

# Numerical simulations of a novel offshore floating solar system

A study on the simulation possibilities for an interconnected, multi-body floating system using a combined frequency-time domain approach  
W.J. Botman





# Numerical simulations of a novel offshore floating solar system

A study on the simulation possibilities for an interconnected, multi-body floating system using a combined frequency-time domain approach

by

W.J. Botman

to obtain the degree of Master of Science  
at the Delft University of Technology,  
to be defended publicly on October 29 2019.

Student number:	4279336
Project duration:	January 7, 2019 – October 29, 2019
Thesis committee:	Dr. Ir. P.R. Wellens TU Delft, Chairman
	Dr. -Ing. S. Schreier TU Delft, daily supervisor
	Dr. Ir. H. Polinder TU Delft
	Ir. R.J. van der Wiel Oceans of Energy, daily supervisor
	Ir. W.J. Otto MARIN, external member

*This thesis is confidential and cannot be made public until December 31, 2021.*

An electronic version of this thesis is available at <http://repository.tudelft.nl/>.

# Preface

For the past 10 months I have worked, sometimes with the unavoidable healthy doses of stress but mostly with great pleasure, on my graduation thesis that is presented in this report. The subject is one that is close to my heart, due to the challenge it presented in hydrodynamics but also due to the relevance of the application of offshore floating solar for the development of renewable energy.

First and foremost, I would like to thank my entire thesis committee, Dr. Ir. Peter Wellens, Dr. -Ing. Sebastian Schreier, Dr. Ir. Henk Polinder, Ir. Robert van der Wiel and Ir. William Otto for thoroughly reading and discussing the work in this report, to guarantee it's quality. I would specifically like to thank my supervisors, Sebastian, Robert and William.

Sebastian, you have thought me a great deal, not only regarding this specific subject, but also about doing academic research in a more general sense. Additionally, you were always available for my questions and I have enjoyed and appreciated our discussions very much.

Robert, you have been my sparring partner throughout this entire process and have supported me with valuable tips and feedback. I really appreciate all the time you took to patiently help me, and I have enjoyed working together!

William, your experience in aNySIM and insights in the simulations has taught me a lot and gave me inspiration for next steps during this process.

I am also very grateful to Huibert-Jan, Anne, Fabian and Maarten for proofreading parts of this thesis and the useful feedback.

I have spent the past 10 months at the company Oceans of Energy and I would like to thank everyone there for really including me in the company during this interesting journey. Seeing all the daily challenges and important milestones has taught me so much that was outside the scope of this project, from which I will benefit in the rest of my career. Furthermore, working at the start up has undoubtedly made my graduation time much more fun :) I am positive that OOE awaits a successful future and I am proud to have worked with you!

Finally, I would like to thank my parents and sisters, who have supported me with their constant interest and their good advise, not only during these past 10 months but throughout my entire time as a student in Delft. And last but not least, I would like to thank Luuk, for all your valuable insights in this research, but also for being my distraction when I needed something else on my mind. You are my rock, thank you!

Willemijn Botman  
Delft, October 2019

# Abstract

The development of renewable energy applications has become increasingly important in the past couple of years due to a growing global energy demand and increasing consciousness of global warming. A recent development in renewable energy is the application of offshore floating solar systems. A prototype design for this application, as developed by the company 'Oceans of Energy', consists of multiple, interconnected floating platforms (floaters), moored to the sea bed. The floaters are characterised by their small dimensions compared to the wave length.

One of the challenges for offshore floating solar systems is the continuous wave induced force acting on the floater that can become significant in severe weather conditions. Numerical simulations are often used to analyse and predict these forces. Combined frequency-time domain solvers are the most promising tool for this design to obtain reliable results within reasonable computational time. Studies done previously on this tool for multi-body systems emphasize the challenges in coupled hydrodynamics, viscous damping implementation and gap resonance effects. However, these studies focus on systems with fewer bodies and larger dimensions. Therefore, the capability of the simulation tool is unknown for this specific design. Hence, the main question of this study is: *To what extent is the frequency-time domain solver able to simulate the behaviour of an interconnected, multi-body, offshore floating solar system?*

A numerical model was developed in the simulation tool 'aNySIM'. Experiments conducted in the offshore basin at MARIN were used for the model structure development and validation. Additionally, viscous damping effects were implemented from empirical data based on the experiments. Decay tests were used for damping determination. This resulted in inaccurately determined forces and motion amplitudes for regular and irregular wave tests, indicating the presence of parameter uncertainty. A new damping determination method was introduced, using regular wave results as input. The accuracy of the model improved with 4% using this method. Nonetheless, inaccuracies in mooring line forces, oscillating behaviour and motion amplitudes are present.

These inaccuracies have been addressed with an uncertainty analysis and sensitivity studies. Trends within the accuracy of the simulation model were linked to physical phenomena that occurred during the experiments. Analysis showed that several effects, related to the novel design characteristics, influence the model accuracy. Multi-body (e.g. shielding of floaters), small dimensions (e.g. coupled viscous effects) and mooring system (e.g. hydrodynamic loads on the mooring lines) effects have been identified; all influencing the viscous damping of the system. Additionally, nonlinear effects due to breaking waves and overflowing water have been identified.

For regular wave tests and lower irregular wave tests, the simulation model gives reliable results with errors in the mooring line forces below 10%. These errors are mainly ascribed to viscous damping effects. For irregular wave tests with a significant wave height larger than 4.75 metre and a peak period longer than 10.4 seconds, the simulation behaviour shows discrepancies and errors in the mooring line forces increase. In these tests, nonlinear effects due to breaking waves and overflowing water become more relevant.

For future work, different uncertainty causes must be further isolated in the simulation model. This can be done by obtaining more experimental data. To quantify several effects, studies in other numerical tools can be performed (e.g. CFD calculations) and more extended sensitivity studies must be executed in aNySIM.

# Contents

<b>List of Abbreviations</b>	<b>v</b>
<b>List of Figures</b>	<b>vi</b>
<b>List of Tables</b>	<b>vii</b>
<b>1 Introduction</b>	<b>2</b>
<b>2 Physical model and conditions</b>	<b>6</b>
2.1 Offshore basin model . . . . .	6
2.1.1 Model particulars . . . . .	6
2.1.2 Scaling. . . . .	6
2.2 Experiments . . . . .	8
2.2.1 Performed tests . . . . .	8
2.2.2 Physical conditions . . . . .	9
2.3 Informational uncertainty . . . . .	14
2.4 Conclusion . . . . .	15
<b>3 Simulation model development</b>	<b>16</b>
3.1 aNySIM . . . . .	16
3.2 Model assumptions . . . . .	16
3.2.1 Assumptions of the frequency-time domain approach. . . . .	16
3.2.2 Assumptions specific for this model implementation . . . . .	17
3.3 Mathematical model . . . . .	18
3.3.1 System geometry and notation. . . . .	18
3.3.2 System description single body system . . . . .	18
3.3.3 System description multi-body system. . . . .	22
3.4 Numerical model . . . . .	23
3.4.1 General overview aNySIM and DIFFRAC. . . . .	23
3.4.2 DIFFRAC - Hyd file. . . . .	24
3.4.3 aNySIM - XMF file . . . . .	25
3.5 Preliminary sensitivity study . . . . .	29
3.6 Conclusion . . . . .	31
<b>4 Damping implementation and model accuracy</b>	<b>33</b>
4.1 Static equilibrium. . . . .	33
4.1.1 Method . . . . .	33
4.1.2 Results . . . . .	33
4.1.3 Concluding remarks . . . . .	35
4.2 Damping determination "decay-fit" . . . . .	35
4.2.1 Method . . . . .	36
4.2.2 Results "decay-fit" damping determination . . . . .	38
4.2.3 Concluding remarks . . . . .	42
4.3 Damping determination 'regular wave-fit' . . . . .	43
4.3.1 Method . . . . .	43
4.3.2 Results . . . . .	44
4.3.3 Concluding remarks . . . . .	47
4.4 Model accuracy . . . . .	47
4.4.1 Data outliers . . . . .	49
4.5 Conclusion . . . . .	50

<b>5</b>	<b>Uncertainty analysis</b>	<b>51</b>
5.1	Method . . . . .	51
5.2	Regular wave test results . . . . .	52
5.2.1	Surge and sway motion in head and beam waves . . . . .	52
5.2.2	Surge and sway motion in oblique waves . . . . .	52
5.2.3	Heave motion . . . . .	53
5.2.4	Roll and pitch motion . . . . .	54
5.2.5	Yaw motion . . . . .	54
5.3	Irregular wave test results . . . . .	54
5.3.1	Motion amplitude accuracy SLS . . . . .	55
5.3.2	Motion amplitude accuracy bridging tests . . . . .	57
5.3.3	Oscillating behaviour . . . . .	57
5.4	Conclusion . . . . .	59
<b>6</b>	<b>Sensitivity studies</b>	<b>61</b>
6.1	Method . . . . .	61
6.1.1	Hydrodynamic mooring line implementation . . . . .	61
6.1.2	Shielding effect . . . . .	62
6.1.3	Coupled pitch-surge damping . . . . .	63
6.2	Results . . . . .	65
6.2.1	Parameter 1 - Hydrodynamic mooring line implementation . . . . .	66
6.2.2	Parameter 2 - Shielding effect implementation. . . . .	66
6.2.3	Parameter 3 - Coupled pitch-surge damping implementation . . . . .	66
6.2.4	Mooring line forces in irregular waves . . . . .	68
6.2.5	Decay test results . . . . .	69
6.3	Conclusion . . . . .	69
<b>7</b>	<b>Discussion</b>	<b>71</b>
7.1	Limitations of this study . . . . .	71
7.2	Interconnected, multi-body offshore floating solar systems. . . . .	72
7.3	aNySIM . . . . .	73
<b>8</b>	<b>Conclusion and recommendations</b>	<b>74</b>
8.1	Conclusion . . . . .	74
8.2	Recommendations . . . . .	75
	<b>Bibliography</b>	<b>76</b>
<b>A</b>	<b>Basin model details</b>	<b>79</b>
A.1	Test details . . . . .	79
A.2	Video footage findings . . . . .	80
<b>B</b>	<b>DIFFRAC method and verification</b>	<b>81</b>
B.1	First order excitation force . . . . .	81
B.2	Second order excitation force. . . . .	82
B.3	Hydrodynamic coefficients . . . . .	83
<b>C</b>	<b>aNySIM implementation</b>	<b>85</b>
C.1	Main XMF file . . . . .	85
C.2	Sub XMF file - Floater . . . . .	86
C.3	Sub XMF file - Mooring system catenary line . . . . .	87
C.4	Sub XMF file - Joints . . . . .	87
C.5	Sub XMF file - Mooring system Lumped mass line . . . . .	88
<b>D</b>	<b>aNySIM simulations</b>	<b>89</b>
D.1	Zero procedure . . . . .	89
D.2	Static offset test . . . . .	89
D.3	Decay tests . . . . .	90
D.4	User defined wave elevation time trace . . . . .	90
D.5	aNySIM defined wave elevation. . . . .	91

<b>E</b>	<b>Studies in aNySIM</b>	<b>92</b>
E.1	Numerical integration . . . . .	92
E.2	Mechanical joint damping . . . . .	93
E.3	Drag coefficient . . . . .	93
E.4	Lumped mass line time step and number of elements . . . . .	94
<b>F</b>	<b>aNySIM results</b>	<b>95</b>
E1	Mooring line errors all irregular wave tests . . . . .	95
<b>G</b>	<b>Supporting figures and tables</b>	<b>97</b>
G.1	Comparison hydrodynamic/viscous damping . . . . .	97
G.2	Hydrodynamic coupling between degrees of freedom . . . . .	98
G.3	Force contributions . . . . .	98
G.4	Maximum mooring line forces Basin test results . . . . .	99
G.5	Shielding implementation . . . . .	99

# List of Abbreviations

BT	Basin test
CFD	Computational Fluid Dynamics
COG	Centre of Gravity
DOF	Degree Of Freedom
EQOM	Equation of motion
FS	Full scale
GCS	Global Coordinate System
LCS	Local Coordinate System
MARIN	Maritime Research Institute Netherlands
MS	Model scale
ODE	Ordinary Differential Equation
OOE	Oceans Of Energy
PS	Portside
PSA	Portside Aft
PSF	Portside Front
QTF	Quality Transfer Function
RAO	Response Amplitude Operator
SB	Starboard
SBA	Starboard Aft
SBF	Starboard Front
SLS	Serviceability Limit State
ULS	Ultimate Limit State
XMF	eXtensible Modelling Framework

# List of Figures

1.1	Artist impression of the system design of OOE. The design consists of 12 floaters connected to each other and the sea bed. The floaters are shown as one body here. The mooring lines are not a representation of reality. . . . .	2
1.2	Schematic overview of the model setup for the basin model and the simulation model. The arrows indicate where information is transferred from the basin model to the simulation model and how information flows within the two different models. The colour indicates the source of uncertainty that could be present. This uncertainty could influence the final accuracy of the simulation model and thus the reliability. . . . .	5
2.1	Schematic overview of the mooring setup on model scale, where the stiffness is implemented with 2 springs, spring A and B . . . . .	7
2.2	Numbering and orientation of the 12 floaters as used in the basin model . . . . .	7
2.3	Decay time traces of basin tests in surge, sway and yaw direction, shown for floater 7. The signals damp out quickly. . . . .	9
2.4	The surge motions of floater 3 and 7 around their equilibrium, to observe the differences in behaviour. From these figures it can be observed that the system of 12 floaters is generally behaving as 1 system. . . . .	10
2.5	Schematic overview of wave follower behaviour. The three floaters are shown at a different moment in time, and the heave and pitch (or roll) motion are mainly determined by the free surface of the wave. . . . .	10
2.6	Video stills of the regular wave tests R-56 and R-58 to show the differences in wave generation at the aft of the floaters (highlighted by the red arrow). Note that the video images have been blurred for confidentiality reasons. Both stills were taken at the same point in the oscillation of the system. . . . .	11
2.7	Schematic visualisation of the flow behaviour within the gaps between two floaters. Water flows through and onto the floaters, causing a turbulent flow. Some of the water flows back trough the gaps, further disturbing the flow. At the outer edges of the system, turbulent flow effects can be observed as well. . . . .	12
2.8	Mooring line force in mooring line SBF (starboard front) for a certain moment in time at which slamming occurred. . . . .	12
2.9	Measured overflowing water for irregular wave test I-12 ( $T_p = 11.40s, H_s = 4.47, \mu = 90^\circ$ ), compared to the wave elevation. No clear relation can be observed, indicating that other effects influence the overflowing water. . . . .	12
2.10	The mean level of overflowing water for floater 5, 9, 10 and 11, given for all regular and irregular wave tests. . . . .	13
2.11	Two examples of the effect of breaking wave incidents on the mooring line forces. . . . .	14
2.12	This figure shows an invalid signal for the x location of two floaters due to the effect of water drops on the measuring system at the black arrows This invalid signal is solved by MARIN by fitting a spline interpolation [31] . . . . .	15
3.1	Schematic overview of an effect of wave follower behaviour, explained with the pitch added mass. Due to long waves compared to the floater dimensions, the actual pitch motion (relative to the wave angle) is lower than the absolute pitch motion as used in DIFFRAC. This results in a lower added mass and damping in the basin model. . . . .	17
3.2	Global and local coordinate systems used for the floaters in the mathematical model . . . . .	19
3.3	Overview of the set up of aNySIM in combination with DIFFRAC. The aNySIM model uses the hyd file obtained in DIFFRAC as input for the hydrodynamic coefficients. . . . .	24
3.4	Overview of the main XMF file used for the aNySIM model . . . . .	25

3.5	Restoring force in heave and moment in pitch comparison of aNySIM results with analytically calculated value for 1 floater . . . . .	26
3.6	Forces in all four mooring lines for a static offset test obtained from the aNySIM simulation. The lines show symmetric behaviour, and a linear relation with a direction coefficient that is equal to the spring stiffness. This verifies the mooring stiffness implementation. . . . .	29
3.7	Motion RAO for different frequencies and different damping values, obtained with a aNySIM defined regular wave train. The grey bars indicate the transition between the three ranges of governing forces (spring, damping or mass dominated). . . . .	30
3.8	The regular and irregular wave tests that have been executed in the offshore basin are classified according to their (peak) period in the area of stiffness, damping or mass dominated motions. . . . .	30
3.9	The coupled hydrodynamic damping in surge and sway direction due to motions in all DOF, obtained from the hyd file. . . . .	31
3.10	Motion RAO in surge and sway for a range of incoming wave angles to visualise the effect of a different incoming wave. . . . .	31
4.1	Results of the pretension in all 4 mooring lines measured with a zero procedure. The pretension is equal to the pretension measured in the offshore basin tests. The static equilibrium is reached after 120 seconds. . . . .	34
4.2	Mean pretension in the joints between the floaters for the basin tests and aNySIM simulation. Pretension is given in the global coordinate system. . . . .	35
4.3	The mooring line forces of the aNySIM simulations for static offsets in global x and y direction. The static offset in x direction is compared with the basin test results. . . . .	36
4.4	Selected decay time traces of basin tests in surge, sway and yaw direction. . . . .	37
4.5	Results for the surge decay test using the 'decay-fit' damping implementation . . . . .	39
4.6	Results for the surge decay test using the 'decay-fit' damping implementation and a low damped implementation . . . . .	39
4.7	Results of the decay motion in yaw direction with the decay fit. The simulation model results show different behaviour for the first oscillation. . . . .	40
4.8	Comparison of different offset locations in x and y for floater 1 . . . . .	40
4.9	Comparison of the decaying motion in the yaw decay test for different floaters. . . . .	41
4.10	Time trace of the surge motion of floater 7 in regular wave R-50 for the basin test and the aNySIM simulation. The aNySIM simulation underestimates the motion amplitude. A small difference in initial location can be observed . . . . .	41
4.11	Normalised RAO's for all regular wave tests in surge and sway direction, where the RAO of the basin test is set to 1. The RAO's are shown for floater 1 . . . . .	42
4.12	Motion RAO for eight floaters with 'Regular wave-fit' damping. The RAO's of the simulation model are equal to the RAO's of the basin test. . . . .	44
4.13	Motion RAO in surge and sway for all regular wave tests. The 'decay-fit', 'regular wave-fit' and the basin test results are shown. . . . .	45
4.14	Comparison of decay simulations for the 'Regular wave-fit' damping, the 'decay-fit' damping and the basin tests results . . . . .	46
4.15	Comparison of irregular wave simulations for the 'Regular wave-fit' damping, the 'decay-fit' damping and the basin tests results . . . . .	46
4.16	Comparison of irregular wave simulations using a spectral density for the 'Regular wave-fit' damping, the 'decay-fit' damping and the basin tests results . . . . .	47
4.17	Error in mooring line forces for the 10 highest forces obtained from the basin tests. Errors are shown for the 'decay-fit' method and the 'regular wave-fit' method for all 4 mooring lines. . . . .	49
4.18	Error in mooring line forces for the 10 highest forces obtained from the basin tests. Errors are shown for the 'decay-fit' method and the 'regular wave-fit' method for all 4 mooring lines. . . . .	49
5.1	Surge motion of floater 3 and 7 around their equilibrium position. For both the simulation model as the basin test results, the relative motion between the two floaters is negligible. . . . .	53
5.2	Basin test results for the heave motion and the wave elevation. A difference in amplitude of the heave motion compared to the wave elevation can be observed for test R-51 and R-58. . . . .	54
5.3	Spectral density of the surge motion for irregular wave test I-3, showing an overestimation of the simulation model. . . . .	56

5.4	Excitation force RAO obtained from DIFFRAC for four floaters in sway motion. . . . .	56
5.5	Spectral densities of irregular wave test I-11 and I-13, showing the difference in simulation accuracy at the wave exciting ( $\omega_p$ ) and natural $\omega_n$ frequency, both indicated with a dashed black line. . . . .	58
5.6	Examples of oscillation accuracy for different irregular wave tests. The green circles highlight differences in oscillation behaviour for irregular wave test I-14. . . . .	58
5.7	Roll motion of floater 7 in irregular wave I-11. Different behaviour can be observed for the simulation model compared to the basin test results. The green circle highlights the behaviour the moment at which an increase in overflowing water was observed as shown in figure 5.8. . . . .	59
5.8	The time traces of the measured water height on floater 11 for irregular wave I-11. The green circle highlights an increase in overflowing water. The green arrow highlights a lower level of overflowing water . . . . .	59
5.9	Roll and heave results for irregular wave test I-13. The green circle indicates a breaking wave incident. . . . .	60
6.1	Visualisation of the shielding effect per floater, which is dependent on the row and column. . .	63
6.2	Motion RAO for surge and sway of floater 1. All regular wave test results are shown for parameter 1, 2 and 3, together with the results the 'regular wave-fit' model and the basin tests. . . . .	64
6.3	The linear damping force in surge, built up by the surge-surge and pitch-surge damping. Analytic and aNySIM results are equal. . . . .	65
6.4	Motion RAO for surge and sway of floater 1. All regular wave test results are shown for parameter 1, 2 and 3, together with the results the 'regular wave-fit' model and the basin tests. . . . .	67
6.5	Spectral densities of the surge and sway motions of floater 7 for all three parameters, the 'regular wave-fit' model and the basin test results. Different irregular wave tests are shown to perform the sensitivity analysis . . . . .	67
6.6	Spectral densities of all four mooring lines for all three parameters, the 'regular wave-fit' model and the basin test results. . . . .	68
6.7	Decay tests in surge and sway for all three parameters, the 'regular wave-fit' model and the basin test results. . . . .	69
A.1	Details of all tests executed in offshore basin . . . . .	79
A.2	angle=90 . . . . .	80
B.1	First order wave excitation force RAO in z direction for floater 1 to 4 in 2 different wave directions. These values are directly obtained from the hyd file as calculated in DIFFRAC. . . . .	81
B.2	analytic Froude Krylov force calculations compared to the first order excitation force RAO obtained from DIFFRAC . . . . .	82
B.3	Second order wave excitation force QTF values for 2 different combinations of wave frequencies. These values are directly obtained from the hyd file as calculated in DIFFRAC. . . . .	83
B.4	Comparing the DIFFRAC software with calculations in NEMOH. Results are equal for the range of wave exciting frequencies (0.6-1.2 rad/s). The irregularities in higher frequencies, caused by gap resonance effects, can therefore be neglected in this research. . . . .	84
D.1	txt file used for static offset in surge direction . . . . .	89
D.2	External force files used for the decay simulations . . . . .	90
D.3	Wave elevation timetraces at origin of GCS for the basin tests and the aNySIM model . . . . .	91
E.1	Motion of floater1 for 4 different time steps, no differences in results can be observed. . . . .	93
E.2	Results for irregular wave tests . . . . .	94
E.3	Grouping of floaters in rows to combine the forces per row . . . . .	94
E.4	Convergence study on the elements and step size for the Lumped mass mooring line . . . . .	94
F.1	Error in mooring line forces for the 10 highest forces obtained from the basin tests. Errors are shown for the 'decay-fit' method and the 'regular wave-fit' method for all 4 mooring lines. . . .	95
F.2	Error in mooring line forces for the 10 highest forces obtained from the basin tests. Errors are shown for the 'decay-fit' method and the 'regular wave-fit' method for all 4 mooring lines. . . .	95

---

E.3	Error in mooring line forces for the 10 highest forces obtained from the basin tests. Errors are shown for the 'decay-fit' method and the 'regular wave-fit' method for all 4 mooring lines. . . .	96
E.4	Error in mooring line forces for the 10 highest forces obtained from the basin tests. Errors are shown for the 'decay-fit' method and the 'regular wave-fit' method for all 4 mooring lines. . . .	96
G.1	Comparison of contribution hydrodynamic and viscous damping . . . . .	97
G.2	Comparison of contribution hydrodynamic and viscous damping . . . . .	97
G.3	Comparison of contribution hydrodynamic and viscous damping . . . . .	98
G.4	The coupled hydrodynamic damping in heave, roll, pitch and yaw direction obtained from the hyd file. . . . .	98
G.5	Force split for surge and heave in regular wave test R-58 . . . . .	99
G.6	The maximum measured force in the mooring lines for all irregular wave tests, obtained from the MARIN report [31] . . . . .	101

# List of Tables

1.1	A selection of studies performed in time domain using similar approaches as the present research. The design presented in this stu is highlighted in blue. . . . .	3
2.1	Scaling factors with $\rho = 1025 kg/m^3$ . . . . .	7
3.1	SI Units . . . . .	24
3.2	Verification of the damping implementation in aNySIM. The linear damping force and drag are compared to analytically calculated values. . . . .	27
3.3	Particulars of irregular wave tests that exceed maximum force . . . . .	28
4.1	The difference between the basin tests and simulation static equilibrium in full scale, Locations in x and y direction and yaw rotation are given for all 8 floaters equipped with motion sensors. .	35
4.2	Threshold value for decaying motion in model scale (MS) and full scale (FS) and the number of oscillation that will be taken into account. . . . .	37
4.3	Damping coefficient values for 1 floater in comparison to the total hydrodynamic damping . . .	38
4.4	(Damped) natural period for the decay tests in surge, sway and yaw direction. . . . .	38
4.5	Overview of Damping coefficients for 'Decay-fit' and 'Regular wave-fit' . . . . .	44
4.6	Error in mooring lines of the simulation model for maximum force that occurs in the basin test	48
4.7	Overview of the mean error in the mooring lines for the 10 highest forces. The mean error is calculated for the SLS, bridging in oblique waves and bridging in beam waves. . . . .	50
4.8	Accuracy results of regular wave tests using the scale as defined in table 5.1 . . . . .	50
5.1	The used scale for amplitude accuracy of simulation model . . . . .	51
5.2	The used scale for oscillation accuracy of the irregular wave tests . . . . .	51
5.3	Accuracy results of regular wave tests using the scale as defined in table 5.1 . . . . .	52
5.4	Summarised overview of the results of irregular wave tests using the scale as defined in table 5.1	55
5.5	Summarised overview of the oscillation accuracy of irregular wave tests using the scale as defined in table 5.2 . . . . .	55
5.6	The pitch motion and velocity amplitudes for regular waves and the irregular wave I-3 with different wave periods and steepness factors. Note that for the irregular wave test, the significant wave height, peak period and significant pitch amplitude are given. . . . .	56
5.7	Wave characteristics of the tests in which the simulations underestimate the system behaviour .	57
5.8	Overview of the character of the uncertainties that have been identified by analysing the accuracy of the simulation model and the physical conditions during the test. The design aspect related to the uncertainty is mentioned. . . . .	60
6.1	Overview of the shielding coefficients for floater 1 and floater 10 and 11. The latter two have the same shielding coefficient for all wave angles. . . . .	64
6.2	Overview of values used for the calculation of the damping coefficient for the coupled pitch-surge damping. The assumption is made that the force exerted by this damping is around 25% of the first order wave force exerted on the floater in surge direction. . . . .	64
D.1	Desired and actual wave angle that is obtained in the basin tests for regular head and beam waves	91
E.1	Implemented values for joint damping . . . . .	93
G.1	The shielding percentages for all different floaters depending on the incoming wave angle. . . .	100



# Introduction

The development of renewable energy applications has become increasingly important in the past couple of years due to a growing global energy demand and increasing consciousness of global warming. A recent development in renewable energy is the application of offshore floating solar systems. This is not only addressing the problems of global warming, but is also responding to the problem of land scarcity, by using space at sea instead of land.

A pioneer in the field of offshore floating solar is the Dutch company Oceans of Energy [29] (from now on referred to as OOE), currently finalising the world's first prototype of a floating solar system to be deployed offshore [1, 30]. The system consists of 12 interconnected floating platforms (floaters), moored to the sea bed (figure 1.1). An important step for the OOE system is deployment in the North Sea, where the design is exposed to a demanding environment. In order to withstand the significant forces (induced by high waves) that are likely to be present in this environment, prior knowledge on the hydrodynamic behaviour of the system is crucial in the design process.

Conventional methods to obtain insight into this hydrodynamic behaviour use data analysis from experimental (model scale) tests, results from simulation software, and often a combination of the two[5, 8]. Experimental data retrieved from model tests executed at MARIN (Maritime Research Institute Netherlands [21]) has been used to analyse the expected hydrodynamic behaviour of the first prototype design. However, in terms of flexibility, time, and costs, reliable simulation software is more beneficial as a design tool for future developments as minor changes in the design can be implemented in the simulation software quickly.

Simulation solvers can be classified according to the underlying mathematical model, and the assumptions and simplifications made within these models[32]. Generally speaking, a more extensive model is able to obtain higher reliability but computational time also increases. Two types of solvers can be distinguished: frequency domain and time domain [13]. Nonlinear effects can only be incorporated in time domain models. Due to the setup of the system as presented in this study, nonlinear effects such as the interaction between the floaters are crucial in the behaviour [3]. Therefore, frequency domain simulations are not suitable. However, due to high computational times (order of magnitude of multiple days for 1000s real time simulation[12]), Computational Fluid Dynamics (CFD), an extensive time domain solver in which all nonlinear effects are incorporated, is not suitable either. The combination of a frequency domain solver and a time domain solver

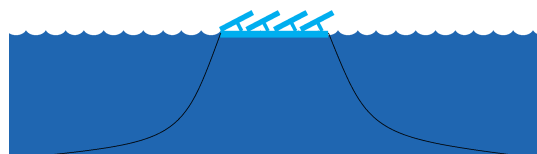


Figure 1.1: Artist impression of the system design of OOE. The design consists of 12 floaters connected to each other and the sea bed. The floaters are shown as one body here. The mooring lines are not a representation of reality.

Table 1.1: A selection of studies performed in time domain using similar approaches as the present research. The design presented in this study is highlighted in blue.

Relevant studies	Number of bodies	$\lambda/L$	$H_s/D$	Significant wave height	Viscous damping implementation
<b>Novel offshore floating solar system</b>	12	5-15	5-15	6m	Decay tests
Flexible joint multi-body floating system [4]	6	1	0.8	2m	No viscous damping
Side by side moored vessels [3, 27, 39]	2	<2	<1	4m	Decay tests
Float over system [2]	1	1	<1	No details	Decay tests

is a method that is used often for offshore systems (e.g. side by side operations [3, 27, 39]) and offers a better solution for this specific design: Computational time remains within reasonable limits (order of magnitude of a couple of hours for 1000s real time simulation[34]) and nonlinear effects regarding mooring line dynamics and coupling between the bodies can be included. Therefore, this approach has been chosen as simulation tool for the offshore floating solar system.

First results regarding the simulation of this offshore floating solar system were obtained by Van Poppelen [34]. This study has shown that the applied simulation method resulted in inaccurately determined mooring line forces and system behaviour. As a result, Van Poppelen [34] concluded that more research is required on the viscous damping implementation to obtain higher reliability.

Previous studies related to the numerical simulation of multi-body systems have been done for numerous different designs, using different numerical models. A multi-body application of floating piers has been studied by Tajali et al. [40] in frequency domain, in which was observed that the motions were strongly influenced by the draft and that the motion response in waves increases for an increasing number of bodies. However, no validation was provided.

The applicability of a frequency-time domain simulation tool on a flexible joint, multi body floating system was studied by, amongst others, Chen et al. [4]. Results showed relatively good agreement with validation data, but no details were provided on the observed sea states. Both studies have neglected the effect of viscous damping.

Buchner et al. [3] and Naciri et al. [27] have addressed the importance of correct implementation of hydrodynamic and mechanic coupling between individual bodies. Moreover, Buchner et al. [3] emphasizes the viscous damping implementation by using relative damping coefficients, determined with decay tests. Recommendations are made regarding wave resonance effects in the gap between the bodies and a more extended viscous damping.

A study done by Bokhorst et al. [2] on float over operations has implemented damping using decay tests for surge and sway and sea states with various wave heights for roll damping. The importance of a correct damping implementation on the simulation accuracy, specifically for the roll motion, is emphasised.

These studies substantiate the conclusion drawn by Van Poppelen and indicate several aspects (viscous damping effects, gap resonance effects and the (hydro)dynamic coupling between bodies) that introduce uncertainties in the simulation model.

Although substantial research has already been conducted, the present design shows significant structural differences that need to be taken into account. An overview of characteristics is given in table 1.1.

Firstly, the present design consists of 12 bodies, compared to 1, 2 or 6 bodies in previous research. It is expected that the hydrodynamic and viscous damping coupling (as discussed by Buchner et al.[3]) becomes even more important for this design. Secondly, the previous research focusses on vessels with a length in the same order of magnitude as the wave lengths ( $\lambda$ ). The present design will be exposed to sea states with wavelengths that are 10 to 15 times the body length. This difference in dimensions causes different system behaviour. Similarly, the wave height divided by the structure height ( $D$ ) is approximately  $H_s/D = 10$  for this design. This ratio is strongly related to water flowing over the structures on a regular basis, something that is not studied in the studies above (where  $H_s/D < 1$ ). Studies on the implementation of overflowing water mainly consider dam break models [47] or overwash on ice structures[35], and demonstrate that this

overflowing water is accompanied by strong nonlinear effects and that correct simulations require extensive numerical models.

The different number of floaters and dimensions lead to an increase in uncertainty regarding the aspects identified in previous research. Moreover, new effects (e.g. due to overflowing water) are likely to be introduced. Therefore, more research is required on the simulation capabilities of interconnected, multi-body systems with small dimensions compared to the wave length. With the focus on the rapid evaluation of design options, combined frequency-time domain simulations are the most promising approach for reasonably fast and sufficiently reliable computations. Hence, the following main research question has been formulated:

**To what extent is the frequency-time domain solver able to simulate the behaviour of an interconnected, multi-body, offshore floating solar system?**

Several sub questions have been formulated to support this main question:

1. Which physical phenomena influence the behaviour of the system?
2. What is a good simulation model implementation of the used physical (scale) model?
3. What is the reliability of the simulation model compared to the validation data?
4. Which uncertainties are causing inaccuracies in the simulation model?
5. Which aspects within the simulation tool require more research or adjustments for further improvement?

To answer the main and sub research questions, several definitions require clarification:

- The *behaviour* of the system is defined as the motions of the floaters in 6 degrees of freedom and the mooring line forces. Distinction is made between the *oscillating behaviour* and the motion and force *amplitudes*.
- The simulation model is considered *reliable* for engineering purposes when the oscillating behaviour of the system shows the same trend as the validation data and the mooring line force amplitudes are determined within an error of 10%. This number is defined in consultation with Oceans of Energy.
- *Uncertainties* that might influence the model accuracy are studied. Figure 1.2 gives a schematic overview of the model set up and the locations where these uncertainties occur. Four uncertainties are defined [19]:
  - *Informational uncertainty*: imprecision in specified boundary and initial conditions or measured output variable values.
  - *Numerical uncertainty*: errors in the model solution algorithm.
  - *Parameter uncertainty*: wrongly determined parameter values.
  - *Model structure uncertainty*: incomplete or incorrect model structure.

This report is set up as follows:

Chapter 2 presents the physical model and physical behaviour that has been used during this research (related to research question 1). Additionally, the informational uncertainty is addressed.

Chapter 3 presents the model structure of the simulation model (related to research question 2). The numerical implementation is verified, addressing the numerical uncertainty .

In chapter 4, two different damping determination methods are presented and analysed, addressing the parameter uncertainty in the model. Furthermore, results are shown regarding the model reliability (related to research question 3).

An uncertainty analysis on the model behaviour is presented in chapter 5, identifying physical parameters that influence the accuracy of the model (related to research question 4 and 5).

A sensitivity study is then applied to three selected parameters to further quantify their effect in chapter 6 (related to research question 4 and 5).

The results and findings are discussed in chapter 7 and final conclusions are presented in chapter 8.

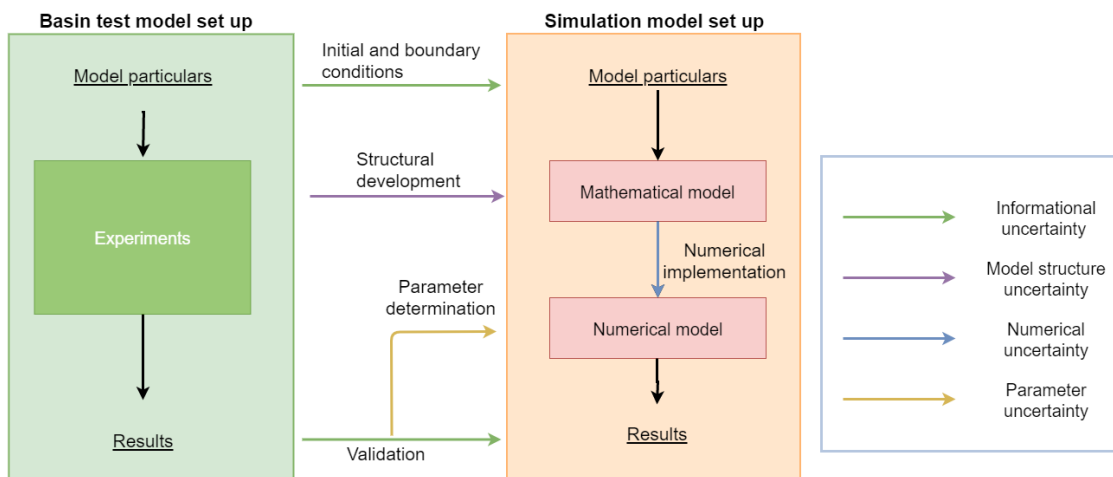


Figure 1.2: Schematic overview of the model setup for the basin model and the simulation model. The arrows indicate where information is transferred from the basin model to the simulation model and how information flows within the two different models. The colour indicates the source of uncertainty that could be present. This uncertainty could influence the final accuracy of the simulation model and thus the reliability.

# 2

## Physical model and conditions

The design used for the present research was adopted from the physical scale model as used in the basin experiments, from which the results were used for behavioural analysis and validation. The goal of this chapter is to provide insight in this physical model and important conditions that need to be taken into account for development of the simulation model. This is related to research question 1 as introduced in chapter 1.

Characteristics of this design are presented in the first section, whereafter details of the experiments are presented and the behaviour of the system in the experiments is analysed. Finally, the informational uncertainty of the model is addressed.

A report produced by MARIN [31] regarding all model specifics and video footage of the executed tests are used as main source for this chapter. However, since this report is not publicly available, relevant details of the offshore basin and tests can be reviewed in appendix A.

### 2.1. Offshore basin model

The design consists of twelve floaters, moored to the seabed with four mooring lines and interconnected with joints. An artists impression of the design can be observed in figure 1.1. In the offshore basin model, the solar panel superstructure is neglected, and only the floaters are studied. The weight of the superstructure has been incorporated in the weight of the floaters. Wave and current measurement probes are set up in the basin, to measure the realised sea states.

#### 2.1.1. Model particulars

##### **Floaters**

Figure 2.2 shows the floater setup for floaters in more detail, with the numbering used in the basin tests. The earth fixed coordinate system is defined as shown in the top left corner of the figure. The origin of this coordinate system is located 1 metre above still water level and in the centre of the twelve floaters. The local coordinate system of a floater has its origin at the vertical centre of gravity (COG) in the horizontal centre. Eight of the twelve floaters are equipped with an optical tracking target and the remaining four floaters have a wave probe, from which the data gives insight in the overtopping waves.

##### **Joints**

The floaters are connected to each other using so called joints, which are implemented as springs.

##### **Mooring**

Four mooring lines are implemented in the model setup. Figure 2.1 shows a schematic overview of the mooring line. A nonlinear stiffness is mimicked with 2 springs with different stiffnesses. Spring A has a higher stiffness than spring B.

#### 2.1.2. Scaling

As is common for ship and offshore structures, the full scale design is scaled to model scale using Froude scaling, since both gravity forces (waves) and inertia forces play an important role. The Froude number is defined as:

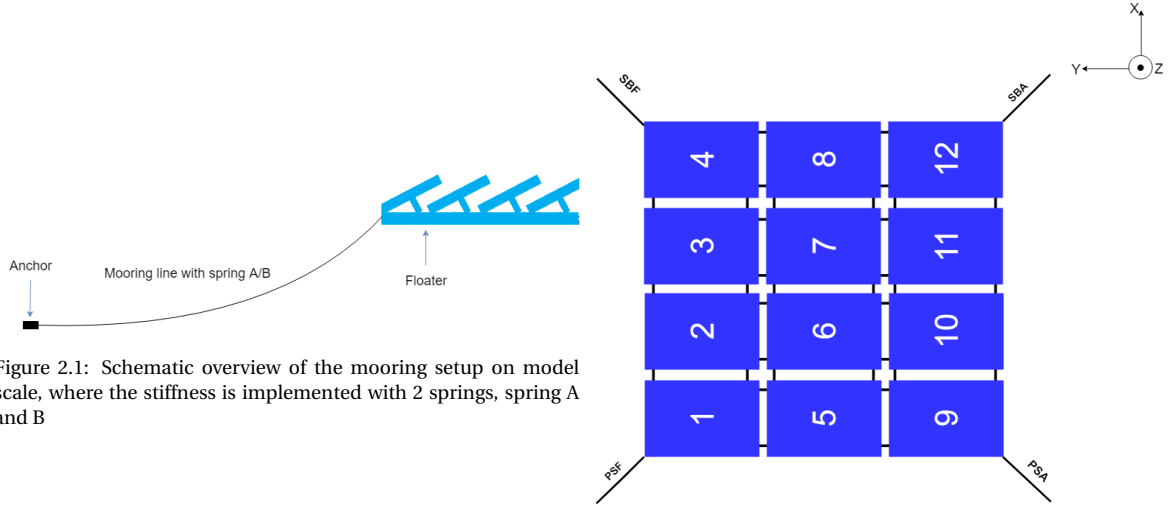


Figure 2.1: Schematic overview of the mooring setup on model scale, where the stiffness is implemented with 2 springs, spring A and B

Figure 2.2: Numbering and orientation of the 12 floaters as used in the basin model

$$F_n = \frac{\text{Inertia forces}}{\text{Gravity forces}} = \frac{u_m}{\sqrt{gL_m}} = \frac{u_f}{\sqrt{gL_f}} \quad (2.1)$$

Where:  $g$  is the gravitational acceleration,  $u$  is the flow velocity and  $L$  is the characteristic length. The subscripts  $m$  and  $f$  indicate model and full scale respectively. Using Froude's law of similitude implies that gravity forces are preponderant over for instance viscous forces, which is a valid assumption for problems including a surface and free surface waves as long as the waves are long enough and surface tension is not important. For this model a geometric scale is used of  $\lambda_s = 1 : 20$ , resulting in the scaling factors as shown in table 2.1. Several scaling factors are also dependent on the density  $\rho$  of the fluid.

Table 2.1: Scaling factors with  $\rho = 1025 \text{ kg/m}^3$

Quantity	Model scale	Prototype scale	Ratio
Linear dimension	1 [m]	20.00 [m]	$\lambda_s$
Area	1 [ $m^2$ ]	400 [ $m^2$ ]	$\lambda_s^2$
Volume	1 [ $m^3$ ]	8000 [ $m^3$ ]	$\lambda_s^3$
Time	1 [s]	4.472 [s]	$\sqrt{\lambda_s}$
Velocity	1 [m/s]	4.472 [m/s]	$\sqrt{\lambda_s}$
Acceleration	1 [ $m/s^2$ ]	1 [ $m/s^2$ ]	1
Angle	1 [deg]	1 [deg]	1
Angular velocity	1 [deg/s]	0.224 [deg/s]	$1/\sqrt{\lambda_s}$
Mass	1 [kg]	$8.2 \cdot 10^3$ [kg]	$\rho \lambda_s^3 / 1000$
Force	1 [N]	8.2 [kN]	$\rho \lambda_s^3 / 1000$
Moment	1 [Nm]	164.0 [kNm]	$\rho \lambda_s^4 / 1000$

Although scaling has been done with inertia and gravity forces, viscous forces are present in the physical problem. Scaling these forces is often done by assuming a constant Reynolds number in model and full scale:

$$Re = \frac{\text{Inertia forces}}{\text{Viscous forces}} = \frac{uL}{\mu} \quad (2.2)$$

Where  $\mu$  is the kinematic viscosity. To obtain an equal ratio between model and full scale, it is required to change the viscous flow of the model scale. As this is not possible for model tests in water, scaling according to Froude's law of similitude means that the Reynolds number is not similar for prototype and model scale and viscous forces are not scaled correctly. Using the Froude number is preferred over the Reynolds number since

gravitational effects are larger than viscous effects on ship motions[13]. By applying Froude's law of similitude, the Reynolds number is scaled with  $m^2/s = \lambda_s^{3/2}$ . This means that for  $\lambda_s = 20$ , the Reynolds number of the full scale is 89.44 times as large as the Reynolds number of the model scale. The transition towards a turbulent flow is around  $Re = 1E4$ . For both the model scale and full scale, Reynolds numbers are between  $Re = 1E6$  and  $Re = 1E9$ , which means that both flows are within the turbulent regime.

For this research, the choice was made to use the full scale results and accept the possible inaccuracy caused by the scaling effect. This is done to allow for a conclusion on the usability of the simulation tool as a design tool, where the accuracy on full scale should be analysed. This report therefore uses the full scale (FS) dimensions as standard dimensions. If model scale (MS) dimensions are relevant, this is explicitly mentioned.

## 2.2. Experiments

The data obtained by MARIN for the different tests consist of signals that are measured with an analogue system or digitally. The analogue data was sampled and stored at a sampling rate of 200Hz. This results in a time interval between two signals of 0.02236 seconds on full scale. Data that was sampled and stored analogue are the forces in the mooring line and the wave elevation signals in the basin and on the floaters. The digitally sampled data had a sampling rate of 100Hz, corresponding to a time interval of 0.04472seconds. The positions of the floaters were sampled and stored digitally.

Data was obtained for 1.5 hours for irregular waves and for 1300 seconds for regular waves. Due to possible transient phenomena, a start-up phase of half an hour is used for the irregular wave tests and of 300 seconds for the regular wave tests. Results within this start up phase are not analysed.

The results obtained have been pre-processed by MARIN before they were delivered to OOE. This pre-processing contains translations from target positions to COG positions of the floaters and calculation of joint forces from the relative distance between floaters. Additionally, the results have been scaled from model scale to full scale.

### 2.2.1. Performed tests

Several different tests were performed in the offshore basin of MARIN, hereafter referred to as basin tests. These basin tests can be split into several groups that were used as input for the numerical model and validation. An overview of all tests is given in appendix A.1, where the number in front of the tests will later be used for reference. These numbers are also noted here.

#### Static tests

*Test Z-15, S-17, S-18*

Zero procedures, in which the basin model is not subjected to external forces and static equilibrium is reached, have been performed to obtain the pretension in the lines and joints.

Static offset tests have been performed to obtain the mooring line forces given a specific offset. No external dynamic forces are implemented, enabling an analysis of the mooring line stiffness.

#### Decay tests

*Test D-12, D-13, D-14*

The decay tests were performed in the three horizontal directions: Surge, sway and yaw. These tests are used to obtain the natural frequency and damping coefficients.

#### Regular waves

*Head waves - Test R-50, R-51, R-52*

These tests served mainly to analyse the behaviour of the system in surge, with wave periods near the natural period of the system in surge direction.

*Beam waves - Test R-53, R-54, R-55*

These tests served mainly to analyse the behaviour of the system in sway direction, with wave periods near the natural period of the system in sway direction.

*Oblique waves - Test R-56, R-57, R-58*

These tests have an incoming wave angle of  $\mu = 170^\circ$  and increasing wave periods. The tests mainly served to analyse the behaviour of the system in longer waves, where the small wave angle causes some effects in both surge and sway and therefore a higher system rotation.

#### Irregular waves

Irregular wave tests have been carried out in serviceability limit state (SLS), sea states in which the structure is fully functional, an ultimate limit state (ULS), containing the maximum sea states the structure should be able to withstand, and bridging states, containing sea states from SLS to ULS. For this research, the focus of

analysis was on the SLS and the bridging states. The ULS was not taken into account due to the increasing non-linear effects, which increase the uncertainty in the model.

*Serviceability limit state (SLS) – Tests I-3, I-4, I-5 and I-6*

These tests have the same significant wave height (2m) and wave peak period (6.8s) with incoming wave angles of  $\mu = 180^\circ, 135^\circ, 105^\circ$  and  $90^\circ$ . The effect of an altering wave angle can be analysed with these tests. Furthermore, due to their close similarity to the regular waves, a comparison in behaviour can be made.

*Bridging state, beam waves – Tests I-8, I-10, I-12, I-14*

The bridging state tests increase in wave height and wavelength and serve to analyse the effect of these increasing sea states. Four increasing sea states are tested for beam waves ( $\mu = 90^\circ$ ). These tests allow for an analysis of the system with a dominating sway motion, where surge motions can be neglected.

*Bridging state, oblique waves – Tests I-7, I-9, I-11, I-13,*

The bridging tests increase in wave height and wavelength and serve to analyse the effect of these increasing sea states. Four sea states tested oblique waves ( $\mu = 135^\circ$ ). These tests allow for analysis of the system where both surge and sway motions are present, and the system experiences more yaw rotation.

## 2.2.2. Physical conditions

Video footage of regular and irregular wave tests has been used to obtain insight in the system behaviour. Decay tests were not recorded. Appendix A.2 gives an overview of the findings from video material for all regular wave tests and irregular tests I-3 to I-14. The following sections elaborate on several phenomena that were observed in the video footage.

### Decay behaviour

Decay tests performed in surge, sway and yaw all showed similar behaviour of a highly damped system, as shown in figure 2.3. The results show very few oscillations, whereafter the signal is damped out, only showing very small amplitudes.

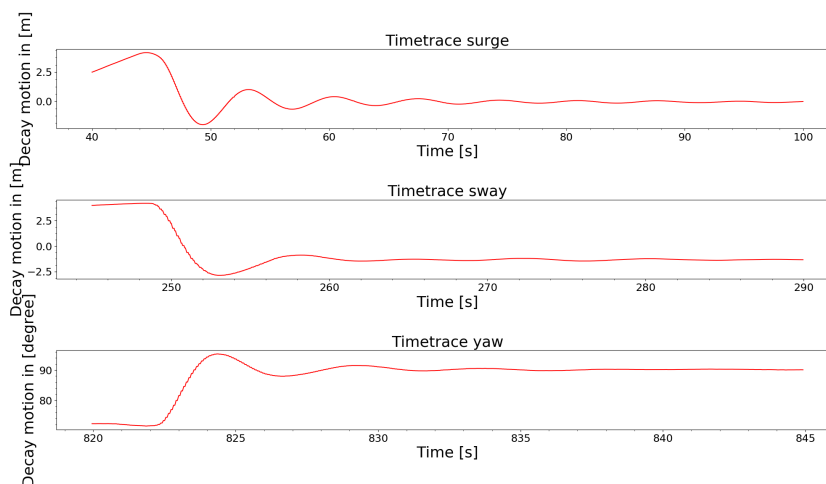
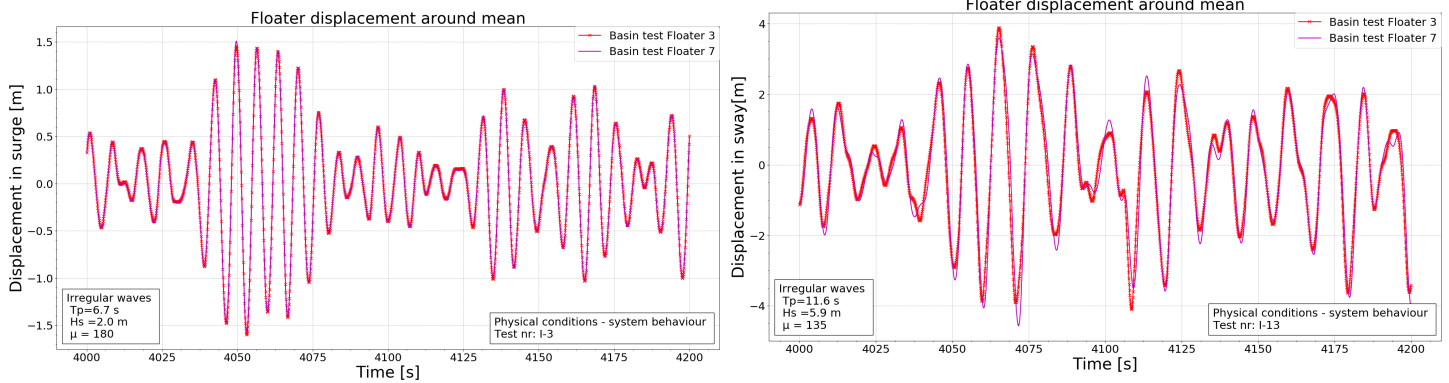


Figure 2.3: Decay time traces of basin tests in surge, sway and yaw direction, shown for floater 7. The signals damp out quickly.

### System behaviour

For both the regular and irregular wave tests, the multiple floaters are behaving as one system, meaning that the floaters show very little relative motion to each other. To substantiate this finding, the floater motions around their equilibrium position are compared for all irregular wave tests. Relative motions were only observed for the sway motion of floater 3 and 7 for oblique incoming waves, independent of the wave height that was tested. Figure 2.4 shows examples of this system behaviour for irregular wave test I-3, with incoming head waves, and irregular wave test I-13, with oblique incoming waves. As can be observed for the head waves (figure 2.4a), the two floaters show the exact same behaviour in surge. This means that the system behaves as one, no relative motions are observed. For irregular wave I-13, figure 2.4b shows some differences in behaviour for floater 3 and 7, caused by the oblique incoming wave angle.



(a) The surge motion of floater 3 and 7 around their mean value for irregular wave test I-3 (head waves). As can be observed, the floaters have the exact same displacement.

(b) The sway motion of floater 3 and 7 around their mean value for irregular wave test I-13 (oblique incoming waves). As can be observed, the floaters show some differences in behaviour, but overall the time traces show a similar trends.

Figure 2.4: The surge motions of floater 3 and 7 around their equilibrium, to observe the differences in behaviour. From these figures it can be observed that the system of 12 floaters is generally behaving as 1 system.

### Mooring system behaviour

Video footage only gives insight in the mooring line part that is visible above the water surface. Waves were observed around the line that are relatively small compared the flow disturbances around the floaters. These waves originate due to the hydrodynamic characteristics of the lines, where effects as drag and added mass play a role. No clear difference in effects is observed between the regular and irregular wave tests. This indicates that the hydrodynamic force acting on the surfaced part of the mooring line does not change significantly for different tests. For the behaviour of the mooring line below the water surface video footage cannot be used.

The influence of mooring line damping is often related to the low frequency motions of the system, which are, for large offshore structures, close to the natural frequency of the system [42]. Further study on the mooring line dynamics done by Yang [46] states that the mooring line induced damping increases relative to other sources of damping that are affecting the motion response of the vessel considerably at these low frequencies. For this study, the natural frequency of the moored system is close to the wave frequencies instead of the low frequencies. Therefore, damping effects on the mooring lines are expected to become more important around the wave exciting frequencies and less important around the low frequencies, but the significance of this damping is unknown.

### Wave following behaviour

The video footage clearly showed wave following behaviour for the regular wave tests in head and beam waves. Wave following behaviour is defined as behaviour in which the system follows the free surface of the wave and comprises the heave, roll and pitch motion of the system, see figure 2.5 for schematic visualisation. The relative motions (compared to the instantaneous free surface) are relatively small. This is a result of the small dimensions of the system in comparison to the wave length. For head waves  $\frac{\lambda}{L} \approx 8$  and for beam waves  $\frac{\lambda}{B} \approx 30$  (where  $\lambda$  is the wavelength,  $L$  and  $B$  are the length and width of a floater respectively). This behaviour is endorsed by theory([13]) stating that for waves much longer than a body, the body starts to behave as a wave follower.

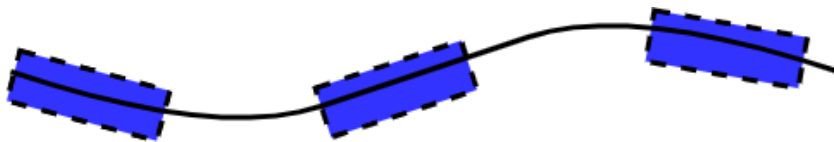


Figure 2.5: Schematic overview of wave follower behaviour. The three floaters are shown at a different moment in time, and the heave and pitch (or roll) motion are mainly determined by the free surface of the wave.

### Flow disturbances around the system

Observing video footage of regular and irregular waves, flow disturbances around the system are visible, which can be described as waves or turbulent effects due to vortex shedding. An schematic visualisation of vortices around the system can be observed in figure 2.7. Due to the sharp edges of the system, the flow is quickly separated and vortices are generated[28]. Quantifying this effect is not possible from the video footage, however a clear trend was observed that for higher waves, more vortices were generated. Thus, this effect becomes more apparent in higher irregular sea states and influences the viscous damping of the system.

Although this effect was not as strongly observed for regular waves (a result of the wave following behaviour in regular waves, causing less flow disturbances), a specific effect of waves generated can be observed in the oblique regular wave tests R-56, R-57 and R-58. The effects for R-56 and R-58 are shown in figure 2.6, where the video stills are taken at a similar moment in the oscillation of the system. Figure 2.6b (R-58, T=10s) clearly shows less generated waves than figure 2.6a (R-56, T=8s) on the aft side of the system (indicated with the red arrow). This difference can be related to the difference in the steepness of the waves, defined as  $\frac{H}{\lambda}$ , where  $H$  is the wave height and  $\lambda$  is the wave length. This steepness is different for all regular wave tests, with decreasing values for regular wave test R-56, R-57 and R-58, giving  $\frac{H}{\lambda} = 0.022, 0.012$  and  $0.010$  respectively. For steeper waves more waves are generated at the end of the floater. These waves can be related to viscous effects (since the wave length of these generated waves was significantly smaller than the incoming wave length, radiated waves are excluded).

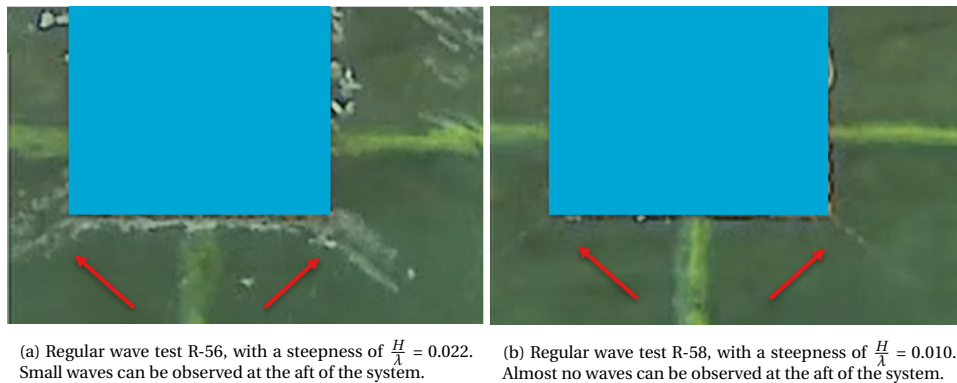


Figure 2.6: Video stills of the regular wave tests R-56 and R-58 to show the differences in wave generation at the aft of the floaters (highlighted by the red arrow). Note that the video images have been blurred for confidentiality reasons. Both stills were taken at the same point in the oscillation of the system.

### Flow disturbances within the system

Video footage showed that water flows through the gaps between the floaters, an effect that becomes more clear in higher irregular sea states. A schematic overview of this effect is presented in figure 2.7. Due to the small dimensions of the floaters, this water is partly flowing over the floaters, and partly flowing back between the gaps (visualised by arrows pointing downwards in figure 2.7). The resulting vortex shedding is an important viscous damping contribution. This effect can be linked to the increasing wave height in higher irregular sea states and the flow direction.

Two effects related to the flow disturbances in the gaps were discussed in literature. Firstly, the viscous effects in the gaps are fortified by the relative motions between the floaters[3], causing high flow velocities within the gaps and resulting vortices. However, from the system behaviour analysis, relative motions between the floaters were identified as very small. Secondly, studies on multi-body offshore structures discuss the effects of both physical as numerical gap resonance[3, 38]. The physical gap resonance effects were not observed in the video footage: as a direct result of the small dimensions, the water is flowing over the floaters instead of being captured in the gaps. Therefore, both aspect are expected to have an insignificant contribution on the system behaviour.

### Overflowing water

Analysing the video's, water is flowing over the floaters regularly, which becomes more apparent for higher waves. The overflowing water can go in multiple directions on the floater, depending on the wave period and direction and effects such as slamming and water flowing through the gaps. A time trace of the measured

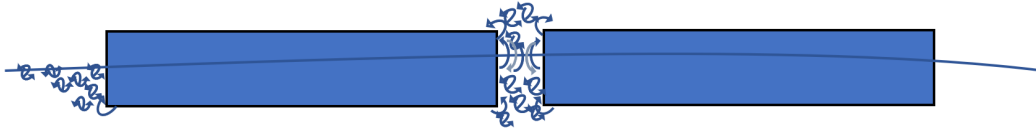


Figure 2.7: Schematic visualisation of the flow behaviour within the gaps between two floaters. Water flows through and onto the floaters, causing a turbulent flow. Some of the water flows back through the gaps, further disturbing the flow. At the outer edges of the system, turbulent flow effects can be observed as well.

overflowing water for irregular wave test I-12 ( $T_p = 11.40s$ ,  $H_s = 4.47$ ,  $\mu = 90^\circ$ ) is shown in figure 2.9. The value of overflowing water on floater 10 is multiplied by 10 to show the trend. Additionally, the wave elevation parallel to floater 10 is shown. As can be seen, the overflowing water has a constant level with additionally higher peaks. These peaks cannot be directly related to the wave elevation, indicating that the overflowing water is influenced by other effects (such as water flowing through the gaps).

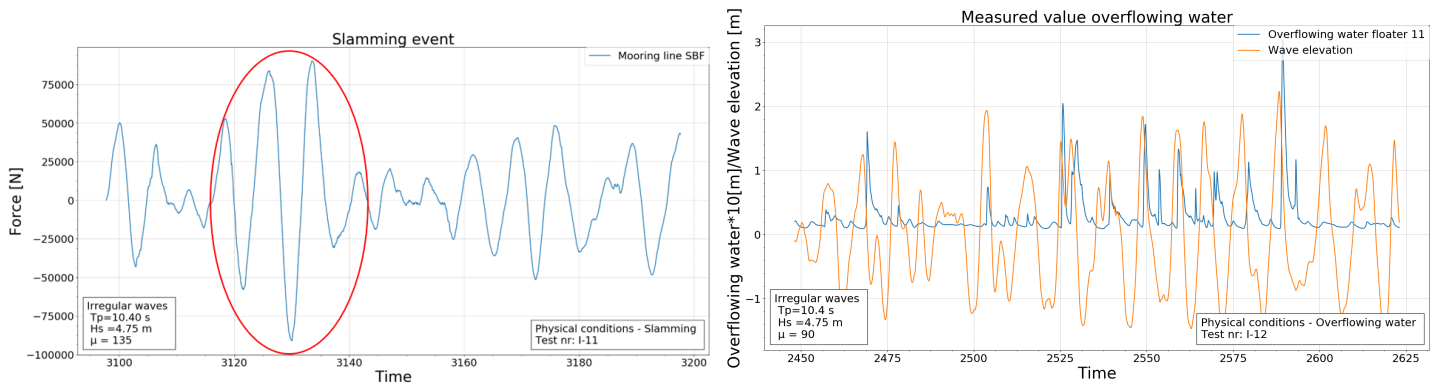


Figure 2.8: Mooring line force in mooring line SBF (starboard front) for a certain moment in time at which slamming occurred.

Figure 2.9: Measured overflowing water for irregular wave test I-12 ( $T_p = 11.40s$ ,  $H_s = 4.47$ ,  $\mu = 90^\circ$ ), compared to the wave elevation. No clear relation can be observed, indicating that other effects influence the overflowing water.

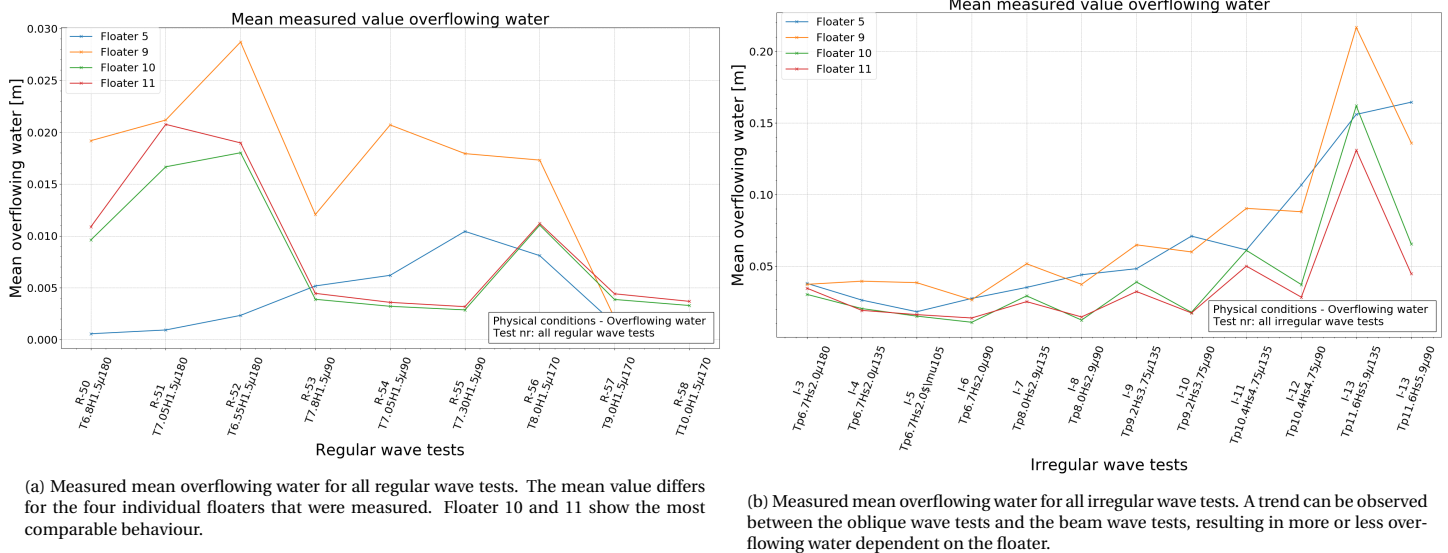
Figure 2.10 shows the mean level of overflowing water for all regular and irregular wave tests. As can be seen in figure 2.10a, the mean level of overflowing water for the regular wave tests is different for the different floaters, depending on the incoming wave angle: Floater 10 and 11 show a clear decrease in mean level for the beam waves compared to the head waves. Overall, the mean water level becomes less for the longer waves (R-56, R-57 and R-58). The mean water level for irregular waves clearly increases for the higher sea states as can be observed in figure 2.10b. Additionally, a difference can be observed for the oblique bridging tests (I-7, I-9, I-11, I-13) compared to the bridging beam tests (I-8, I-10, I-12, I-14), where the oblique waves result in a higher mean level of overflowing water compared to the same wave period and height in beam waves. A strong increase in overflowing water is observed for irregular wave test I-13.

Overflowing water effects can be related to green water effects on deck of a ship, that are subject to the freeboard of the system and the wave height and length of the incoming wave. These green water effects can cause structural damage and influence the dynamics of the system [47]. The former is not of interest in the scope of this research, since the basin model does not contain structures on deck. The latter introduces non-linear behaviour of the systems as a result of the overtopping volume, which would result in differences in weight and buoyancy effects. Additionally, highly nonlinear effects related to breaking waves and air entrapment were observed by Skene [36].

Numerical implementation of overwash (overflowing water) has been studied for thin floating structures such as ice plates [35], highlighting the challenge of numerical modelling of the highly nonlinear phenomenon. This was further studied by Toffoli [41], where the effect of overwash was studied for the transmitted and reflected wave. It was concluded that linear theoretical models become inaccurate for higher wave heights, due to the dissipated energy related to overwash.

### Slamming effects

Slamming effects were observed rarely in the video footages for irregular waves. This slamming is defined as behaviour in which (a part of) the floater is lifted out of the water and then 'slams' back into the wave. The



(a) Measured mean overflowing water for all regular wave tests. The mean value differs for the four individual floaters that were measured. Floater 10 and 11 show the most comparable behaviour.

(b) Measured mean overflowing water for all irregular wave tests. A trend can be observed between the oblique wave tests and the beam wave tests, resulting in more or less overflowing water dependent on the floater.

Figure 2.10: The mean level of overflowing water for floater 5, 9, 10 and 11, given for all regular and irregular wave tests.

slamming causes high impact loads and extra waves and overflowing water, affecting (amongst others) the damping of the system. Figure 2.8 shows a time trace of mooring line force SBF (starboard front) for irregular wave test I-11. The red circle indicates a moment in time in which slamming occurred. As can be seen the mooring line force increases. However, it is not possible to isolate the effect of the slamming in this mooring line force. The slamming can be seen as a one time event that does not directly influence the overall results. Therefore, outliers in behaviour or mooring line forces of the system must be checked for slamming effects.

### Breaking waves

Breaking waves were observed incidental in the video footages for irregular waves. Two different types can be identified:

- Waves breaking before they interact with the structure. This effect is related to the steepness of the wave. The irregular wave tests conducted in the offshore basin have a steepness that is below the wave breaking limit ( $H/\lambda = 0.17$ [15]), when the significant wave height and peak period are used for calculation. However, individual waves in a spectrum can be above this limit, causing the incidental breaking wave effect. Figure 2.11a shows a time trace example of such a breaking wave, indicated with the green arrow. As can be observed, the mooring line force SBF increases.
- Waves breaking during or after interaction with the structure. This effect is related to flow disturbances due to the system behaviour and the overflowing water effects as discussed in by Toffoli [41]. Occurrence of this effect is more difficult to predict due to the nonlinear nature. However, more occurrences were observed for the higher sea states I-13 and I-14. Figure 2.11b shows a time trace example of such a breaking wave, indicated with the green arrow. As can be observed, the mooring line force SBF increases.

Both examples in figure 2.11 show an increase in mooring line force. However, similar to the slamming effects, it is hard to isolate the effect of the breaking wave, as the wave height (strongly related to the breaking wave) also increases, causing higher forces as well.

### Shielding effects

Following from the effects of wave following behaviour, flow disturbances and overflowing water, a shielding effect is introduced, defined as the effect when the second row of floaters experiences a different flow due to the presence of first row. Shielding can be theoretically linked to a different drag force or wave exciting force on the floaters: since the flow is partly shielded by floaters more upstream, these forces might change for the floaters downstream. It has been discussed for side by side moored vessels[27] for viscous effects and hydrodynamic coefficients. Additionally, other applications are studied regarding shielding effects, such as

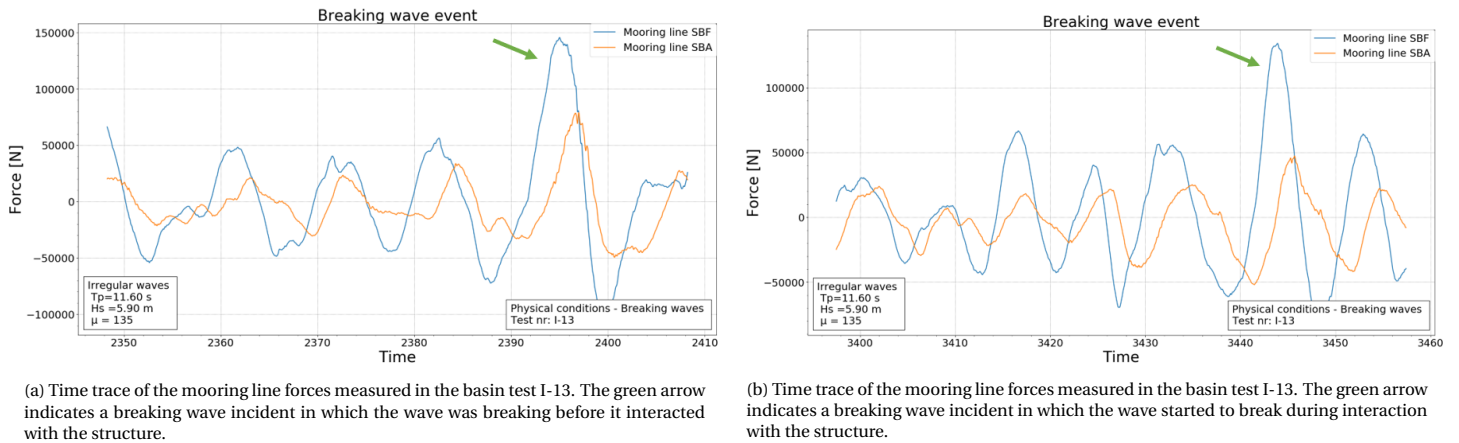


Figure 2.11: Two examples of the effect of breaking wave incidents on the mooring line forces.

cylinders[17, 18, 37]. The studies observe the effect of shielding on the drag coefficients and strong nonlinearities are observed. In this design, the effect will differ for different sea states as a result of the different significance of physical phenomena and is expected to be highly nonlinear as well.

### 2.3. Informational uncertainty

The informational uncertainty of the delivered data from MARIN is addressed in this section. Three different sources for possible uncertainty can be distinguished; The accuracy of the signals, (un)known external factors influencing the signals and the uncertainty of input parameters.

#### Accuracy of signals

Although no detailed information was provided by MARIN on the accuracy of the measurements, the signals are identified as accurate for this study as the measurement equipment and people that performed the tests are considered as highly reliable due to experience within MARIN regarding offshore basin projects.

#### External factors

For this specific experiment, the amount of water flowing over the floaters caused an uncertainty in the measured signal of the location and orientation of the floaters. Due to water drops the signal becomes invalid and this phenomenon could occur for several seconds. Figure 2.12 shows this effect on the signal of the surge motion of two floaters. The invalid part of the signals (depicted with the black arrows) is completed with a spline interpolation through the missing part [31]. It is likely that due to the implemented spline interpolation no large inconsistencies with the reality occur as a result of the water drops. Therefore, this uncertainty is irrelevant for the validation of the locations and orientations of the floaters, also since the comparison will be mainly done on the overall behaviour and not yet on specific points. Since the joint forces are calculated using the locations and orientations of the attached floaters, this effect also influences the joint forces and moments. Unfortunately, the repair done for the motion signals has resulted in the generation of spurious peaks in the joint force signals, which are not coherent with reality. A study performed by Leprou [16] has attempted to remove these spurious peaks without removing real force peaks. Unfortunately no suitable solution was found. The results for joint forces and moments therefore contain a higher uncertainty and will not be analysed extensively in this research.

#### Input data

In addition to uncertainty in the measured data, uncertainties can also stem from errors in the input data. Input data is defined as all parameters used for the experimental setup, such as the locations of anchors, weight of the floaters, stiffness of the springs. All particulars for the floaters and the mooring system are delivered in 3 or 4 significant numbers and the stiffness of the joint is delivered in two significant numbers. Since MARIN has used the same stiffnesses to calculate the joint forces, the same error would be present in the simulation model as in the basin test results. However, there is uncertainty in the actual joint stiffness as implemented in the basin setup.

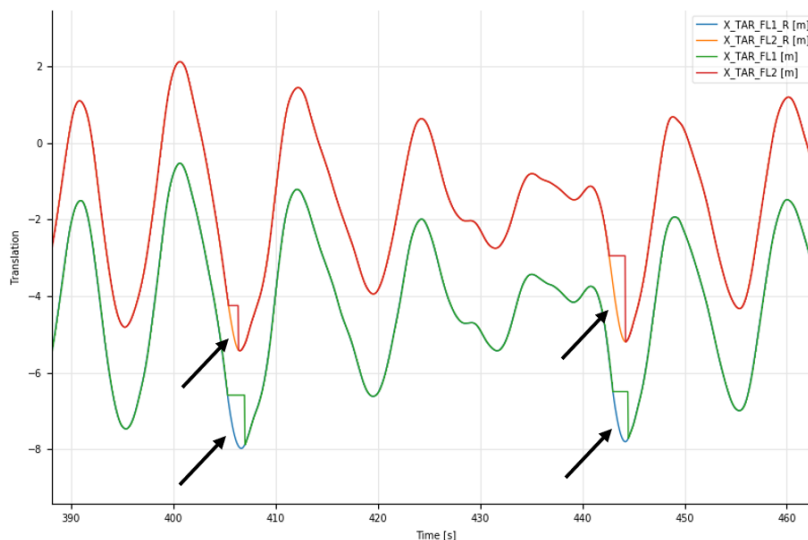


Figure 2.12: This figure shows an invalid signal for the x location of two floaters due to the effect of water drops on the measuring system at the black arrows. This invalid signal is solved by MARIN by fitting a spline interpolation [31].

## 2.4. Conclusion

In this chapter, three aspects of the physical scale model have been presented (the model particulars, the performed tests and the physical conditions present in the experiments). Several conclusions can be drawn regarding the findings from the physical conditions:

- No video footage is available for the decay tests, therefore a gap in information is present on the environment in which these tests took place and the behaviour of the system. The highly damped system in the decay tests increases the chance of parameter uncertainty.
- Several nonlinear effects were observed in the video footage. These effects include viscous damping effects due to water flowing through the gaps, the sharp edges of the system, breaking waves and effects due to the overflowing water.
- The nonlinear effects strongly increase towards the higher sea states and mainly occur (or become more significant) in irregular sea states. This indicates a difference in nonlinear (viscous) effects between irregular and regular sea states.
- Due to the absence of waves in the decay tests, the effects mentioned above are expected to be absent in decaying motions. Therefore, viscous effects in the decay tests differ significantly compared to the irregular and regular waves.
- Contrary to studies on multi-bodies [3, 38], the effect of physical gap resonance and high flow velocities due to relative motions between the floaters (and the related viscous effects) are expected to be of little significance for this study.
- A strong interrelation between the overflowing water, the water through gaps and flow disturbances is present. Isolating one effect is therefore highly challenging (if not impossible).

These conclusions are important for the simulation model structure development presented in chapter 3. Additionally, the possible informational uncertainty has been addressed. Concluding comments are:

- Due to the presence of water drops, there is an uncertainty present in the motion measurement. This uncertainty has a negligible effect on the system motions due to signal improvement done by MARIN. However, effects are present in the joint forces.
- The stiffness of the joints is regarded as the most uncertain input data, but due to small relative motions between the floaters, this uncertainty is not significant in the system behaviour.

Combining the findings on informational uncertainty and that the system behaves as one, it has been decided to leave out the joint forces in the extensive analysis of this research.

# 3

## Simulation model development

The simulation model for the specific application of the multi-body offshore floating solar system was built in aNySIM. This simulation tool has been developed by MARIN.

The goal of this chapter is to present the numerical implementation of the simulation model and all choices that were made during the development of this model. This is related to research question 2 as introduced in chapter 1.

The first section explains the choice for aNySIM whereafter the important assumptions inherent to the frequency-time domain solver are discussed. Thirdly, the underlying mathematical model is presented. Thirdly, the numerical implementation is discussed and verified, addressing the numerical uncertainty in the model. Finally, insight is provided in the significance of specific forces.

### 3.1. aNySIM

aNySIM is a tool developed by MARIN[22] and was selected for several reasons:

- The tool is specialised in multi-body dynamics in offshore operations. Implementation of hydrodynamic and mechanic interaction forces is therefore developed extensively.
- The tool has been extensively verified and validated for all sorts of offshore operations, offering high certainty in the numerical structure of aNySIM. Therefore, the focus of this study could be on the physical behaviour.
- Broad experience and knowledge on the simulation tool is present at MARIN, which was also used during this research.

A downside of the tool is that the hydrodynamic coefficients are obtained using the frequency domain tool DIFFRAC[23], which was not openly available during this research. These calculations have been performed at MARIN.

### 3.2. Model assumptions

Inherently to the frequency-time domain approach, several assumptions and simplifications present within DIFFRAC (frequency domain) and aNySIM (time domain). Additionally, several assumptions based on the physical phenomena analysis of section 2.2.2 are also made for the this study specifically. Both are discussed here.

#### 3.2.1. Assumptions of the frequency-time domain approach

The frequency-time domain solvers DIFFRAC and aNySIM are based on the following assumptions:

##### Linear wave potential

The model is based on potential flow, assuming an ideal flow that can be described with a velocity potential. This potential is set up linearly, neglecting second order (or higher) wave effects. This assumption is correct for low steepness waves, however, when the waves become steeper (defined as  $\frac{H}{\lambda}$  (where  $H$  = wave height and  $\lambda$  = wave length)), the waves start to show nonlinear effects, such as steeper crests and flatter troughs. This

effect is present from  $\frac{H}{\lambda} = 0.001$  [15]. The waves implemented in the basin tests (see appendix A) are all above this limit, however, this effect is expected to be minimal, following from research done on the effect of several non-linearities in simulation models [32].

### Linear hydrodynamic coefficients

Diffraction software is used to calculate the hydrodynamic forces in frequency domain. The hydrodynamic coefficients for added mass and damping are calculated assuming a linearity, where the instantaneous location and orientation of the body is not taken into account. Normally, this assumption is valid for systems that are smaller than the wavelength [32], which is also the case for this model. However, as a consequence of the wave following behaviour as analysed in section 2.2.2 a possible non-linearity in the added mass and hydrodynamic damping could occur. Figure 3.1 visualises this effect schematically. The situation is explained using hydrodynamic coefficients in pitch, but it is applicable for more situations: in the basin tests the relative pitch angle is much smaller when the system acts as a wave follower, which results in lower added mass and damping. aNySIM however, takes into account the absolute pitch angle, which could result in higher forces on the system.

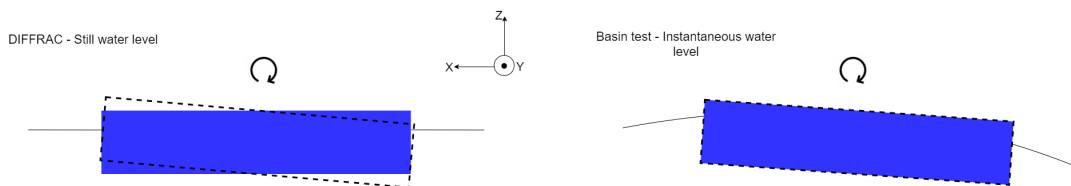


Figure 3.1: Schematic overview of an effect of wave follower behaviour, explained with the pitch added mass. Due to long waves compared to the floater dimensions, the actual pitch motion (relative to the wave angle) is lower than the absolute pitch motion as used in DIFFRAC. This results in a lower added mass and damping in the basin model.

### Wave exciting forces

For wave exciting forces, both first and second order effects are taken into account. The forces are obtained for the mean wetted surface. The calculation method assumes an infinitely low wave height from which force response amplitude operators (RAO's) are determined. Forces on the instantaneous (time dependent) wetted surface are neglected. For large structures where the relative motion between the wave and the structure is minimal, this assumption is valid [32]. However, for this specific system, the ratio between the (significant) wave height ( $H_s$ ) and structure height ( $D$ ) is  $\frac{H_s}{D} \approx 5 - 15$ . This means that the relative motions becomes more significant in relation to the total height of the structure. For higher waves, this can cause nonlinear effects in the wave exciting forces that are not incorporated in the simulation model.

### Overflowing water

The effect of overflowing water is not taken into account since the calculation method assumes an infinitely low wave height in DIFFRAC and the effect is neglected in aNySIM. Following from the analysis in section 2.2.2, the system experiences significant overflowing water. As discussed nonlinear effects are related to overflowing water that are not incorporated (such as volume flux effects and breaking waves). Specifically, the nonlinear effect on the transmitted and radiated wave (discussed by Toffoli [41]) is not incorporated in the linear diffraction model. This simplification is expected to become more visible towards the higher sea states and can also be related to the wave exciting forces.

### Viscous forces

Viscous forces must be added to the model separately to include viscous effects of the flow on the system. Damping coefficients can be obtained using empiric results from which viscous forces can be obtained using the absolute or the relative flow velocity, with both linear and quadratic relations. Following from the analysis in section 2.2.2, viscous effects differ for different regular and irregular wave tests, where highly nonlinear behaviour is present in the gaps between the floaters. The viscous damping implementation using damping coefficients determined from decay tests is a strong simplification of these non-linearities.

### 3.2.2. Assumptions specific for this model implementation

aNySIM offers multiple implementation possibilities for, amongst others, the damping and mooring line implementation. Choices and assumptions made for this specific study are:

### Viscous effects on floaters

Viscous damping effects were assumed to be equal for all floaters. This assumption is based on two reasons. Firstly, since not enough prior knowledge is available on the viscous effects of a multi-body system, the simplest approach was selected to obtain more insight. Secondly, decay tests have only been executed for the entire system, due to which it is not possible to extract relative viscous effects between floaters. However, studies on side-by-side operations emphasise the importance of relative viscous damping effect between two bodies [3]. Additionally, the physical phenomena analysis in section 2.2.2 has demonstrated several factors that might influence the 'shielding' effect. This assumption is therefore a simplification that can result in inaccuracies of the simulation model.

### Viscous effects for 6 degrees of freedom

Viscous forces were implemented for the three directions (surge, sway and yaw) in which a decay test has been performed. Other viscous effects (e.g. in heave, roll, pitch or coupled effects) are neglected. This is done since there is no empirical data available to determine these viscous effects. However, as pointed out in several studies regarding time domain simulations for offshore structures, the viscous roll damping is an important factor [2]. Again, this assumption is a simplification that can result in inaccuracies of the simulation model.

### Hydrodynamic effects on mooring lines

The video findings in section 2.2.2 showed that only very small waves are present around the mooring lines and that the contributions of these hydrodynamic effects on the system behaviour is unknown. Since implementation of hydrodynamic mooring line effects significantly increases the computational time, it was decided to not include these effects. Therefore, the mooring lines are implemented as catenary lines[6], where mass is taken into account but drag and inertia effects are left out.

## 3.3. Mathematical model

The mathematical model that is developed from the basin test model and forms the basis of the aNySIM model is presented in this section, elaborating on the used equation of motion and the forces and moments that are present. Firstly, the system geometry is explained, whereafter the full equation of motion is set up, implementing all forces present.

### 3.3.1. System geometry and notation

The complete system consisting of floaters can be seen in figure 3.2, where 2 coordinate systems are defined. The global coordinate system (GCS), with its origin at the mid centre line of the system on still water level, and the local coordinate system (LCS), with its origin at the horizontal centre of a floater at the keel. The GCS is similar to that in the offshore basin model, but the LCS is defined differently due to predefined definition in the hyd file (this will be explained in section 3.4.2). To distinguish the six degrees of freedom (DOF) from the 12 floaters, different subscripts are used in vector notation. The motion, velocity and acceleration vectors are written as  $\mathbf{u}_{k=1to12}$ ,  $\dot{\mathbf{u}}_{k=1to12}$  and  $\ddot{\mathbf{u}}_{k=1to12}$  respectively for all 12 floaters. For a single floater this results in the following motion vector:  $\mathbf{u}_{k=1} = [x_1, y_1, z_1, \phi_1, \theta_1, \psi_1]$ . The forces (and moments) present on one floater are denoted as  $F_{j=1to3}$  and  $M_{j=3to6}$

### 3.3.2. System description single body system

To describe the system as built in the basin, the problem is simplified to 1 floater. The behaviour can be described using Newton's second law:

$$\mathbf{F}_{j=1to3} = m \cdot \ddot{\mathbf{u}}_{j=1to3}(t) \quad (3.1)$$

$$\mathbf{M}_{j=4to6} = I \cdot \ddot{\mathbf{u}}_{j=4to6}(t) \quad (3.2)$$

Where:

- $F_{j=1to3}$  is the resulting force acting on the centre of gravity (G) of the floater in the j-th degree of freedom.
- $M_{j=4to6}$  is the resulting moment acting on the centre of gravity (G) of the floater in the j-th degree of freedom.
- $\ddot{\mathbf{u}}_{j=1to6}$  is the acceleration of the floater in all 6 DOF
- $m$  is the mass of the floater ([kg])

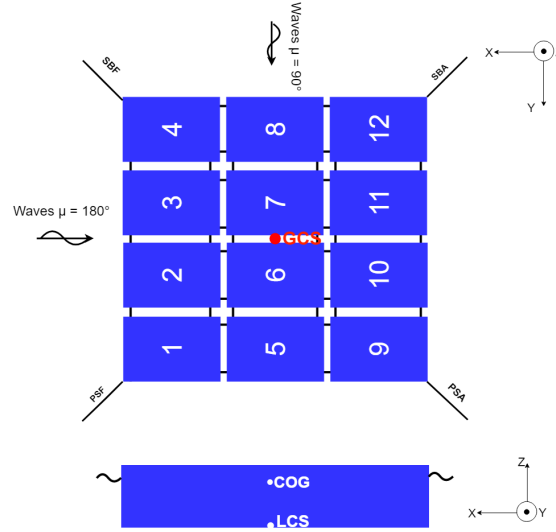


Figure 3.2: Global and local coordinate systems used for the floaters in the mathematical model

- $I$  is the mass moment of inertia ( $[kgm^2]$ )

To solve for this system, the assumption of an ideal (potential flow) is used, which assumes an irrotational flow and a non-viscous fluid. This means that the forces on the body can be described as the integration of the pressure over the submerged surface. Rewriting Newton's second law for this specific system gives:

$$m \cdot \ddot{\mathbf{u}}_j(t) = \mathbf{F}_g - \int_{S(t)} P(t) \mathbf{n} dS + \mathbf{F}_m \quad (3.3)$$

$$I \cdot \ddot{\mathbf{u}}_j(t) = \int_{S(t)} P(t) \mathbf{r} \times \mathbf{n} dS + \mathbf{M}_m \quad (3.4)$$

Where:

- $\mathbf{F}_g$  is the gravitation force
- $S(t)$  is the instantaneous wetted surface
- $P(t)$  is pressure on the body
- $\mathbf{n}$  is the normal vector pointing outwards on the surface
- $\mathbf{r}$  is the distance vector from the surface to the COG
- $\mathbf{F}_m$  and  $\mathbf{M}_m$  are the mechanical interaction forces and moments

The pressure is derived using Bernoulli's law:

$$P(t) = -\rho g z - \rho \frac{\delta \Phi(t)}{\delta t} - \rho \frac{|\nabla \Phi(t)|^2}{2} \quad (3.5)$$

Where  $\Phi$  = the potential flow and  $\rho$  = the density of seawater. The potential describing the flow can be split into three potentials, assuming the potentials are summed linearly. These potentials are:

$$\Phi = \Phi_I + \Phi_D + \Phi_R \quad (3.6)$$

Where:  $\Phi_I$  = Incoming wave potential,  $\Phi_D$  = Diffraction potential and  $\Phi_R$  = Radiation potential. Combining equations (3.3), (3.4), (3.5) and (3.6), gives the following forces acting on the body, that will be explained in the next sections:

- Hydrostatic forces

- Wave exciting forces
- Radiation forces
- Mechanical interaction forces
- Viscous forces

### Hydrostatic forces

The hydrostatic forces can be written as:

$$F_{st} = C\mathbf{u} \quad (3.7)$$

Where  $C$  is the restoring matrix for 1 body. For surge, sway and pitch this restoring coefficient is 0, ie. there is no restoring force. For heave, roll and pitch, the restoring coefficient is determined with:

$$c_z = \rho g A \quad (3.8)$$

$$c_{xx} = GM_t \rho g V \quad (3.9)$$

$$c_{yy} = GM_l \rho g V \quad (3.10)$$

Where  $A$  is the waterline area,  $GM_t$  is the transversal GM and  $GM_l$  is the longitudinal GM. To construct the restoring matrix at COG from the restoring coefficients, a translation is used with the floater fixed distances:

$$\Delta x = LCF - LCG \quad (3.11)$$

$$\Delta y = TCF - TCG \quad (3.12)$$

$$\Delta z = T - KG \quad (3.13)$$

Where LCF and TCF are the longitudinal and transversal centres of floatation respectively and LCG and TCG are the longitudinal and transversal centre of gravity respectively.  $T$  is the draft and  $KG$  is the vertical centre of gravity. Applying these distances results in the following restoring matrix:

$$C = \begin{bmatrix} 0 & 0 & 0 & 0 & 0 & 0 \\ 0 & 0 & 0 & 0 & 0 & 0 \\ 0 & 0 & c_z & \Delta y c_z & -\Delta x c_z & 0 \\ 0 & 0 & \Delta y c_z & c_{xx} + (\Delta y)^2 c_z & -\Delta x \Delta y c_z & 0 \\ 0 & 0 & -\Delta x c_z & -\Delta x \Delta y c_z & c_{yy} + (\Delta x)^2 c_z & 0 \\ 0 & 0 & 0 & 0 & 0 & 0 \end{bmatrix} \quad (3.14)$$

### Wave exciting forces

The wave exciting forces and moments consist of an incoming part and a diffracted part:

$$F_{ex} = F_{fk} + F_{dif} \quad (3.15)$$

$$M_{ex} = M_{fk} + M_{dif} \quad (3.16)$$

Using Bernoulli's law, the incoming and diffracted potential lead to a force and moment:

$$F_{ex} = \rho \int_{S(t)} \frac{\delta(\Phi_I + \Phi_D)}{\delta t} + \frac{|\nabla(\Phi_I + \Phi_D)|^2}{2} \mathbf{n} dS \quad (3.17)$$

$$M_{ex} = \rho \int_{S(t)} \frac{\delta(\Phi_I + \Phi_D)}{\delta t} + \frac{|\nabla(\Phi_I + \Phi_D)|^2}{2} \mathbf{r} \times \mathbf{n} dS \quad (3.18)$$

$$(3.19)$$

These equations lead to forces up to 5th order, using perturbation theory[33]. For this mathematical model, only the first order excitation forces and drift forces are derived. The first order wave forces are obtained from the linear term in the Bernoulli equation, integrated over the mean wetted surface ( $S$ ). This results in:

$$F_{ex1} = \rho \int_S \frac{\delta(\Phi_I + \Phi_D)}{\delta t} \mathbf{n} dS \quad (3.20)$$

$$M_{ex1} = \rho \int_S \frac{\delta(\Phi_I + \Phi_D)}{\delta t} \mathbf{r} \times \mathbf{n} dS \quad (3.21)$$

$$(3.22)$$

The method developed by Pinkster [33] for mean wave drift forces has been used to evaluate the second order forces. This method considers the fully nonlinear Bernoulli equation and integration over the instantaneous wetted surface. Using perturbation theory, only second order forces are evaluated,  $F_{ex2}$ . The second order incoming potential is neglected.

The linear excitation force and the second order drift forces are combined in the excitation force as:

$$F_{ex} = F_{ex1} + F_{ex2} \quad (3.23)$$

$$M_{ex} = M_{ex1} + M_{ex2} \quad (3.24)$$

### Radiation forces

If the body is given a motion in a direction, waves will be radiated. The (first order) force resulting from this radiation can be written as the pressure integration of the (linear) radiation potential over the mean wetted surface:

$$F_{rad} = \rho \int_S \frac{d\Phi_R}{dt} n dS \quad (3.25)$$

The radiation force can also be described as a part in phase with the acceleration of the body: added mass, and a part in phase with the body velocity: hydrodynamic damping. Note that the motion of the floater in one direction causes waves to radiate in all directions, ie. the surge motion results in a radiation force in all other DOF as well. The radiation force (and moments) can be rewritten as:

$$F_{rad} = A(\omega)\ddot{\mathbf{u}} + B(\omega)\dot{\mathbf{u}} \quad (3.26)$$

Where  $A(\omega)$  is the frequency dependent added mass matrix and  $B(\omega)$  the frequency dependent hydrodynamic damping matrix of 1 floater.

### Mechanical interaction forces

Furthermore, the moving body also encounters mechanical interaction forces due to joints between the floaters and the mooring lines. The joint force is calculated by a simple spring system:

$$F_{joint} = S(\mathbf{u}^1 - \mathbf{u}^2) \quad (3.27)$$

where  $S$  is the stiffness matrix of the joint and  $\mathbf{u}^1 - \mathbf{u}^2$  is the distance vector between two floaters. The mooring line forces were calculated using a catenary line, where the force is a combination of the gravitational forces acting on the line and the stiffness in the line.

The mechanical interaction force can now be written as:

$$F_m = F_{mooring} + F_{joint} \quad (3.28)$$

### Viscous forces

The potential theory used to describe the wave exciting and radiation forces does not account for viscous effects, since it assumes an ideal flow which is non-viscous. However, incorporation of these effects is necessary to complete the mathematical model for a real flow. The additional force due to viscous effects can be split into 2 parts:

- Skin friction or friction drag on the bodies (floater, mooring line, joint)
- Form drag due to separation of the flow

Skin friction is a result of the boundary layer that forms on the body in a viscous flow, giving a shear stress. Depending on a laminar or turbulent flow, a different velocity profile needs to be used and the mathematical description of this skin friction is not so straightforward [45].

In addition to the skin drag calculated on a flat plate, the body shape has to be taken into account as well. This can cause a pressure gradient in the boundary layer, resulting in the flow separating from the body at a certain point.

As concluded in section 2.4, different viscous effects are present for the decay, regular and irregular wave tests. This means that mathematically, the ratio between skin friction and form drag changes between the tests. For example: In the longer regular wave tests, less flow disturbances were observed in comparison to

the irregular wave tests (see section 2.2.2 on the flow disturbances). Fewer flow disturbances can be related to fewer flow separation. Therefore, the skin friction on the floater is expected to be higher in the longer regular wave tests.

In general, the entire drag on a body is calculated using a drag coefficient, which depends on both the friction as form drag of the body. The drag can then be calculated with:

$$F_{drag} = \frac{1}{2} \rho C_d A_c \mathbf{u}_r |\mathbf{u}_r| \quad (3.29)$$

Where  $\mathbf{u}_r$  is the relative external flow (relative to the floater),  $C_d$  is the drag coefficient that is dependent on the shape of the body and  $A_c$  is the cross sectional area. However, this equation is not as straightforward as it looks, since it now only depends quadratically on the external flow, whereas a linear relation can be found for the friction drag as well. Therefore, the mathematical implementation of the viscous damping on the floaters was composed as:

$$F_v = B_v^{(1)} \dot{\mathbf{u}} + B_v^{(2)} \mathbf{u}_r |\mathbf{u}_r| \quad (3.30)$$

Here  $B_v^{(1)}$  is the linear viscous damping coefficient matrix and  $B_v^{(2)}$  the quadratic viscous damping coefficient matrix. This quadratic viscous damping coefficient is related to the drag coefficient as:

$$C_d = \frac{2B_v^{(2)}}{\rho A} \quad (3.31)$$

### Equation of motion

Newton's second law can be rewritten into the equation of motion in frequency domain, incorporating all present forces:

$$(m + A(\omega)) \cdot \ddot{\mathbf{u}} + B(\omega) \dot{\mathbf{u}} + C\mathbf{u} = \mathbf{F}_{tot} \quad (3.32)$$

The force  $\mathbf{F}_{tot}$  is a summation of the remaining forces:

- Wave exciting forces  $F_{ex}$
- Viscous forces  $F_v$
- Mechanical interaction forces  $F_m$

Equation (3.32) is dependent on frequency and can therefore not be solved for a time dependent problem. Conversion of the added mass and damping to time domain is required. This results in:

$$(m + A) \cdot \ddot{\mathbf{u}} + \int \int_{-\infty}^t R(t - \tau) \dot{\mathbf{u}}(\tau) d\tau + c\mathbf{u} = F(t) \quad (3.33)$$

$F(t)$  is the sum of arbitrarily in time varying external forces.  $A$  is the added mass at infinite frequency in time domain and  $R$  is the retardation function, both developed by using Cummins' equation [7]:

$$R(t) = \frac{2}{\pi} \int_0^\infty b(\omega) \cos(\omega t) d\omega \quad (3.34)$$

$$A = a(\omega) + \frac{1}{\omega} \int_0^\infty R(\tau) \sin(\omega t) d\tau \quad (3.35)$$

Here  $a(\omega)$  is the added mass at one specific frequency.

### 3.3.3. System description multi-body system

The equation of motion developed in the sections above must be extended to multiple bodies to describe the design. In addition to the equation of motion for all 12 bodies, a coupling between the bodies is present, both hydrodynamical as mechanical.

As an example of all coupled equations of motions, the full equation is derived for  $n = 3$  bodies. The index

numbering is used for the number of the body:

$$\begin{aligned}
& \left( \begin{bmatrix} [M_{11}] & 0 & 0 \\ 0 & [M_{22}] & 0 \\ 0 & 0 & [M_{22}] \end{bmatrix} + \begin{bmatrix} [A_{11}] & [A_{12}] & [A_{13}] \\ [A_{21}] & [A_{22}] & [A_{23}] \\ [A_{31}] & [A_{32}] & [A_{33}] \end{bmatrix} \right) \times \ddot{\mathbf{u}}_{1to3} \\
& + \begin{bmatrix} \int_0^t R_{11}(t-\tau) & \int_0^t R_{12}(t-\tau) & \int_0^t R_{13}(t-\tau) \\ \int_0^t R_{21}(t-\tau) & \int_0^t R_{22}(t-\tau) & \int_0^t R_{23}(t-\tau) \\ \int_0^t R_{31}(t-\tau) & \int_0^t R_{32}(t-\tau) & \int_0^t R_{33}(t-\tau) \end{bmatrix} \times \dot{\mathbf{u}}_{1to3} \\
& + \begin{bmatrix} C_{11} & 0 & 0 \\ 0 & C_{22} & 0 \\ 0 & 0 & C_{33} \end{bmatrix} \times \mathbf{u}_{1to3} = \begin{bmatrix} \mathbf{F}_1 \\ \mathbf{F}_2 \\ \mathbf{F}_3 \end{bmatrix}
\end{aligned} \tag{3.36}$$

Here:

- $M_{11}$  is the inertia matrix for 1 body. No coupling exists between the bodies concerning the inertia terms.
- $[A_{11}]$  is the added mass matrix for body 1
- $[A_{12}]$  is the added mass of body 1 due to motions of body 2.
- $[\int_0^t R_{11}(t-\tau)]$  is the retardation function matrix for body 1
- $[\int_0^t R_{12}(t-\tau)]$  is the retardation function matrix of body 1 due to motions of body 2.
- $\mathbf{u}_{1to3}, \dot{\mathbf{u}}_{1to3}, \ddot{\mathbf{u}}_{1to3}$  are the motion, velocity and acceleration vectors respectively for body 1, 2 and 3.
- $\mathbf{F}_1$  is the external force vector acting on body 1, consisting of:

Exciting wave forces and moments

Mechanical forces and moments

Viscous forces and moments

For  $n = 12$  bodies, the full equation of motion can than be written as:

$$\sum_{j=1}^{6 \cdot n} (M_{kj} + A_{kj}) \ddot{\mathbf{u}}_k + \int \int_{-\infty}^t R_{kj}(t-\tau) \dot{\mathbf{u}}_k(\tau) d\tau + C_{kj} \mathbf{u}_k = \mathbf{F}_k(t) \tag{3.37}$$

for  $k = 1, 2, \dots, n$

The index numbering now continues for all bodies, where  $n$  is the number of bodies. This means that  $j = 1 \dots 6$  accounts for all 6 motions and  $k = 1$  accounts for all 6 DOF for the first body. Now the full equation of motion has been set up, the next step is to implement it in aNySIM. This is discussed in the next section.

## 3.4. Numerical model

In this section a general overview of the applied method in aNySIM is given, whereafter the numerical implementation that is explained in more detail. To describe the model setup, use has been made of the theory and introduction document of aNySIM [22], [43] the in-house prepare tool of aNySIM (Prepare) and the technical report of S. Weller and S. Gueydon [44]. Appendix C gives an overview of the exact details as implemented.

### 3.4.1. General overview aNySIM and DIFFRAC

aNySIM is a time domain simulation program that can be used for multi-body dynamics in offshore operations. The response of bodies in waves due to mechanical and hydro-mechanical forces is solved for each time step, determining the position, velocity and acceleration of all separate bodies, solving the set of nonlinear equations of motion (3.37).

#### Units and coordinate system

Units are defined in the International System of Units [22], see table 3.1 for an overview. The same two right-handed Cartesian coordinate systems can be distinguished as explained in section 3.3.1, see figure 3.2.

Table 3.1: SI Units

Quantity	Unit symbol	Unit name	SI base units
Length	$m$	Metre	$m$
Mass	$kg$	Kilogram	$kg$
Time	$s$	Second	$s$
Temperature	$K$	Kelvin	$K$
Angle	$rad$	Radian	$mm^{-1}$
Anqular frequency	$\omega$	Omega	$s^{-1}$
Force	$N$	Newton	$kgms^{-2}$

### Solving method

To solve for equation (3.37), aNySIM is built up as can be seen in figure 3.3. Firstly, the added mass, damping coefficients and the wave excitation forces are determined in the frequency domain solver DIFFRAC[23]. The results from DIFFRAC are loaded into aNySIM using a hyd (hydrodynamic) file. Secondly, the requested environment is defined in aNySIM, this can contain wind, waves, current and the bathymetry. Thirdly, an integrator is used to solve for the equation of motion (3.37). Within this integrator, the hydromechanical interaction forces, mechanical forces and viscous forces are calculated for each time step. To do so, the input file from DIFFRAC needs to be converted from frequency to time domain. Finally, an output file is generated containing time traces of the desired quantities.

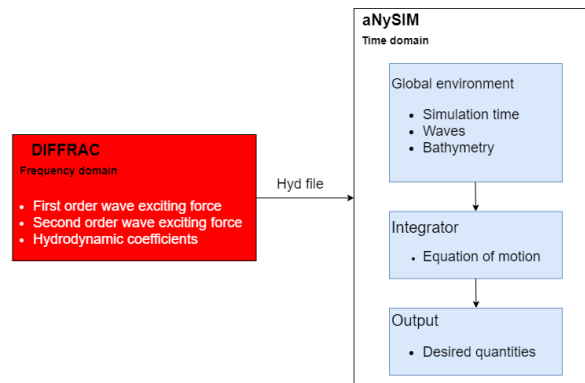


Figure 3.3: Overview of the set up of aNySIM in combination with DIFFRAC. The aNySIM model uses the hyd file obtained in DIFFRAC as input for the hydrodynamic coefficients.

### 3.4.2. DIFFRAC - Hyd file

The first step in the simulation process is the diffraction analysis done in the frequency domain tool DIFFRAC to obtain the required hyd file. A note must be made that the DIFFRAC calculations are performed by MARIN, where the geometry of the full scale system is used. In DIFFRAC, hydrodynamic properties for moored bodies can be calculated. The following hydrodynamic properties have been calculated in the frequency domain, for frequencies  $\omega$  in the range from 0 to 8 rad/s, with incoming wave directions  $\mu$  from 0 to 360 degrees:

- First order excitation force
- Second order excitation force
- Hydrodynamic coefficients

To calculate these properties, the diffraction and radiation problem is solved by solving a governing set of the linearised equations using a Green's function. For more detail on the supporting theory, the DIFFRAC user guide can be consulted [23]. Finally, the results from DIFFRAC are converted to a hydrodynamic (hyd) file that is loaded into aNySIM. A more extended explanation and verification of these aspects can be consulted in appendix B.

### 3.4.3. aNySIM - XMF file

aNySIM is based on the Extensible Modelling Framework (XMF), a software toolkit. The XMF input file is read by the XMF system and the related dynamic content libraries are loaded in which details regarding hydrodynamic, integration or environment specifics. Figure 3.4 shows an overview of all parts within the XMF file, specified for the developed model:

- The global environment (Waves and bathymetry for specific sea state)
- The global hydrodynamic database (This is the hyd file loaded from DIFFRAC)
- The integrator object that performs the actual time domain simulation. Within this integrator object, childs are collected. These childs include the floaters, joints and mooring lines.
- The output object, in which the desired quantities can be defined to generate the output files.

All blocks on the left side are objects. The grey block "Nodes" contains specific information that has to be specified for the dynamic content library concerned. Within an object, childs are defined if applicable. These childs have nodes as well. The childs with a grey box are further defined in a sub model, linking to another XMF file. These childs may contain more (sub)childs. Details of the main XMF-file are shown in appendix C.1

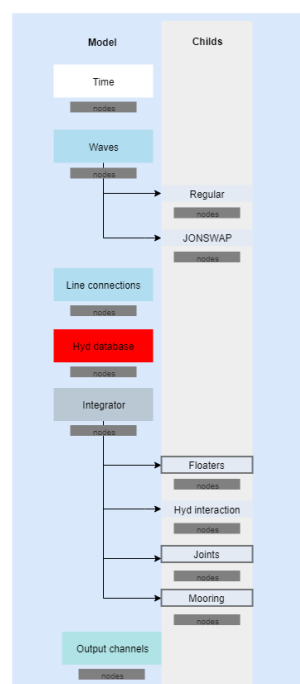


Figure 3.4: Overview of the main XMF file used for the aNySIM model

The following sections will elaborate on the different objects of the main XMF-file. Using figure 3.4, the **objects** will be annotated as a subsection, the **childs** of objects in *italic and bold* and the *childs* of childs in *italic*.

#### Time

A time step is defined for the integration of the equation of motion. This time step influences the accuracy and duration of the calculation. The time step required for a stable simulation has been studied in order to minimise the computational time. Results are shown in appendix E.1.

#### Waves

In the environment used in the simulations, both regular and irregular waves are considered. These waves define the wave exciting force that is subjected to the system. In addition to the pre-defined spectra (regular or JONSWAP), a user defined time trace can also be implemented, which consists of the wave height at a specific location for every time step.

### Hydrodynamic database

The hydrodynamic database from DIFFRAC is loaded into the XMF file so that it can be used in other objects and childs.

### Integrator

In the main part of the XMF file, the equation of motion is solved by means of an integrator, in this case a Runge Kutta 4 (RK4) scheme. See details in appendix E.1.

### Floater

All floaters are defined in the same submodel file. Here the dimensions, mass and initial positions of the floaters are defined, as well as the locations of possible mooring lines or joints. This file contains the hydrostatic forces, wave forces and viscous forces applied to a floater. All details are displayed in appendix C.2.

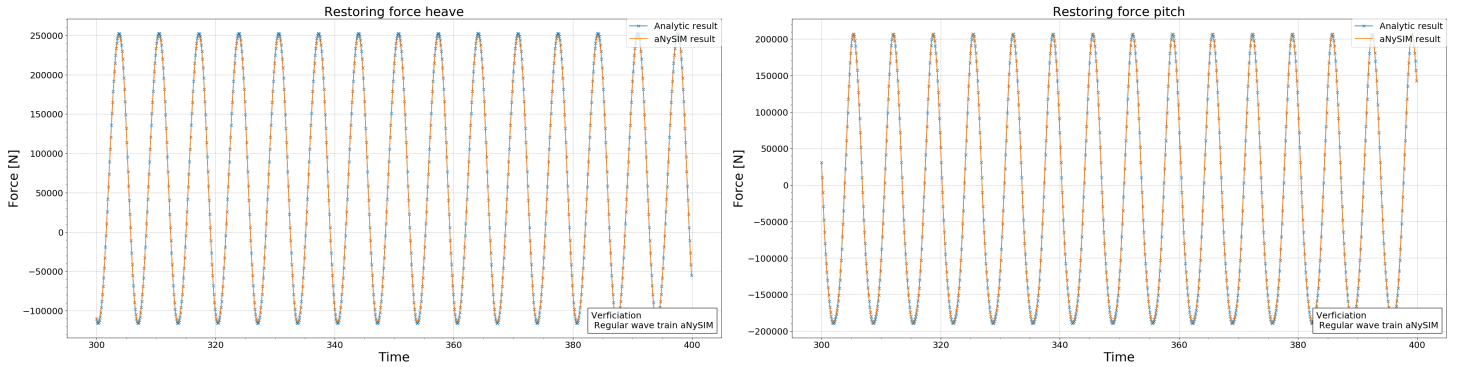
#### Force series:

An external force can be applied to the COG of the floaters, used for the decay tests to give the floaters an initial location.

#### Linear hydrostatics:

The linear hydrostatics are retrieved from the hydrodynamic database for the specific floater. This restoring matrix as shown in 3.14 is implemented in equation (3.37).

The restoring force is implemented in aNySIM using the linear restoring matrix. To verify the linear hydrostatics in aNySIM, the restoring force in heave and pitch is calculated analytically using the same restoring matrix in 3.14. Results are shown in figure 3.5, where the results obtained from aNySIM and the analytical calculations show the exact same results for both the force in heave direction (figure 3.5a) as the moment in pitch direction (figure 3.5b)



(a) Comparison of the restoring force in heave direction for a given heave displacement in aNySIM. The analytic solution is equal to the aNySIM result.

(b) Comparison of the restoring moment in pitch direction for a given a pitch displacement in aNySIM. The analytic solution is equal to the aNySIM result.

Figure 3.5: Restoring force in heave and moment in pitch comparison of aNySIM results with analytically calculated value for 1 floater

### Excitation

The first order excitation force is loaded directly from the hydrodynamic data base, depending on the applied environmental load. This excitation force consists of the Froude Krylov force and the diffraction force.

#### Second order excitation force

The second order excitation force is loaded directly from the hydrodynamic data base, depending on the applied environmental load. This second order force consists of the mean and low frequency wave drift force. All other second order (and higher) terms are neglected.

#### Linear damping, drag force

In addition to the hydrodynamic damping calculated in DIFFRAC and implemented in aNySIM in the **Hydrodynamic interaction**, the system will experience more damping effects as explained in 3.3.2. The different methods to determine the linear and quadratic damping coefficients is elaborated on in 4.2.1. The damping implementation of (3.30) is dependent on both the absolute velocity of the floater as the relative flow velocity. aNySIM incorporates this load due to the relative velocity based on non-dimensional polar coefficients. The drag force vector calculated as follows:

$$F_{drag}(\alpha) = \frac{1}{2} \rho |\mathbf{v}| AC_p(\alpha) \quad (3.38)$$

Table 3.2: Verification of the damping implementation in aNySIM. The linear damping force and drag are compared to analytically calculated values.

Designation	Magnitude
Instantaneous wave height [m]	0.55
Wave angle [deg]	180
Floater surge velocity [m/s]	-1.23
Wave velocity [m/s]	-0.50
Linear damping coefficient $b_1^{(1)}$ [Ns/m]	889.20
Linear damping force analytic [N]	1093
Linear damping force aNySIM [N]	1093
Drag force analytic [N]	140
Drag force aNySIM [N]	140

Where:

- $\alpha$  = the angle of attack of the flow
- $|\mathbf{v}|$  = the relative horizontal velocity. This is calculated with  $\dot{x}_r^2 + \dot{y}_r^2$ , in which  $\dot{x}_r$  and  $\dot{y}_r$  are the relative flow velocities of the floater in x and y direction.
- $A$  = the cross sectional area
- $C_p$  = the polar coefficient vector.

The relation for the force is quadratic with the relative velocity, and therefore, to determine the polar coefficient, the drag coefficient is used, dependent on the flow angle of attack. This results in:

$$C_{px}(\alpha) = C_d \cos(\alpha) \quad (3.39)$$

A vector for  $\alpha$  is defined from  $\alpha = 0$  to 350degrees. Analysing the difference between polar coefficients and quadratic damping for a floating solar structure in regular waves, small improvements can be observed for polar coefficients [34]. Following this research, the implementation of polar coefficients is implemented in this aNySIM model instead of the quadratic damping term. The final viscous force is implemented as:

$$F_v = Bv^{(1)} \cdot \mathbf{u}_1 + \frac{1}{2} \rho |\mathbf{v}| A C_p(\alpha) \quad (3.40)$$

To verify the implementation of the viscous force, regular wave tests have been performed with different wave directions. The viscous forces (linear and drag) will be compared with analytic calculations using the mathematical formulations 3.30 and 3.38. Table 3.2 gives results for a regular wave as implemented in aNySIM, comparing the analytic solution to the aNySIM result for the linear damping and drag force. As can be observed, both analytically calculated values for the damping forces give the same results, verifying the damping implementation

#### **Hydrodynamic interaction**

The hydrodynamic database of the floaters consists of added mass and damping for the individual floaters but also interactions between floaters. Because of this interaction, the motions of the floaters cannot be calculated separately. This hydrodynamic interaction between the floaters is taken into account, by loading the added mass and damping information from the global hyd file for the specified body. The added mass and damping are then converted from frequency domain to time domain using Cummins' equation 3.35. As concluded by [3], the hydrodynamic coupling between bodies is crucial in simulation accuracy. Appendix B studies this effect in further detail. An important comment is that numerical gap resonance effects can be observed in the added mass and damping coefficients due to the hydrodynamic coupling, but that these resonance effects occur round a frequency of 4 rad/s. The wave exciting frequency range for this study is below 2 rad/s, and therefore these numerical resonance effects are not relevant. This was explained in further detail by Koppes [14].

#### **Joints**

The joints connect two floaters and are implemented as springs with six degrees of freedom. In all six directions a spring stiffness and mechanical damping constant is defined by the properties of the material. The properties of a joint are defined at the middle of the two pontoons it connects. A joint can be located at the fore or aft between two pontoons side by side, and it can be located at port side or starboard between two

pontoons positioned opposite of each other. The force in a joint is calculated as the relative distance  $\Delta x_e$  and relative orientation  $\alpha_e$  offset between two attached floaters multiplied by a 6x6 stiffness matrix  $\mathbf{S}_e$ , see equation (3.41). This results as moments and forces at the attachment points on floater 1 and 2.

For numerical stability, mechanical damping needed to be added to the joint implementation. Since the mechanical damping of a spring is negligible in reality, it is desired to keep this damping as small as possible. A study on this damping implementation is shown in appendix E.2.

$$\begin{Bmatrix} \mathbf{f}_e \\ \mathbf{m}_e \end{Bmatrix} = \mathbf{S}_e \begin{Bmatrix} \Delta x_e \\ \alpha_e \end{Bmatrix} \quad (3.41)$$

### Mooring

All four mooring lines are set up in the same way, mimicking the physical mooring line as implemented in the basin (see figure 2.1). Important aspects of the mooring lines are:

- The mooring line dynamics are based on the Catenary effect of the line and the springs implemented for stiffness
- The two springs are implemented between the mooring lines that have a different stiffnesses and work in series for small offsets
- Spring B, with the smallest stiffness, has a maximum length, after which the axial stiffness of the line is effectively determined by spring A.

The mooring lines were implemented as a Composite Catenary line; a quasi-static solution of a line with mass, neglecting hydrodynamic forces.

The Composite catenary line end point is found by a numerical rootfinder, the Broyden algorithm [22]. However, on time step  $t = 0$ , the line shape and end point is still unknown. This results in an Broyden error in the aNySIM solver on  $t = 0$ , which can be ignored if the Broyden algorithm converges.

All details of the mooring set up are shown in appendix C.3. To mimic the specific mooring line parts as implemented in the basin tests, the Composite Catenary line is divided in segments, each corresponding to a different part of the line as visualised in figure 2.1.

The composite catenary line as implemented in aNySIM is verified using benchmark tests from the aNySIM documentation[22], where simplified problems are used. Additionally, a static offset test used to see if the behaviour is according the expectations. In figure 3.6 the forces in all four mooring lines are shown.

As can be seen, the lines show symmetric behaviour, with two different shapes. For a positive x displacement, the aft lines are stretched according to the spring stiffness as implemented. For a negative x displacement, the aft lines show a nonlinear decrease in force, caused by the catenary effect of the lines.

Furthermore, the slope of the mooring line force does not change for larger offsets. This means that the mooring line force follows a linear relation. However, as explained in section 2.1.1, the basin model consists of nonlinear mooring lines, by implementing a maximum length for spring B. The set up has not been mimicked in the aNySIM model as no suitable implementation could be found. This assumption still results in valid behaviour for motions within a range of 10 metre offset in x and y direction, in which spring B has a length smaller than 13 metres. This is related to a mooring line force of 480.7kN. This means that for heavy sea states with large displacements, the model is not valid. Appendix G.4 shows the maximum measured force in all 4 mooring lines for all irregular wave tests. Four tests exceed the limit of 480.7kN, see table 3.3, for which results are not valid. These tests are all within the ULS range of the tests, which are outside the scope of this study.

Table 3.3: Particulars of irregular wave tests that exceed maximum force

Basin test nr	Name	Wave height[m]	Wave period [s]	Wave angle[°]	Water depth
16	Ultimate limit state	5.46	12.82	135	25
17	Ultimate limit state	7.30	12.82	105	25
18	Ultimate limit state	6.35	13.09	90	25
21	Ultimate limit state with slack	7.47	12.82	105	22.5

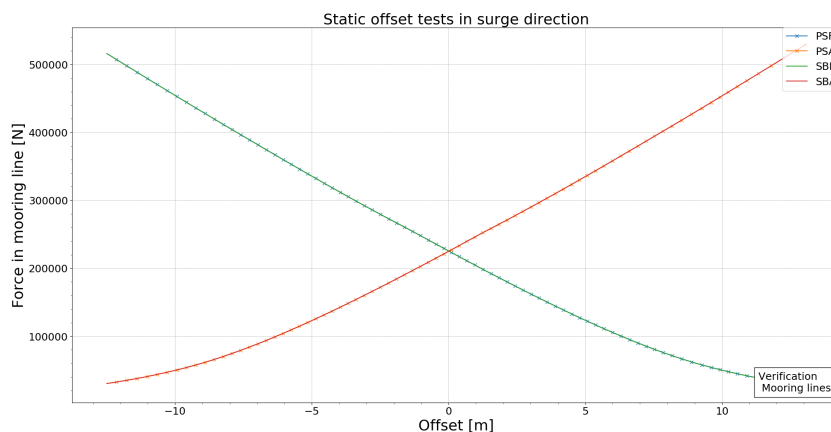


Figure 3.6: Forces in all four mooring lines for a static offset test obtained from the aNySIM simulation. The lines show symmetric behaviour, and a linear relation with a direction coefficient that is equal to the spring stiffness. This verifies the mooring stiffness implementation.

### Output channels

The final object in the XMF file holds the output channels of which a time trace is logged into a results file. Data can be obtained for the motions in 6DOF of the floaters and for all forces and moments acting on the floaters, joints and mooring lines.

## 3.5. Preliminary sensitivity study

With the numerical model set up in aNySIM, some preliminary sensitivity studies were performed to get a better insight in the behaviour of the system.

### Governing forces for surge and sway behaviour

The behaviour of the system can be described with the equation of motion as shown in equation (3.37). Within this equation, three dominating force (and moments) groups can be distinguished:

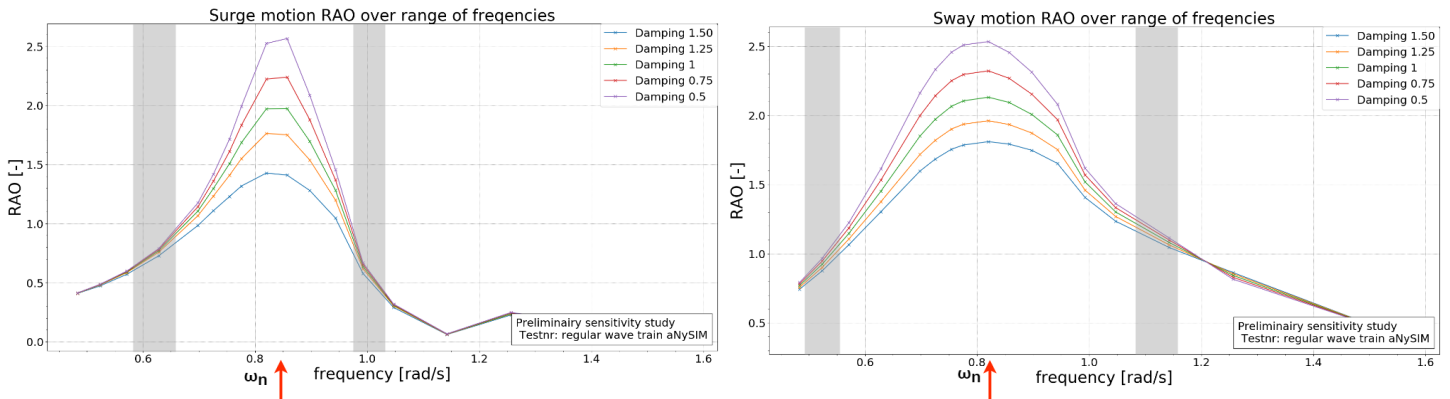
1. Inertia forces, in phase with the acceleration of the system, are governing in longer waves, with low wave frequencies
2. Damping forces, in phase with the velocity of the system, are governing around the natural frequency of the system
3. Spring forces, in phase with the displacement of the system, are governing in shorter waves, with high wave frequencies.

To determine the range of these governing forces, the RAO's for surge and sway have been determined for 5 different damping values over 17 different frequencies. This is done with using a regular wave train that is computed in aNySIM, see appendix D.5 for the applied method. The used damping coefficients are indicated relative to the damping that is defined in chapter 4.

Results are shown in figure 3.7. The natural frequency of the system ( $\omega_n$ ) in both directions is designated with the red arrow. As becomes clear, the damping not only has a significant influence at that frequency, but in a wider range (this can be observed by the difference in RAO for different damping values). The range which has been defined as the damping dominated range is shown between the grey bars. Within the grey bars, an increase or decrease by 50% in damping accounts for 10% in RAO: The damping is still influential, but other forces become more dominant. Outside of the grey bars, inertia or spring forces are dominating. A note must be made that this division is based on a subjective judgement and therefore the grey bars can not be seen as hard lines, but more as transition phases.

In figure 3.8, the regular and irregular wave tests are allocated in a force group according to their wave (peak) period.

As can be seen, most regular and irregular tests are located in the damping dominating region. However, irregular waves in higher sea states (longer wave periods and higher wave heights, test I-13, I-14) are located in the transition area between the spring terms and damping terms.



(a) Surge RAO for different damping values. The natural frequency of the system in surge is depicted with the red arrow.

(b) Sway RAO for different damping values. The natural frequency of the system in surge is depicted with the red arrow.

Figure 3.7: Motion RAO for different frequencies and different damping values, obtained with a aNySIM defined regular wave train. The grey bars indicate the transition between the three ranges of governing forces (spring, damping or mass dominated).

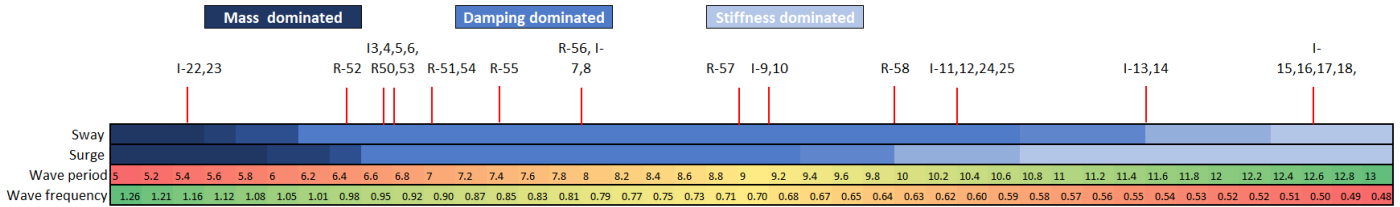


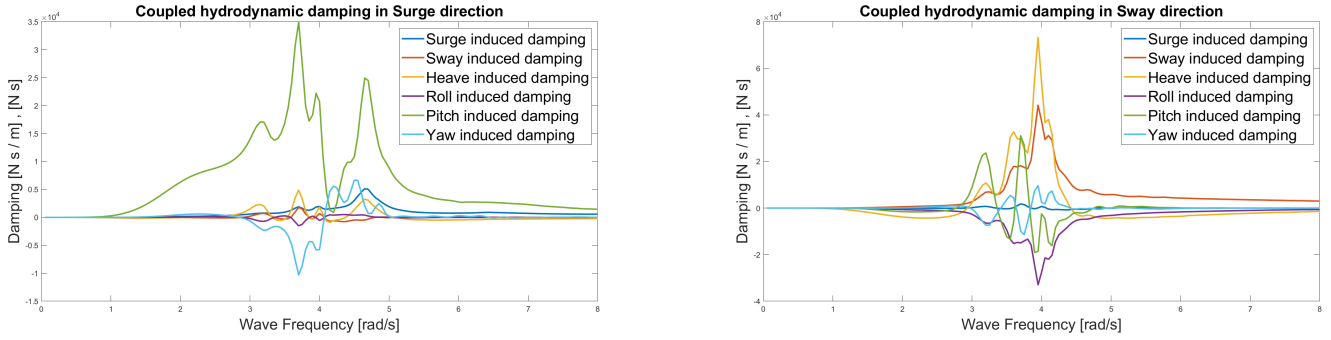
Figure 3.8: The regular and irregular wave tests that have been executed in the offshore basin are classified according to their (peak) period in the area of stiffness, damping or mass dominated motions.

### Relative significance of viscous damping

As shown in the previous section about governing forces, most tests are in the damping region. Damping, as explained in chapter 3.3, is a combination of hydrodynamic (wave making) damping and viscous damping effects. To show the governing damping effect for a degree of freedom, the hydrodynamic damping in has been extracted from the hyd file for all 12 floaters. Appendix G.1 shows the results of this hydrodynamic damping together with the viscous damping that is determined in chapter 4. The overall result is that for surge, sway and yaw the viscous damping is dominating and for heave, roll and pitch the hydrodynamic damping is dominating. Differences between simulation and basin test results for these hydrodynamic dominated motions are therefore likely not caused by viscous damping.

### Hydrodynamic coupling between degrees of freedom

The system experiences coupling between the degrees of freedom for the hydrodynamic coefficients, which is explained in section 3.3.2. The significance of these coupling effects for the hydrodynamic damping is obtained from the hydrodynamic data base and shown surge and sway in figure 3.9. Although no data is available, similar reasoning can be applied to the expected coupling in viscous damping effects. Both figures show that most damping effects become visible between the range of 3 and 5 rad/s. However, for the wave exciting frequencies in this research, the range between 0.6 and 1.2 rad/s is most important (see appendix A.1). For this range, the coupled damping effects are low, which can be observed by the low damping coefficients. One exception is present; a strong coupling can be observed between the pitch motion and surge damping as shown in figure 3.9a. This coupling becomes visible from a frequency of 1rad/s and becomes stronger towards the higher frequencies. On the other hand, figure 3.9b does not give similar results for the coupled roll damping, which is negligible for frequencies up to 3rad/s. This difference between the coupled pitch and roll damping can be explained by the dimensions of the floater in x and y directions. A larger dimension in x-direction corresponds to a larger coupled pitch damping. A smaller dimension in y-direction corresponds to a lower coupled roll damping.



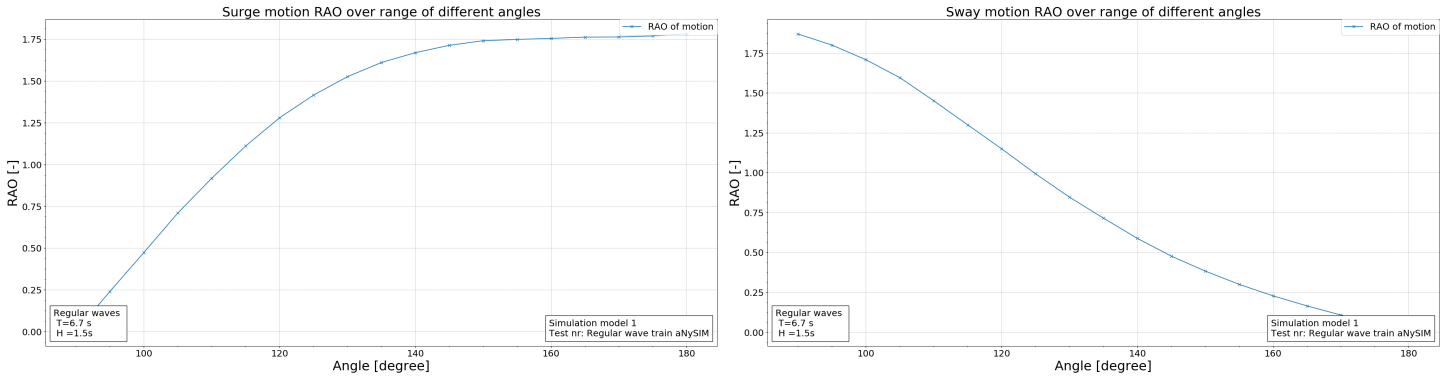
(a) Hydrodynamic damping in surge direction due to motion in all DOF. For the wave exciting frequency range (0.5-1.2rad/s), only a small influence of the pitch induced damping can be observed.

(b) Hydrodynamic damping in sway direction due to motion in all DOF. For the wave exciting frequency range (0.5-1.2rad/s), no influence of hydrodynamic damping can be observed.

Figure 3.9: The coupled hydrodynamic damping in surge and sway direction due to motions in all DOF, obtained from the hyd file.

### Influence of wave angle

The influence of different wave angles was studied ( $\mu$ ) in the simulation model, by performing simulations from  $\mu = 180^\circ$  to  $\mu = 90^\circ$ . The influence of this incoming wave angle on the surge and sway motion RAO is shown in figure 3.10. Waves with wave period  $T = 6.7s$  and wave height  $H = 1.5m$  are used. As can be seen in 3.10a, the RAO in surge remains relatively constant for incoming wave angles from  $\mu = 180^\circ$  to  $\mu = 150^\circ$ , whereafter a steep decline in RAO can be observed. This means that for small differences in the head waves, no clear differences are likely to be observed in the surge motion RAO. The sway RAO, as observed in figure 3.10b, has a more constant change in RAO over the entire range of incoming wave angles, resulting in more effect around the beam wave range (compared to the surge RAO in head waves) and a smaller effect in the head wave range (compared to the surge RAO in beam waves). The effect of a different wave angle therefore has different effects on the surge and sway motion of the system. Both trends can be used for the analysis of the different wave angle tests.



(a) Surge RAO for different wave angles. The maximum RAO occurs for head waves  $\mu = 180^\circ$ .

(b) Sway RAO for different wave angles. The maximum RAO occurs for beam waves  $\mu = 90^\circ$ .

Figure 3.10: Motion RAO in surge and sway for a range of incoming wave angles to visualise the effect of a different incoming wave.

### 3.6. Conclusion

In this chapter the model structure and numerical implementation are presented for the simulation model. The implementation of the mathematical model in the numerical model has been verified for aNySIM, and the results from DIFFRAC have been analysed in appendix B to address possible numerical uncertainties. However, since the calculations in DIFFRAC are done externally (at MARIN), numerical uncertainties cannot be fully excluded.

Inherent to the choice of a frequency-time domain approach, several simplifications and assumptions are incorporated in the simulation model regarding the physical problem presented in chapter 2. The most

important conclusions of these simplifications are:

- The simulation model is equipped with a viscous damping force that is dependent (linear or quadratic) on the flow velocity. The damping coefficients are similar for all tests characteristics. This introduces several simplifications:
  - A different ratio between linear and quadratic damping effects (and between skin friction and form drag) is present due to different viscous effects (vortices/water trough gaps). This difference is present between decay, regular and irregular wave tests, but can also occur for different wave heights or period.
  - Different viscous effects on the floaters due to shielding are levelled out in the damping determination method. A change in shielding effects is not incorporated.
  - Similarly, different viscous effects on the mooring lines or joints are levelled out. A change in these effects for different tests is not incorporated.
- Viscous effects in roll, pitch and heave not included in the simulation model. This is assumed to be a valid simplification since viscous forces are negligible as compared to hydrodynamic (wave making) damping effects in these three directions, contrary to studies on more common offshore simulations[3].
- The contribution of viscous forces to the behaviour of the system is significant in surge and sway, where the systems natural period is close to the regular and irregular sea states tested. The decay tests are expected to introduce parameter uncertainty due to the highly damped behaviour, which is therefore expected to influence the system behaviour significantly.
- Overflowing water effects are not incorporated in the simulation model. Nonlinear effects related to this phenomenon are not incorporated and include wave breaking, volume flux effects and nonlinear effects on the computation on the excitation force. The significance of these effects have not yet been studied for a multi-body, moored floating system.

Following from these conclusions, the viscous damping implementation is expected to introduce several uncertainties that significantly influence the simulation model accuracy. Therefore, the next chapter discusses the viscous damping implementation and the model accuracy.

# 4

## Damping implementation and model accuracy

In this chapter, the viscous damping implementation and the model accuracy are presented. The goal of this chapter is to provide insight into the usability of the conventional damping method, for which the parameter uncertainty is discussed, and to present and analyse the model accuracy. This goal is related to research question 3 as presented in chapter 1.

This first section elaborates on the validation of the static behaviour of the system, which is required for further analysis of the dynamic behaviour. Thereafter the damping determination method and the associated possible parameter uncertainty are presented and discussed. Finally, the model accuracy is analysed.

### 4.1. Static equilibrium

The static equilibrium of the system is independent on dynamic effects from the viscous damping implementation and can therefore be validated prior to the damping determination.

#### 4.1.1. Method

The static equilibrium was determined based on pretension in the mooring line forces, pretension in the joints, the locations and orientations of the floaters and static offset of the system. The first three components were determined using a zero procedure, the latter was determined with a static offset test.

##### Zero procedure

In the zero procedure, the simulation model runs for 200 seconds with no external forces applied on the floaters. Within this time the model reaches static equilibrium (see figure 4.1, where static equilibrium is reached after 120 seconds), after which the mean tension in the mooring lines and joints is obtained. The locations and orientations of the floaters have been derived from this static equilibrium as well.

##### Static offset test

In addition to the static equilibrium, the system is subjected to a static offset test, to obtain the mooring line forces for a static offset in x or y direction. To do so, an external force is applied to the model in x or y direction. From this offset the mooring line characteristics such as the stiffness can be validated. Details of the applied simulation method can be observed in appendix D.2. The static offset test is validated with a similar test performed in the experiments.

#### 4.1.2. Results

In this section results are presented to validate the static behaviour of the mooring system, joints and floaters. Corresponding basin tests serve as validation.

##### Pretension in mooring lines

Figure 4.1 shows a time trace of the tension in all 4 mooring lines during the zero procedure. As can be seen, all 4 lines have converged to the same value, meaning the system has reached static equilibrium. The pretension is 226.6kN. This is within 1% error of the zero measurements of the basin tests, where the average is 225.63

kN. The first 40 seconds of the time trace show a heavy oscillating mooring force in which the simulation is not numerically stable. This can be attributed to the Broyden error as explained in section 3.4.3.

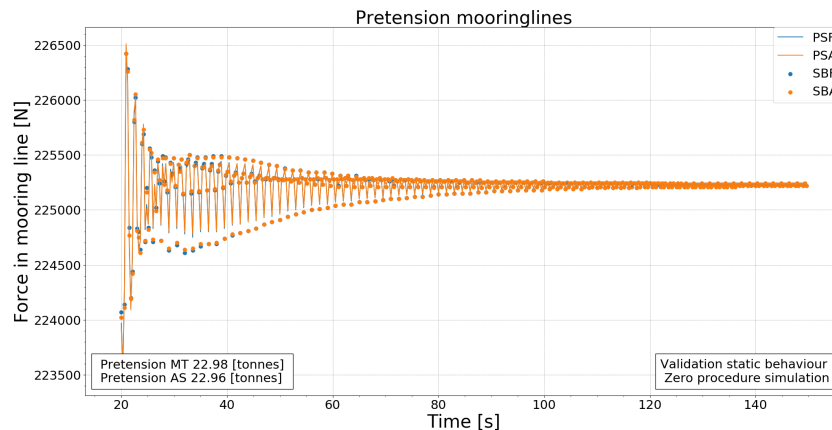


Figure 4.1: Results of the pretension in all 4 mooring lines measured with a zero procedure. The pretension is equal to the pretension measured in the offshore basin tests. The static equilibrium is reached after 120 seconds.

### Pretension in joints

In addition to the pretension in the mooring lines, the joints between the floaters are subjected to pretension as well. Results for this pretension is shown in figure 4.2 for the joints between the 8 floaters that were equipped with motion measurement sensors in the basin tests. This means that not all joint forces are known for the basin tests. The mean value is shown for the force in the global x and y direction. Note that for joints 'fore' and 'aft', the force in y direction is the axial force in the joint and that for joints 'PS' and 'SB', the force in x direction is the axial force. These forces are dominant in the joint for both the basin tests and the aNySIM simulation.

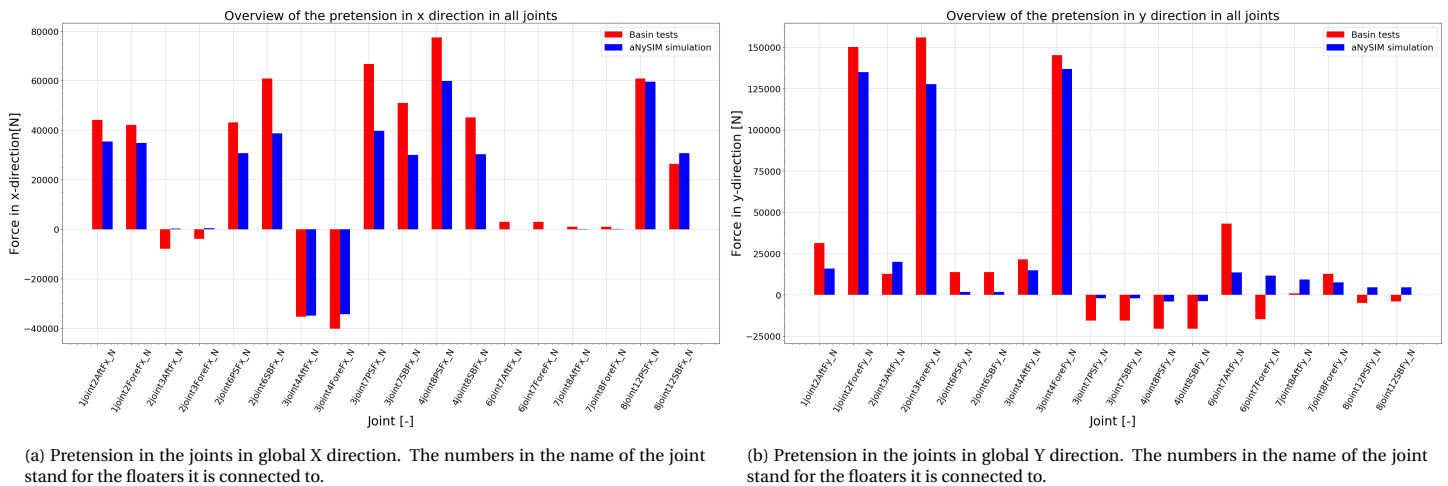
As can be seen, the agreement in pretension is relatively good, the same trend over all joints can be observed. However, the aNySIM simulation is underestimating the pretension in almost all joints. This implies that the system is spread out further in the basin tests, with more distance between the floaters due to the mooring line pretension. For the joints with the axial stiffness in global x-direction (figure 4.2a), and in global y-direction (figure 4.2b) the underestimation is around 20000N. This corresponds to a relative distance of 0.009 m. On model scale this is 0.00045m, less than 0.5mm. It is likely that this difference is not a result of signal inaccuracy but due to informational uncertainty of the actual stiffness of the joints (see section 2.3): the actual stiffness in the model tests could be slightly lower than what has been provided by MARIN. This results in a different force equilibrium.

The difference in the joint pretension is accepted for the simulation model, since it has been explained in section 2.3 that the joints will not be analysed extensively and possible inaccuracies in the simulation model or basin test results do not influence the overall behaviour of the system much due to the high stiffness of the joints (therefore, the system behaves as one system, as discussed in section 2.2.2).

### Orientation and location of floaters

In addition to the pretension in the mooring lines and joints, the orientation and locations of the floaters were compared to analyse the agreement in static equilibrium. Table 4.1 shows the difference between the basin tests and simulation results. As can be seen, there is a constant offset of around 0.1m for all floaters in x-direction, meaning that in the simulation model the system is positioned 0.1m more in positive x-direction. This is less than 1% offset in comparison to the length of the entire system.

For the locations in y direction, it can be observed that the floaters in aNySIM are closer together and closer to the GCS (all floaters that are located on the positive y-axis have a negative displacement compared to the basin test result). The difference becomes larger for the outer floaters (floater 1, 8 and 12). The largest offset is present for floater 1, where the floater in the simulation model is positioned 0.1m closer to the GCS origin. This is 1% offset in comparison to the width of the entire system. For the yaw orientation of the floaters, the floaters at the aft side of the system (floater 8 and 12), show a smaller spreading of the system in



(a) Pretension in the joints in global X direction. The numbers in the name of the joint stand for the floaters it is connected to.

(b) Pretension in the joints in global Y direction. The numbers in the name of the joint stand for the floaters it is connected to.

Figure 4.2: Mean pretension in the joints between the floaters for the basin tests and aNySIM simulation. Pretension is given in the global coordinate system.

the simulation model. This means that the simulation model system is oriented more symmetrically than the basin test system. This is a logical result from the difference in joint pretension as discussed in section 4.1.2.

Table 4.1: The difference between the basin tests and simulation static equilibrium in full scale, Locations in x and y direction and yaw rotation are given for all 8 floaters equipped with motion sensors.

Floater	x offset [m]	y offset [m]	yaw offset [degree]
1	0.1011	-0.1085	-0.5700
2	0.0928	-0.0517	-0.1343
3	0.0724	-0.0316	-0.3131
4	0.1022	0.0307	0.0473
6	0.0913	-0.0204	0.2121
7	0.1065	0.0366	-0.1976
8	0.1258	0.0746	1.0295
12	0.1392	0.0734	-2.6709

### Static offset

Figure 4.3a shows the forces in all mooring lines for the static offset in x-direction, together with the measured force from the basin tests. As can be seen, the current model simulates the forces in the mooring lines correctly until an offset of 10 meters. After that, the stiffness gradient of the force increases in the basin tests due to the maximum length of spring B, which has not been implemented in the simulation model (see section 3.4.3 on the mooring line implementation). Furthermore, the mooring lines on front and aft show mirrored behaviour, implying that all mooring lines behave in the same way.

Similar results are present for static offset test in y direction (figure 4.3b), where the mooring lines on starboard show the mirrored behaviour of the lines on port side.

Finally, the system is symmetric in the GCS origin, since the intersection of the mooring lines is at offset = 0 for both x as y direction.

### 4.1.3. Concluding remarks

The static equilibrium of the simulation model is validated as the error in pretension in the mooring lines is within 1%, and the floater locations are determined with offsets around 1% in comparison to size of the system. However, for offsets larger than 10m, the mooring system becomes invalid due to a different implementation of the springs in the mooring line simulation.

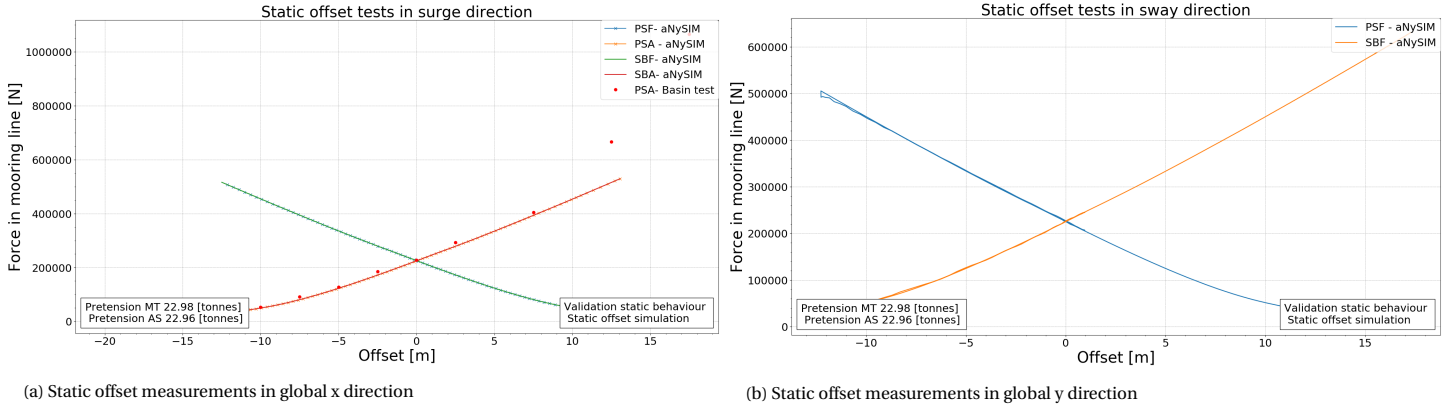


Figure 4.3: The mooring line forces of the aNySIM simulations for static offsets in global x and y direction. The static offset in x direction is compared with the basin test results.

## 4.2. Damping determination "decay-fit"

The conventional method to determine the viscous damping of a system is by analysing decay tests, applied by several previous done studies [3, 27, 39]. This method will be referred to as the 'decay-fit' method. The usability of this method is unknown for a multi-body system as presented in this study due to several reasons as discussed in chapter 2 and 3:

- No literature was found on decay tests for more than 2 interconnected bodies, hence there is a knowledge gap on the simulation accuracy for decay motions.
- The decay test results show that the system is highly damped, increasing the chance on parameter uncertainty.
- The natural frequency of the system in surge and sway is within the sea state range that is analysed, contrary to the previous done studies [3, 27, 39], where the natural period of the system is much larger than the sea state range. Damping effects are of significance importance in these tests.
- As concluded in section 2.4, different viscous effects are present for different tests (decay/regular/irregular wave tests). The mathematical implementation simplifies this phenomenon by selecting a fixed linear and quadratic damping term (see section 3.6).

The following section discusses the method and results obtained for the 'decay-fit' damping implementation.

### 4.2.1. Method

To obtain the 'decay-fit' damping, the decay tests done at MARIN are compared with the decay simulations that were performed in aNySIM. The decay simulations were performed by giving all floaters an offset and then releasing them to obtain a decaying motion. The first step is to stabilise the simulation model such that its static equilibrium is reached. Secondly, a force is applied to all floaters to give the system an offset. aNySIM does not offer the possibility to give the floaters a fixed location after static equilibrium was reached and therefore this was done by applying an external force. The required external force has to result in an initial displacement that is in agreement with the initial displacement the model has in the basin tests. This force was determined by trial and error. More detail on the decay simulation can be seen in D.3.

The decay basin tests were repeated 3 times for each direction, resulting in 3 different time traces that can be used. These time traces clearly show that the system is highly damped, resulting in few oscillations. Figure 4.4 shows the selected time traces for floater 7 that will be used for damping value determination. Two methods were applied to do so.

### P-Q analysis

A common method is to use a P-Q analysis [44], in which the linear and quadratic damping coefficients can be determined with a polynomial fit. This analysis sets out the successive crests and troughs as a function of the amplitude to determine a polynomial fit. P and Q values for all 3 decay tests were delivered in the MARIN report [31], where more details on this method can be found as well. These values can be converted to a linear damping coefficient with:

$$B^{(1)} = \frac{2PM_{kk\text{tot}}}{T_d} - b_{kk} \quad (4.1)$$

Table 4.2: Threshold value for decaying motion in model scale (MS) and full scale (FS) and the number of oscillation that will be taken into account.

Decay direction	Threshold value MS	Threshold value FS	Time[s]	# oscillations [-]
Surge	0.0085[m]	0.17 [m]	68	2
Sway	0.0098[m]	0.195[m]	262	1
Yaw	0.16 [degree]	0.16 [degree]	835	1

Where  $M_{tot}$  is the sum of the total mass of the system and the added mass in the direction of decay.  $T_d$  is the damped period and  $b_{kk}$  is the hydrodynamic damping in the direction of decay(k). Here the assumption is made that the hydrodynamic damping is linear only. The quadratic damping can be determined with:

$$B^{(2)} = \frac{2QM_{kk_{tot}}}{8} \quad (4.2)$$

Note that for the damping in yaw direction this quadratic term has to be multiplied by  $\frac{180}{\pi}$  to convert to the correct units. This method works best for low damped systems, where multiple successive damping oscillations can be evaluated. Therefore it was expected that the determination of P and Q would not give damping values accurate enough for this system, since the system is heavily damped.

### Motion fitting

In the second method, the motion of the simulation model was fitted on the basin test results by adjusting the linear and quadratic damping directly. The quadratic damping following from this method is then converted to polar coefficients to implement in aNySIM. To identify the relevant oscillations for decay analysis, a threshold value was identified, below which the decay amplitude becomes very small and therefore no decaying relation can be observed. Table 4.2 shows these amplitudes in both model scale (MS) and full scale (FS), and the corresponding time from where the amplitudes are below the threshold value in the time trace in figure 4.4 for all directions. As a conclusion, the number of oscillations that were taken into account for each decay motion was determined. The damping values are correctly fitted to the motion if the behaviour of the simulation complies to 2 criteria:

- Damped period of simulation is in agreement with damped period of basin tests for applicable oscillations.
- Applicable oscillations show similar behaviour; the linear and quadratic share of the damping values is correctly determined.

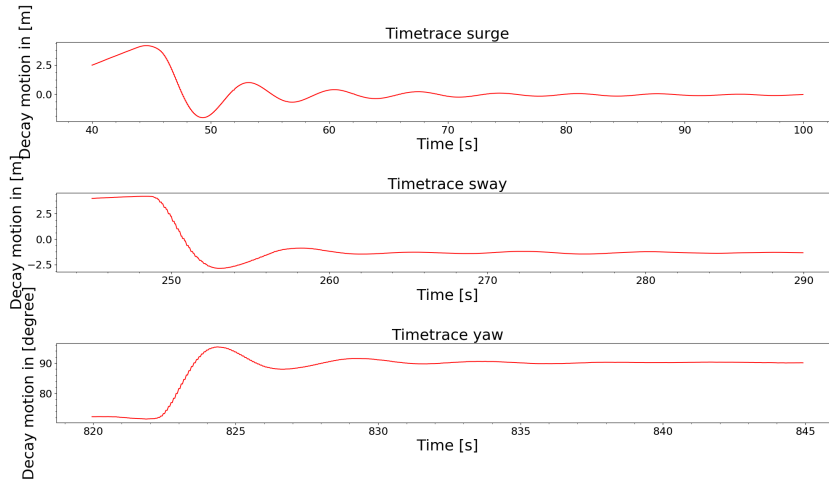


Figure 4.4: Selected decay time traces of basin tests in surge, sway and yaw direction.

To calculate the natural frequency, the logarithmic decrement is used:

$$T_n = T_d \sqrt{1 - \zeta^2} \quad (4.3)$$

with:

$$\zeta = \frac{1}{\sqrt{1 + \left(\frac{2\pi}{\delta}\right)^2}} \quad (4.4)$$

$$\delta = \frac{1}{n} \ln \frac{x(t)}{x(t + nT_d)} \quad (4.5)$$

Where  $\zeta$  is the damping ratio of the system,  $\delta$  is the logarithmic decrement,  $n$  is the number of peaks and  $x$  is the amplitude of a peak. The damped period  $T_d$  is measured using the mean crossings method [31].

#### 4.2.2. Results "decay-fit" damping determination

The results from the decay tests and the behaviour in regular waves using the "decay-fit" damping are analysed in this section. The damping values obtained from the 'decay-fit' method are presented in table 4.3, together with the initial damping values obtained from the P-Q analysis. As can be observed, there is a large difference between the values of the two methods. Another comment must be made on the fact that the sway and yaw results do not contain a quadratic contribution for the 'decay-fit' method. This is a result of the direct fitting method, where the highest agreement was obtained using linear damping only. The results will be discussed in more detail for each DOF separately.

Table 4.3: Damping coefficient values for 1 floater in comparison to the total hydrodynamic damping

Damping coeff	P-Q method	'Decay-fit'
$b_{surge}^{(1)} [kNm/s]$	1.73E+03	1.56E+03
$b_{sway}^{(1)} [kNm/s]$	6.25E+03	5.61E+03
$b_{yaw}^{(1)} [kNm/s]$	3.78E+03	6.10E+05
$b_{surge}^{(2)} [kNm^2s^{-2}]$	1.11E+03	6.31E+02
$b_{sway}^{(2)} [kNm^2s^{-2}]$	7.54E+02	-
$b_{yaw}^{(2)} [kNm^2s^{-2}]$	1.15E+04	-

Table 4.4: (Damped) natural period for the decay tests in surge, sway and yaw direction.

Natural frequency		Surge	Sway	Yaw
Basin test	$T_d$	7.33	8.1	4.47
	$T_n$	7.31	8.06	4.40
aNySIM	$T_d$	7.55	8.05	5.04
	$T_n$	7.5	8.0	4.98

#### Decay behaviour in surge

Since the system is highly damped, it is difficult to obtain the natural frequency of the system. Therefore, low damping values were implemented in aNySIM to obtain more oscillations and get better insight in the decaying behaviour. Figure 4.5a shows the decaying motion as a result. As can be seen, the simulation model has a constant damped natural period, that is in agreement with the damped natural period of the first two oscillations of the basin tests. The damped natural period for the basin tests is 7.3 seconds, whereas the simulation model has an average of 7.5 seconds over all periods, as shown in table 4.4.

Results of the final damping are shown in figure 4.5b. The first 2 oscillations of the simulation are in good agreement with the basin tests. What stands out is that, after two oscillations, the simulation model damps out more quickly than the model tests. This effect could be a result of small noise (e.g. remaining small waves) in the basin test, however no visual data is available to check this hypothesis. Furthermore, the simulation model shows asymmetric behaviour in the later oscillations, where the motion from trough to crest takes longer than the motion from crest to trough. This behaviour is not seen in the low damped system of figure 4.5a. This asymmetry becomes obvious for amplitudes lower than 0.1 metre on full scale and is of very small significance on the total behaviour of the system (less than 1% in comparison to the length of the entire system) and was therefore neglected in further analysis.

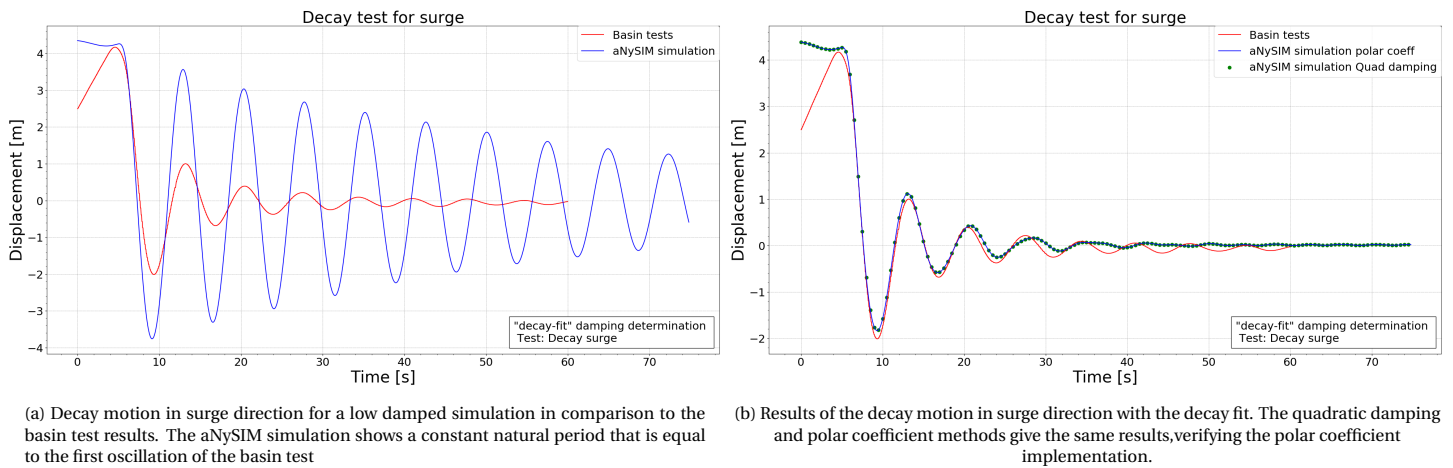


Figure 4.5: Results for the surge decay test using the 'decay-fit' damping implementation

Furthermore, the polar coefficients were verified. figure 4.5b shows the results for the quadratic damping method as the polar coefficient method. The former is calculated using the absolute floater velocity and the latter is calculated using the relative flow velocity, see section 3.4.3. The two methods are in exact agreement, which is expected since there is no flow velocity in the decay test and thus the relative velocity is equal to the absolute velocity of the floater. The polar coefficient implementation is done correctly.

### Decay behaviour in sway

Similar to surge, a low damped system is used to obtain the natural frequency, which can be seen in figure 4.6b. The system has a constant damped natural period of 8.1 seconds, which is comparable to the first oscillation of the basin tests, shown in table 4.4.

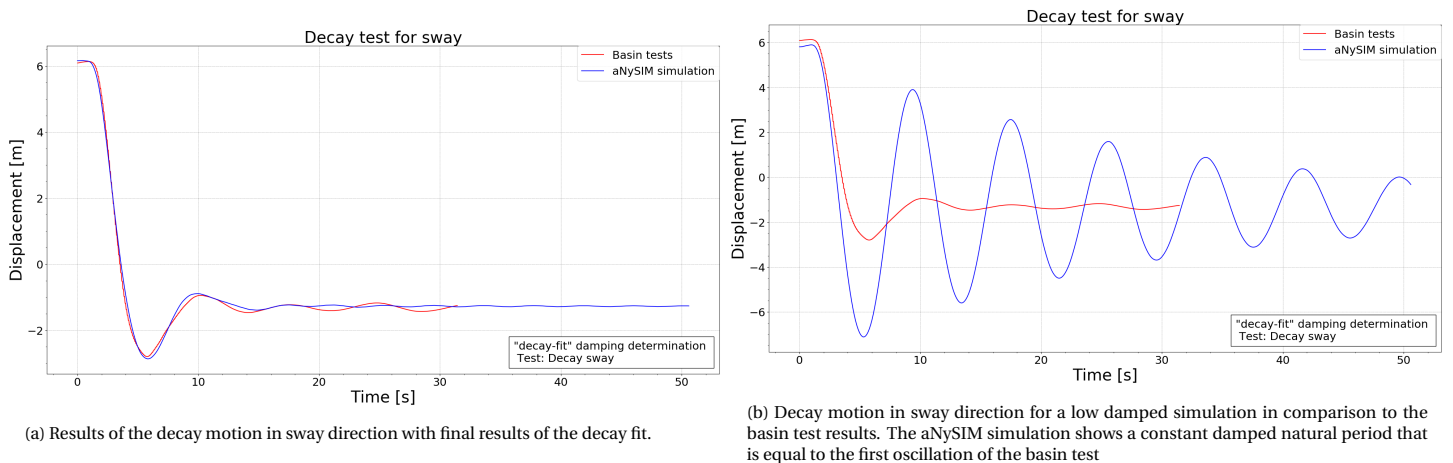


Figure 4.6: Results for the surge decay test using the 'decay-fit' damping implementation and a low damped implementation

Results of the final damping are shown in figure 4.6a. For the final result, only linear damping is implemented (see table 4.3), in contrast to the values obtained from the P-Q analysis. This is done because results using quadratic damping showed less agreement.

The first oscillation is in relative good agreement with the basin test. The decaying motion stops after 1 oscillation, after which the simulation model shows very small displacements. The damping in the basin tests results in larger motions for further oscillations, which could be a result of small noise (e.g. remaining small waves) in the basin test, similar to the surge decay.

### Decay behaviour in yaw

The system behaviour in yaw decay is shown in figure 4.7. The simulation model result shows notable behaviour for the first oscillation, in which no clear sine wave can be observed, indicating a nonlinear motion due to a summation of multiple oscillations. This nonlinear behaviour is not expected. As a result, the damped natural period for the simulation model differs from the model tests significantly, as can be seen in table 4.4.

As can be observed in table 4.3, the 'decay-fit' method does not contain quadratic damping. This was done since adding the quadratic damping resulted in a motion that showed more nonlinear behaviour in the first oscillation.

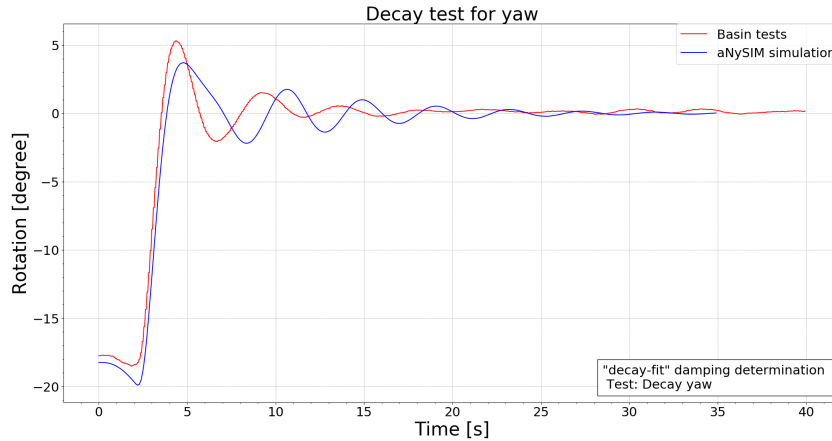
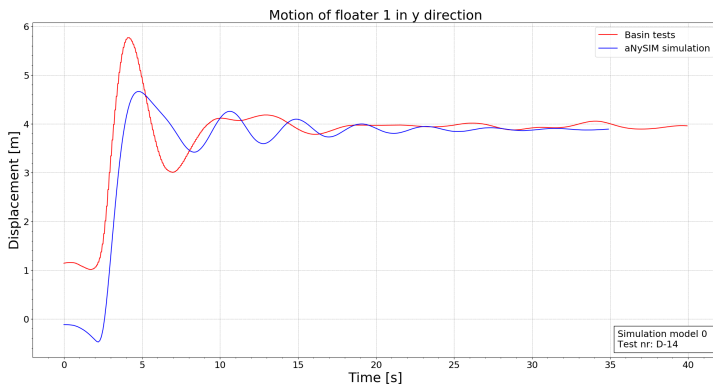
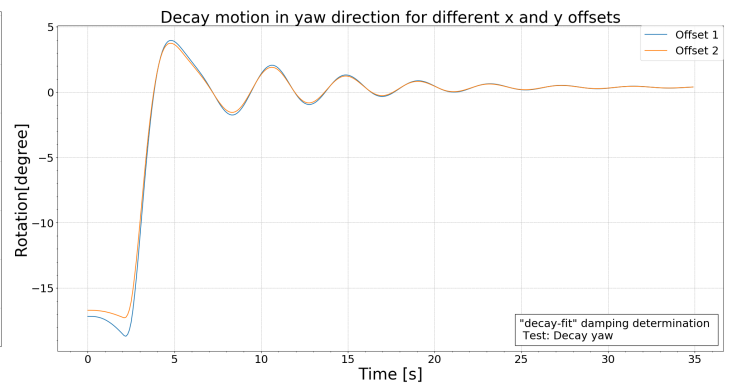


Figure 4.7: Results of the decay motion in yaw direction with the decay fit. The simulation model results show different behaviour for the first oscillation.



(a) Sway motion of floater 1 for the decay test in yaw direction. Comparison between the basin test and the aNySIM simulation shows that the simulation has a different initial location.



(b) Comparison of yaw decay results for different initial offsets. The nonlinear behaviour of the first oscillation does not change significantly.

Figure 4.8: Comparison of different offset locations in x and y for floater 1

To study the cause of this inaccuracy in the simulation model behaviour, the x and y positions of floater 1 are also evaluated in figure 4.8. Floater 1 is used instead of floater 7 because it has higher displacements for the same yaw angle. The positions are compared for the basin test and aNySIM model in figure 4.8a. What can be seen is that the initial displacement for floater 1 in the aNySIM simulation is lower in x direction. This implies that, although the initial yaw angle for both tests is equal, the system is not setup in a similar way, resulting in different displacements. To see whether this different setup is influential, two decay simulations of floater 1 are shown for 2 different initial offsets of the floaters in figure 4.8b. As can be seen, offset 1 and 2 have a different yaw angle in the initial stage but still show the same behaviour. The initial offset does not influence the yaw behaviour in a significant manner.

Furthermore, the relative motion of the floaters is studied in yaw decay motion. Figure 4.9 presents the yaw decay for 5 different floaters. As can be seen, the motion is similar for all floaters in both the aNySIM simulation (figure 4.9a) as in the basin test (figure 4.9b), and therefore it can be concluded that there is no

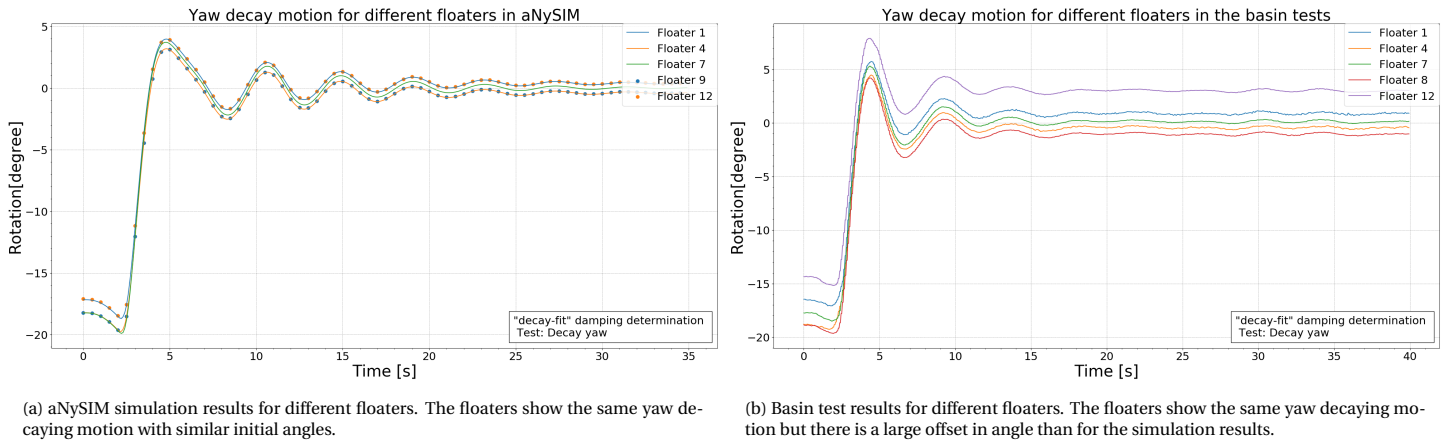


Figure 4.9: Comparison of the decaying motion in the yaw decay test for different floaters.

relative motion between the floaters causing the nonlinear behaviour in the aNySIM simulation. Both figures show a small difference in mean for all floaters due to the spreading of the system in pretension. Following logically from the higher pretension in the basin tests (figure 4.2), the difference in mean between the floaters is larger in the basin tests.

The final result in figure 4.7 does not show the desired agreement for the model aNySIM tests, however, it is decided to continue with this result, given the following reason: There is an uncertainty in the decaying motion of both the simulation as the basin test as a result from the approach that is used to obtain the initial angle. To get the exact similar initial position for the aNySIM test is not reasonable using a trial and error method, therefore, more research is required to develop a suitable yaw decay method for the simulation model. Additionally, no video data is available of the yaw decay tests, so it is unknown what the exact circumstances were in the basin test.

### Behaviour in regular waves

The results of regular wave test R-50, where the surge motion is the governing due to head waves, was evaluated to see the effect of the 'decay-fit' method in regular waves. The time trace of the surge motion of floater 1 for the first 300 seconds can be seen in figure 4.10, in which waves are in their start-up phase. The results for the basin tests and simulations show a similar period, equal to the excited wave period. Additionally, the motion in the simulation model is built up in a similar manner as for the basin tests up to 100s. Thereafter, the amplitude is lower for the simulation. Furthermore, a small offset in the mean location of the floater can be observed, which can be related to the orientation offset as discussed in section 4.1.2.

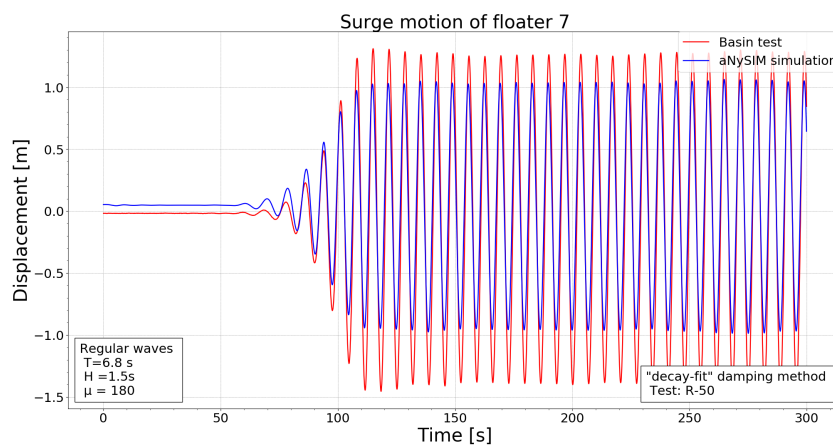


Figure 4.10: Time trace of the surge motion of floater 7 in regular wave R-50 for the basin test and the aNySIM simulation. The aNySIM simulation underestimates the motion amplitude. A small difference in initial location can be observed

The trend of a lower amplitude that is observed for test R-50 with head waves, can also be observed for the

other regular wave tests. To analyse this trend, the RAO (response amplitude operator) was calculated for the surge and sway motions of all regular wave tests ( see figure 4.11). Here the RAO's are normalised, showing the RAO of the simulation relative to the RAO of the basin tests. Some observations can be made:

- The RAO of the surge motion in head waves (R-50, R-51, R-52) for the simulation model is around 65 to 75 percent of the basin test results (see figure 4.11a). The agreement for test R-51 is lowest. This test has a wave period of 7.05 seconds, which is closer to the actual natural period of the system than R-50 and R-52. The effect thus implies that towards the natural period of the system, the agreement in motion becomes less.
- The RAO for sway motion in beam waves (R-53, R-54, R-55) can be observed in figure 4.11b and is less than 60% for all 3 tests. The effect of the natural frequency is less visible in sway direction. This can be explained since the natural frequency in sway is 8.1 seconds and the highest tested wave period is 7.3 seconds for R-55. This difference is larger than for the surge motion, and thus the natural frequency effect is less visible.
- Looking at the RAO in the motion perpendicular to the wave direction, the agreement for both surge (figure 4.11a, R-53, R-54, R-55) as for sway (figure 4.11b, R-50, R-51, R-52) is very low. An explanation for this phenomenon is that the system in aNySIM is oriented more symmetrically than in the basin tests, which is typically the case for numerical simulations. This means that head waves induce little to no response in sway and the other way around. However, the absolute RAO in this perpendicular direction for the basin test results are around 10% of the RAO's parallel to the wave direction and thus the overall impact of this effect is small as well.
- The RAO's for the final tests (R-56, R-57, R-58) of the simulation model show the same trend for surge and sway, where the RAO increases towards R-58. This results in an overestimation in surge RAO for test R-57 and R-58 (Wave periods 9 and 10 seconds), for the surge RAO. The RAO for sway remains much lower for the simulation results.

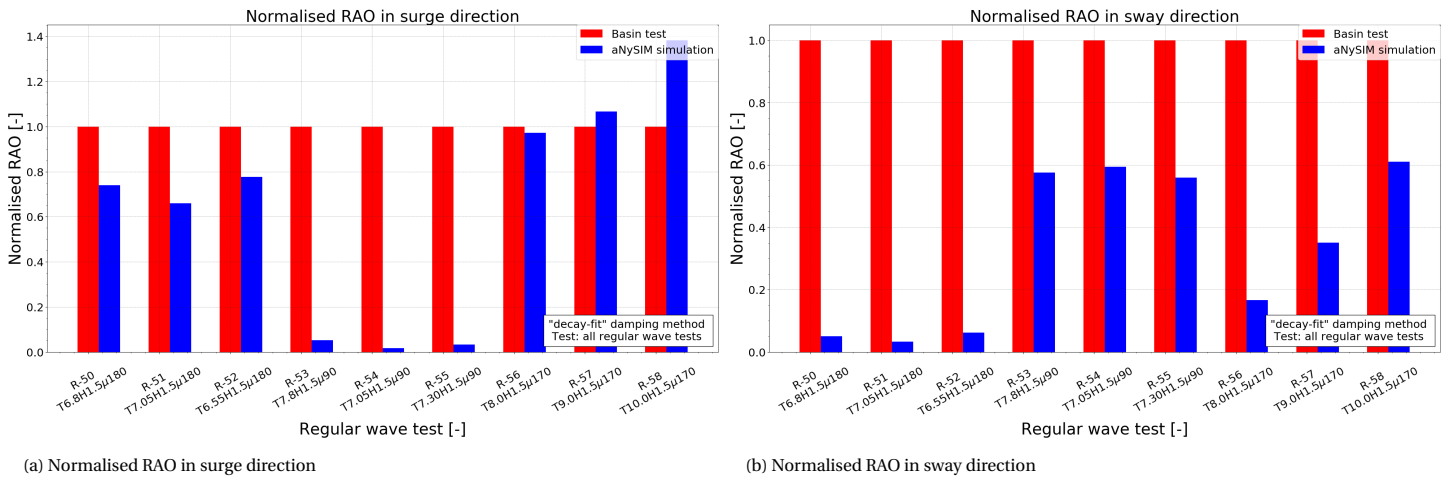


Figure 4.11: Normalised RAO's for all regular wave tests in surge and sway direction, where the RAO of the basin test is set to 1. The RAO's are shown for floater 1

### 4.2.3. Concluding remarks

The usability of the 'decay-fit' method to determine the viscous damping of the system was studied in this section. Several conclusions can be drawn:

- The decay motion in surge and sway can be accurately simulated for a multi-body system. However, the oscillation accuracy for the yaw decay motion is low and more research is required to obtain a suitable simulation method for the yaw decay tests of a multi-body system.
- For regular waves, the 'decay-fit' method is over damped and the decrease in agreement for the regular wave tests closest to the natural frequency of the system indicates that the damping is indeed not accurately determined.

- The 'decay-fit' was applied on the first oscillation of the used tests, which has resulted in little comparison data for the damping coefficients, creating significant parameter uncertainty, contributing to the over damped system in regular waves.
- Small errors in the damping determination are of large influence since the regular wave tests that were studied are close to the natural frequency.
- A physical cause could be present in which the decay tests are too strongly damped compared to the damping that is present in the regular wave tests. However, this is in contradiction with the expectations regarding damping effects in the different tests, since it is expected that more viscous damping effects are present in the regular wave tests. Unfortunately, no video footage is available to further study the decay tests.

It can be concluded that the decay-fit method introduces parameter uncertainty that causes inaccurate results for the regular wave tests. Due to the natural period of the system in the regular wave range, this parameter uncertainty has a large effect. Secondly, a gap of knowledge is present on the physical conditions of the decay tests that might cause the high damping. Therefore, it was decided to use a different damping determination method to get more insight in the parameter uncertainty of the decay tests and to analyse whether higher accuracy can be obtained using a different method.

### 4.3. Damping determination 'regular wave-fit'

A different method to obtain viscous damping is studied by Malta [20], where the Random Decrement Technique [10] is presented for offshore structures. This method uses irregular wave test to determine damping coefficients, assuming a linear response of the floating units. Due to the hydrodynamic coupling and physical origin of viscous effects, the response of this system is not linear, and therefore this method was not adopted for this study.

Another method to obtain the viscous damping is briefly mentioned by Bokhorst [2], where viscous damping values are calibrated using different model tests with different wave heights. Unfortunately, the approach is not explained extensively, but it was decided to build on this idea, using regular wave tests to calibrate the damping values. Therefore, the 'regular wave-fit' method was introduced. Several comments must be made regarding the proposed method:

- Viscous damping effects in regular waves are expected to be more similar to the viscous damping effects in irregular waves as compared to decay tests (see section 2.4), due to the presence of waves.
- Using regular waves decreases the parameter uncertainty in the damping determination since the motions can be fitted more accurately and more data is available.
- A downside is that regular wave tests are not performed at the natural frequency of the system in surge and sway. This means that not all viscous damping effects are captured by this method, and damping at one specific frequency is implemented.
- The damping implementation remains equal to the 'decay-fit' method, ie. The mathematical set up does not change, only the determination of the damping coefficients is altered.
- No previous done research has been found on the application of this method that can be used as a benchmark study.

Following from these comments, three differences in the 'regular wave-fit' method as compared to the 'decay-fit' method can be identified; A decrease in parameter uncertainty, the presence of viscous effects due to the waves, and the frequency used to determine the damping. Changes in the results of the two methods can be due a combination of these three aspects, and isolation of 1 aspect is challenging.

#### 4.3.1. Method

To obtain the 'regular wave-fit' damping, regular wave tests done at MARIN are compared with the regular wave tests as performed in aNySIM. The focus is put on the behaviour in surge and sway to determine the damping coefficients in surge and sway. Multiple regular wave tests are available for this damping method, and the choice was made to use the two tests with the wave period that is closest to the natural frequency in surge and sway, because around this frequency the damping is most influential. The tests selected are R-51 ( $T=7.05s$ ,  $H=1.5m$ ,  $\mu=180^\circ$ ) and R-55 ( $T=7.3s$ ,  $H=1.5m$ ,  $\mu=90^\circ$ ) for surge and sway respectively.

Similar to the 'decay-fit' damping determination, the linear and quadratic (implemented as drag coefficients) damping coefficients (see equation (3.40)) needed to be determined for each floater. These coefficients are similar for all floaters. Since a different drag coefficient resulted in different decaying behaviour in

Table 4.5: Overview of Damping coefficients for 'Decay-fit' and 'Regular wave-fit'

Damping coefficient	'Decay-fit'	'Regular wave-fit'	Percentage [%]
$B_{11}^{(1)} [kNm/s]$	1560	889.2	57
$B_{22}^{(1)} [kNm/s]$	5610	1402.5	25
$B_{11}^{(2)} [kNm^2s^{-2}]$	621	266	43
$B_{22}^{(2)} [kNm^2s^{-2}]$	-	1446	-
$C_x [-]$	2.37	1	42
$C_y [-]$	-	1	-

the "decay-fit" damping method, the effect of altering the drag coefficient was also studied for regular waves. This study, of which the results are shown in appendix E.3, showed that different drag coefficients have very little effect on the behaviour of the system in waves, solely the amplitude of the motions was influenced. This means that by fitting the regular waves with both the linear and drag coefficients, it is not possible to determine the ratio between linear damping and drag force. Therefore, it was decided to follow a theoretic approach and fix the drag coefficient to a set value for both surge and sway.

Research done on drag coefficients ( $C_d$ ) for different barges [28] shows that the drag coefficient for a barge with sharp edges is within a range of 0.9 to 1.15. For both directions (ie. surge and sway),  $C_d$  is set on 1. This results in different polar coefficients, depending on the incoming wave angle for both directions following equation (3.39).

Following from the fixed drag coefficient, the fitting procedure was solely done with the linear damping coefficient. Surge and sway motions were fitted by comparing the RAO's with the results from the basin tests. Comparing the RAO has been chosen instead of fitting the pure motion time trace, because the floater locations in the simulation model differ slightly from the floater locations in the basin tests, see section 4.1.2 for explanation. Furthermore, by analysing the RAO of the system, the mean value of the entire time trace (except for the start-up phase) is compared, instead of focussing on a small range. The linear damping coefficients that result in the RAO's in surge and sway with the best overall agreement for all 8 floaters (that were equipped with a motion censor) are selected for this 'regular wave-fit'.

### 4.3.2. Results

The applied 'regular wave-fit' method is used to obtain better agreement in regular wave tests. Therefore, results are presented for the regular wave motion RAO's of the specific tests (R-51 ( $T=7.05s$ ,  $H=1.5m$ ,  $\mu=180^\circ$ ) and R-55 ( $T=7.3s$ ,  $H=1.5m$ ,  $\mu=90^\circ$ )) that were used for the fitting. Thereafter, the results for the 'decay-fit' method and 'regular wave-fit' method are compared for all regular wave tests, the decay tests and irregular wave tests.

#### 'Regular wave-fit' results

Results for all eight floaters with the 'regular wave-fit' are shown in figure 4.12. The damping values implemented to obtain these results are shown in table 4.5, together with the 'decay-fit' results. As can be observed, a significant decrease in damping had to be implemented to compensate for the underestimation in motions of the 'decay-fit' damping implementation. Both the linear and quadratic terms of surge have been decreased by around 50%. The linear damping of sway has been decreased to only 25%, however, a quadratic term (drag) has been added to regain damping. As can be observed in both figure 4.12a as 4.12b, the damping coefficients give similar results for all floaters, indicating that no significant relative differences between the floaters are present. The RAO for the simulation model is now equal to the RAO of the basin tests for regular wave R-51 and R-55.

#### Regular wave tests comparison

Applying the 'decay-fit' and 'regular wave-fit' damping to all regular wave tests gives the results of the surge and sway RAO's shown in figure 4.13. Several comments can be made:

- The 'regular wave-fit' damping gives better overall results of the surge motion for the simulations in head waves (R-50, R-51 and R-52) compared to the results of the 'decay-fit' 4.13a. However, the natural frequency effect, explained in section 4.2.2 is still visible for the 'regular wave-fit' damping, resulting in a small overestimation of the RAO for R-50 and R-52.

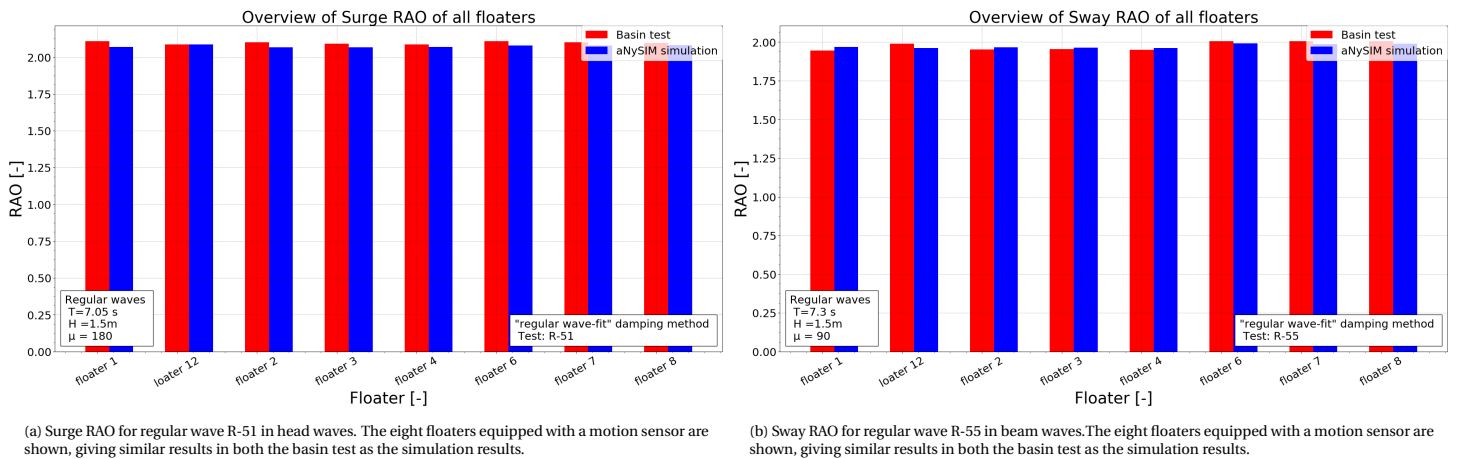


Figure 4.12: Motion RAO for eight floaters with 'Regular wave-fit' damping. The RAO's of the simulation model are equal to the RAO's of the basin test.

- The 'regular wave-fit' damping gives better overall results of the sway motion for the simulations in beam waves (R-53, R-54 and R-55) compared to the results of the 'decay-fit' in figure 4.13b. No natural frequency effect can be observed, due to the larger difference in wave period between the tests and the sway natural period ( $T_n = 8.1$ ).
- Observing tests R-56 ( $T=8s$ ,  $H=1.5m$ ,  $\mu = 170^\circ$ ), R-57 ( $T=9s$ ,  $H=1.5m$ ,  $\mu = 170^\circ$ ) and R-58 ( $T=10s$ ,  $H=1.5m$ ,  $\mu = 170^\circ$ ) a different effect becomes visible. The surge RAO is overestimated for the 'regular wave-fit' method for all three runs (figure 4.13a). The increase in RAO compared to the 'decay-fit' method becomes most visible for R-56, which is closest to the natural frequency in surge direction and therefore damping has most impact. This increase in RAO becomes less visible for R-57 and R-58, which is due to the fact that damping has less influence for these tests (referring to section 3.5, in which the influence of the damping force is set out for all tests).

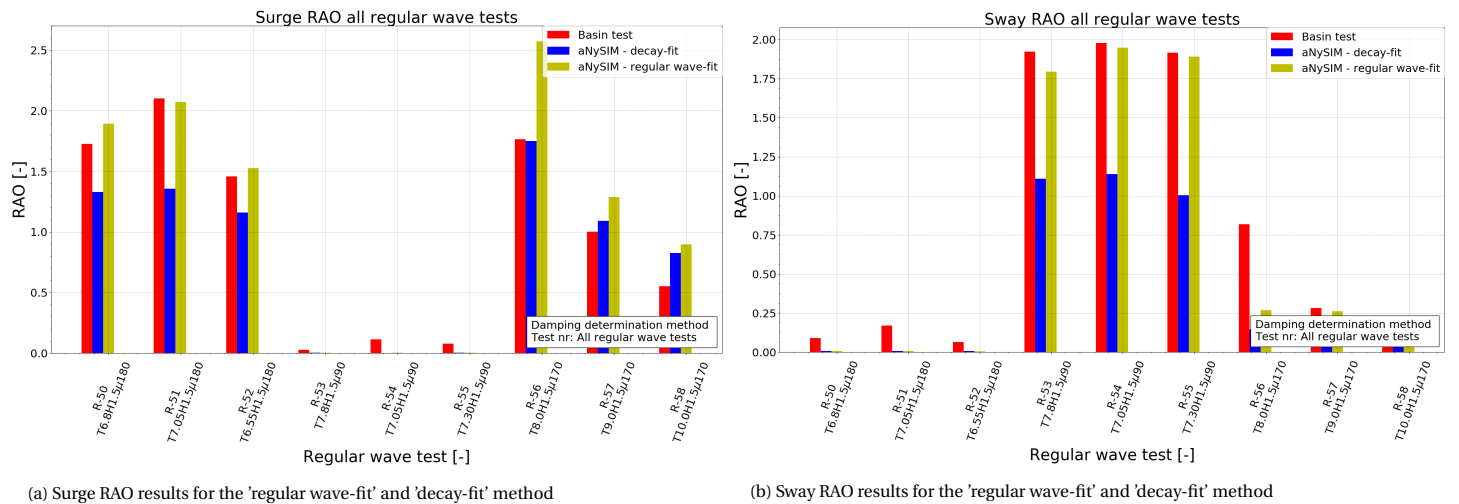


Figure 4.13: Motion RAO in surge and sway for all regular wave tests. The 'decay-fit', 'regular wave-fit' and the basin test results are shown.

### Decay tests comparison

Applying the 'regular wave-fit' results to the surge and sway decay tests shows an overestimation for the aNySIM simulation as can be observed in figure 4.14. This is expected due to the significant decrease in damping coefficients as shown in table 4.5. An explanation for this difference is that the viscous damping effects are significantly higher for decay tests in comparison to the regular wave test (as was explained in section 4.2.3). However, this is unlikely since it was expected that more viscous effects would be present in the regular wave tests.

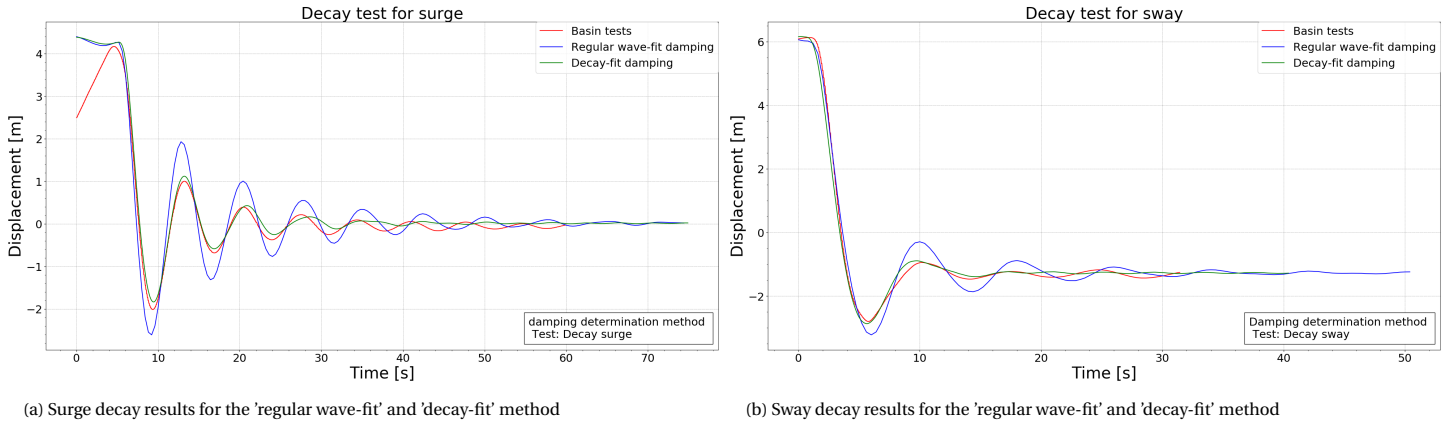


Figure 4.14: Comparison of decay simulations for the 'Regular wave-fit' damping, the 'decay-fit' damping and the basin tests results

### Irregular wave tests comparison

To analyse the effect of the different damping methods in irregular waves, irregular wave tests have been simulated with both the 'regular wave-fit' damping as the 'decay-fit' damping. For this purpose test I-3 ( $T_S=6.7s, H_S=2m, \mu = 180^\circ$ ) and I-6 ( $T_S=6.7s, H_S=2m, \mu = 90^\circ$ ) of the serviceability limit state (SLS) have been analysed, with wave directions in surge and sway direction respectively. These tests (see appendix A.1) both have a significant wave height of 2 metres and peak period of 6.7 seconds, parameters that are closest to the regular wave tests. This is done to (mostly) eliminate high sea state effects that influence the damping effects, and thus keep damping effects similar to the regular wave tests. Results from the irregular wave tests have been converted to a spectral density plot, to get insight in the overall agreement of the simulation with the basin tests, and in time traces, to give insight on the agreement in more detail for a given range in time. Figure 4.15 shows a selected time trace range for both surge and sway motion of run I-3 and I-6 respectively. Furthermore, the spectral density of these motions is shown in figure 4.16. Several observations can be made:

- In general, the aNySIM simulation is showing similar time trace behaviour as the basin tests results, with either an overestimation or underestimation in amplitude as a result of different damping implementation. This phenomenon can be observed in both 4.15a and 4.15b, where the 'decay-fit' method shows lower amplitudes and the 'regular wave-fit' method shows higher amplitudes.
- The spectral density plot for the 'decay-fit' damping is underestimated as compared to the basin test results for both surge and sway (figures 4.16a and 4.16b). This is according to the expectations following from the regular wave tests and can be observed in the time trace plots of figure 4.15. This underestimation can more strongly be observed for the sway motion of I-6 as shown in figure 4.16b.
- The regular wave-fit damping results overestimates the basin test results for both I-3 as I-6 (figures 4.16a and 4.16b). This is not according to expectations when observing the motion RAO's for the regular waves in figure 4.12, since the peak period is similar to the periods from the regular wave tests. It implies that different damping effects are present in the irregular wave tests than in the regular wave tests.
- The agreement with the basin test for sway motion of I-6 is better than for the surge motion of I-3. This implies that the damping in sway is more accurately determined.
- Observing the results for both tests, the 'regular wave-fit' results show a slightly better agreement with the basin tests results as compared to the 'decay-fit' method.

### 4.3.3. Concluding remarks

The 'regular wave-fit' method gives accurate in regular head and beam waves, where an improvement of 30-40% in motion amplitude compared to the 'decay-fit' method is obtained. Decay tests with the 'regular wave-fit' damping are overestimated.

Both methods result in oscillating behaviour in irregular waves of SLS that is in agreement with the basin test results but the amplitudes of the 'decay-fit' method are underestimated and the amplitudes of the 'regular wave-fit' method are overestimated. This means that the simulation model has incorporated most aspects of the equation of motion correctly, but uncertainties are still present. The inaccurate motion amplitudes from the 'regular wave-fit' method imply that these inaccuracies do not originate in parameter uncertainty. They

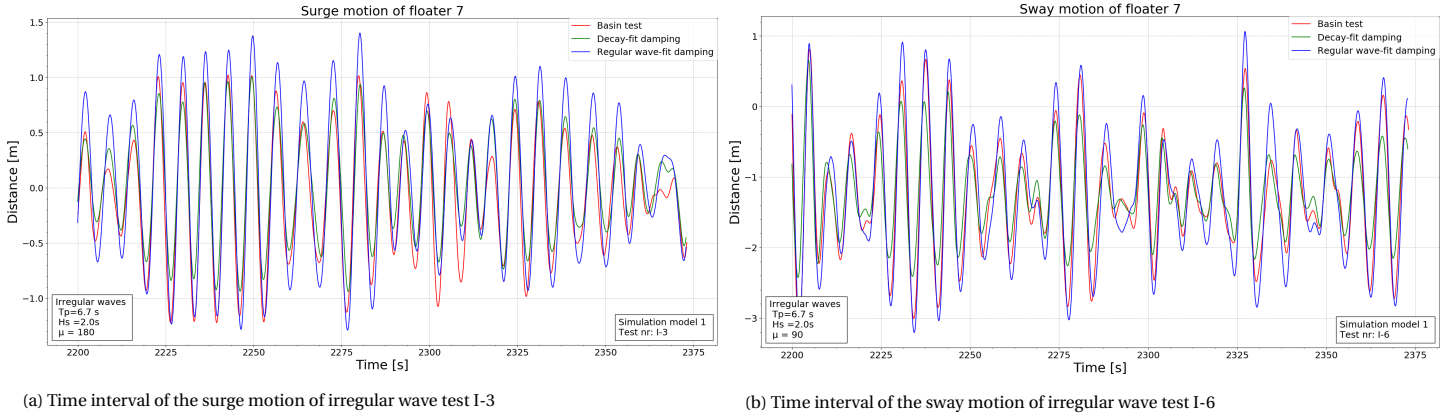


Figure 4.15: Comparison of irregular wave simulations for the 'Regular wave-fit' damping, the 'decay-fit' damping and the basin tests results

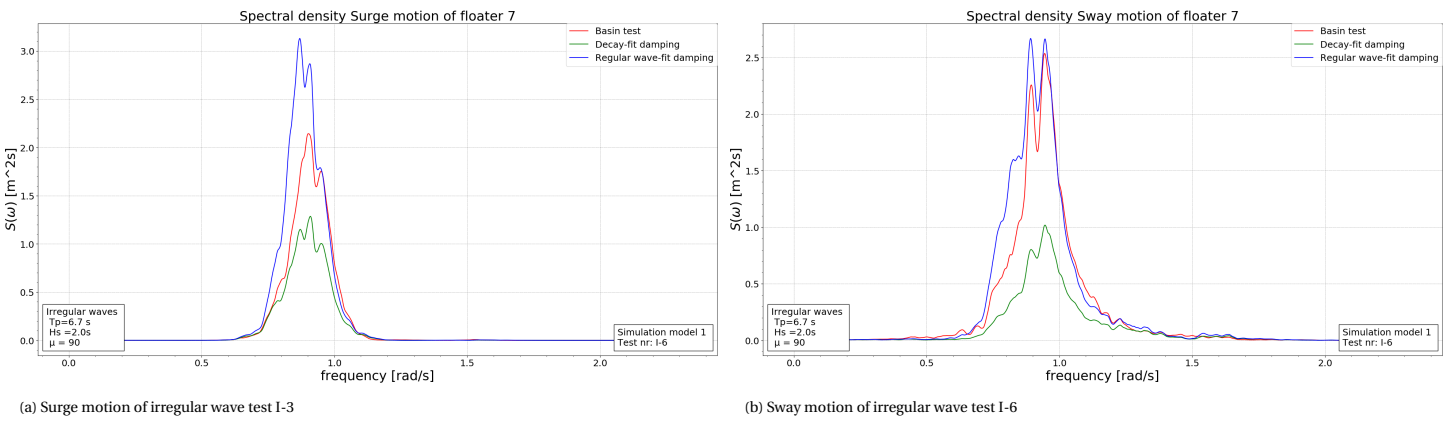


Figure 4.16: Comparison of irregular wave simulations using a spectral density for the 'Regular wave-fit' damping, the 'decay-fit' damping and the basin tests results

can be a result of the different frequency used in the 'regular wave-fit' method or model structure uncertainties (in which the viscous damping is not correctly implemented).

More analysis is required to draw a conclusion on the preferred damping method for this study. Therefore, the next chapter discusses the model accuracy in terms of mooring line force errors for all irregular wave tests, to compare the results of the two damping methods in further detail.

#### 4.4. Model accuracy

The previous sections served to analyse the difference between the 'decay-fit' and 'regular wave-fit' methods regarding the behaviour in decay tests, regular and irregular wave tests. To say something about the overall accuracy of the simulation model, the forces in the mooring lines were used since these are the most important factor in the design process.

To do so, the 10 highest forces occurring, and the corresponding moment of occurrence, in the irregular wave basin tests were determined. Both the 'decay-fit' damping method and the 'regular wave-fit' damping method were used to run the irregular wave tests and determine the force in the mooring lines at the specified moments of occurrence. The error that is present in the simulation models is calculated for the 10 highest forces as:

$$E_{F_{moor}} = (F_{moor-AS} - F_{moor-BT}) / F_{moor-BT} * 100\% \quad (4.6)$$

Where  $E_{F_{moor}}$  is the error in the mooring line forces,  $F_{moor}$  is the mooring line force, in either the aNySIM simulation (AS), or the basin test (BT) results. First, the error for the maximum force is analysed, whereafter the error for the 10 highest forces is presented.

### Error in maximum force

Table 4.6 shows the error that is present in the simulation model for the maximum force present in the basin test. Errors are given for all tests for each mooring line individually and for an average of the four mooring lines. As can be seen in the table, the mooring line forces in the simulation model are underestimated in almost all instances (small exceptions such as mooring line PSF (Port side front) of the 'regular wave-fit' in test I-9). What can be observed from the average values for all lines is that for each test the 'Regular wave-fit' method contains a smaller error than the 'decay-fit' method. However, looking at the lines individually, the 'decay-fit' method contains lower errors for a few instances (the errors in line PSA (Port side aft) and PSF for the tests I-12 and I-14). Generally, the errors become larger towards the higher sea states, implying that the agreement becomes less for higher sea states. The largest error for the 'decay-fit' method is an underestimation of 24% for line SBF (Starboard front) in irregular wave test I-13 ( $T_s 11.6 H_s 5.90 \mu 135^\circ$ ). The largest error for the 'regular wave-fit' method is 19% and occurs on the same line for the same test. This implies that the two methods give similar results that cause errors with the basin test.

Table 4.6: Error in mooring lines of the simulation model for maximum force that occurs in the basin test

	Decay fit					Regular wave fit				
	PSA	PSF	SBA	SBF	All lines	PSA	PSF	SBA	SBF	All lines
I-3	-7%	-7%	-9%	-7%	-7%	-3%	-4%	-5%	-5%	-4%
I-4	-6%	-2%	-6%	-5%	-5%	0%	1%	-3%	0%	0%
I-5	-11%	-6%	-4%	-6%	-7%	-9%	-5%	-1%	-4%	-5%
I-6	-11%	-12%	-5%	-5%	-8%	-11%	-11%	-4%	-3%	-7%
I-7	-15%	-4%	-8%	-10%	-10%	-8%	3%	1%	-3%	-2%
I-8	-13%	-11%	-3%	-4%	-8%	-13%	-10%	2%	-1%	-6%
I-9	-16%	-6%	-11%	-11%	-11%	-11%	3%	1%	-5%	-3%
I-10	-11%	-11%	-9%	-5%	-9%	-9%	-8%	-4%	0%	-6%
I-11	-18%	-10%	-15%	-15%	-15%	-13%	-1%	-4%	-11%	-7%
I-12	-15%	-15%	-13%	-11%	-13%	-18%	-15%	-10%	-8%	-13%
I-13	-22%	-12%	-19%	-24%	-19%	-17%	-1%	-10%	-19%	-12%
I-14	-14%	-14%	-11%	-8%	-12%	-15%	-17%	-6%	-2%	-10%

### Error in 10 highest forces

To see if the trends observed for the maximum force continues for the other high forces, the error is calculated for the 10 highest forces in the mooring lines. Results of these errors are obtained for all mooring lines separately and shown in figure 4.17 for test I-3 ( $T_s 6.7 H_s 2.0 \mu 180^\circ$ ) and I-6 ( $T_s 6.7 H_s 2.0 \mu 90^\circ$ ). When observing the median of the errors, the error for the 'regular wave-fit' is smaller than for the 'decay-fit' for all four mooring lines in both figure 4.17a and 4.17b. This is in agreement with the analysis of the irregular wave tests in section 4.3.2, showing better agreement for the 'regular wave-fit' method. However, the length of the whiskers (between the box and the non-outliers) is generally larger for the 'regular wave-fit'. This phenomena can be observed clearly for mooring line PSF in figure 4.17a and mooring line SBF in figure 4.17b. This indicates that the spreading of the errors is larger for the 'regular wave-fit', indicating that no 'constant' underestimation is present in the simulation, but that the behaviour is different as well.

Furthermore, the 'regular wave-fit' method contains positive errors for lines PSF and PSA in figure 4.17a and for lines SBF and SBA (Starboard aft) in figure 4.17b. This was not observed for test I-3 and I-6 in table 4.6.

For irregular wave test I-6 (figure 4.17b), the errors for the 'decay-fit' method are all within the range of the errors for the 'regular wave-fit' (this can be observed by the fact that the entire boxplot of the 'decay-fit' is within the range of the box plot of the 'regular wave-fit'). This fortifies the finding that the errors of the 'regular wave-fit' method have a larger spreading.

Overall, it can be observed that the maximum mooring line forces in both simulations contain relatively small errors, and that the overall agreement of the 'regular wave-fit' method is higher than for the 'decay-fit' method, but that the spreading of errors is lower for the 'decay-fit' method.

Analysing all other wave tests has resulted in similar plots, which can be observed in appendix F.1. Tests I-13 and I-14 are shown in figure 4.18 to show the results for the higher sea states of the bridging tests. Test I-13 ( $T_s 11.6 H_s 5.90 \mu 135^\circ$ ) can be observed in figure 4.18b. This tests contains oblique waves. As a result, the

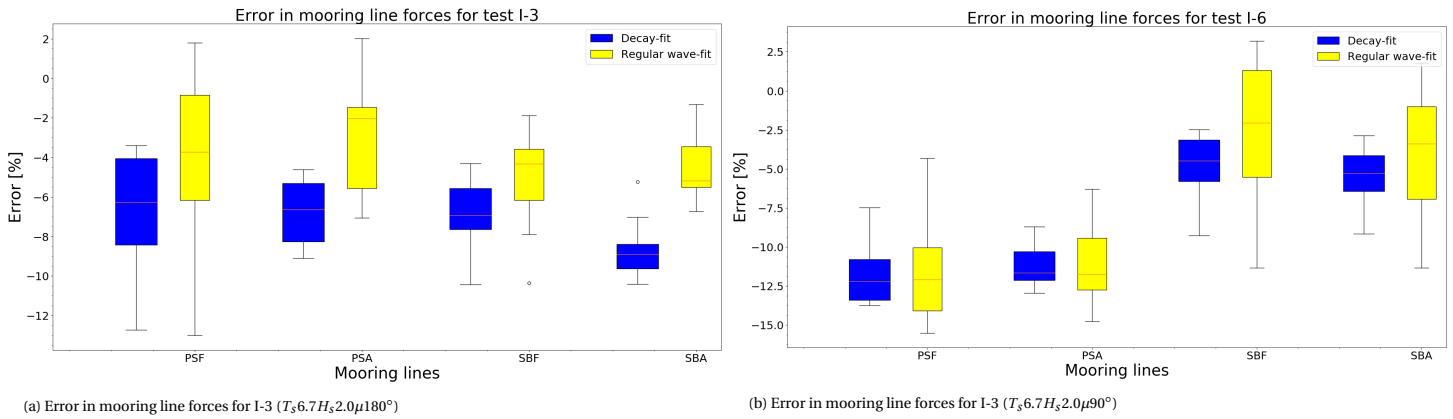


Figure 4.17: Error in mooring line forces for the 10 highest forces obtained from the basin tests. Errors are shown for the 'decay-fit' method and the 'regular wave-fit' method for all 4 mooring lines.

difference between the errors in the mooring lines is relatively large for the regular wave fit (the median for PSF is around 0%, whereas the median for SBF is around 20%). Furthermore, the underestimation for both methods is much larger than observed for tests in head (I-3) or beam waves (I-6). This is presumably a result of the oblique incoming waves and the increasing sea state.

As can be observed for test I-14 ( $T_s 11.6H_s 5.90\mu 90^\circ$ ), again, the underestimation for lines PSF and PSA for both methods becomes larger, which is in line with the trend shown in table 4.6. However, for lines SBF and SBA, both methods contain negative and positive errors, meaning that for some maxima, the simulation overestimates in high waves. This means that the overall agreement of the simulation model becomes less as different behaviour starts to occur.

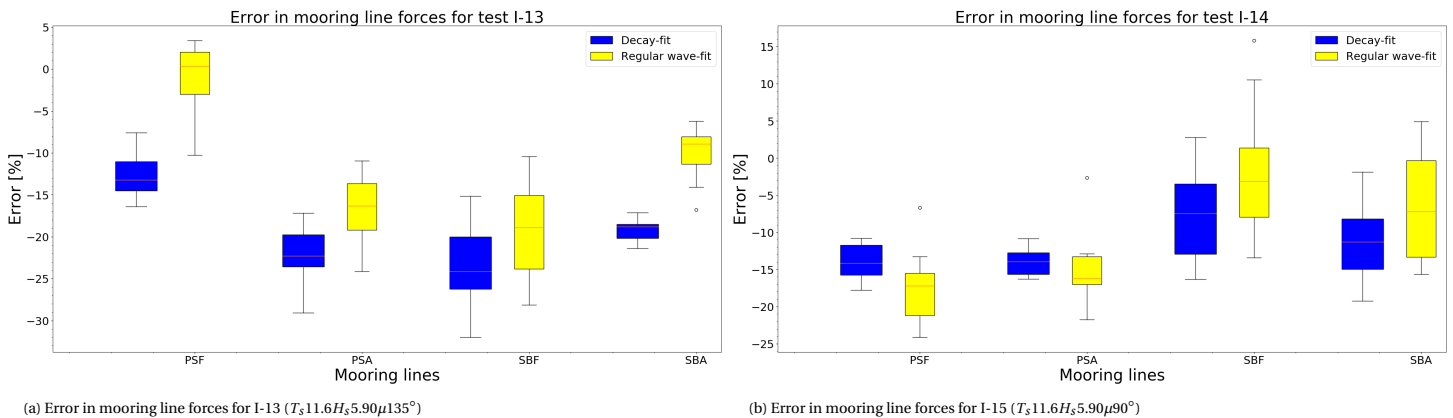


Figure 4.18: Error in mooring line forces for the 10 highest forces obtained from the basin tests. Errors are shown for the 'decay-fit' method and the 'regular wave-fit' method for all 4 mooring lines.

Combining all tests, an overall error is calculated for the individual mooring lines in the serviceability state and the bridging states in oblique and beam waves. These errors can be observed in 4.7. For this calculation, the mean error is calculated over the 10 maximum forces. These results show that for the SLS, the average errors are within 10% for both the 'decay-fit' as the 'regular wave-fit'. As presented in chapter 1, this is deemed to be acceptable for engineering purposes. The error becomes larger for both the bridging-oblique waves as the bridging-beam waves, where the error from the 'regular wave-fit' method is significantly smaller in bridging-oblique waves than the error from the 'decay-fit' method. This difference is less visible in the bridging-beam waves, where the portside lines (PSF and PSA) give the same results for the two methods.

Furthermore, a difference between the lines on starboard side (SBF and SBA) and the lines on portside (PSF and PSA) in the bridging beam waves becomes clear, with lower errors for the starboard side in both methods. This indicates that there is a difference in the simulation accuracy for the starboard and portside lines.

Table 4.7: Overview of the mean error in the mooring lines for the 10 highest forces. The mean error is calculated for the SLS, bridging in oblique waves and bridging in beam waves.

	SLS				Bridging oblique waves				Bridging beam waves			
	PSA	PSF	SBA	SBF	PSA	PSF	SBA	SBF	PSA	PSF	SBA	SBF
Decay-fit	-9%	-7%	-6%	-6%	-18%	-8%	-13%	-15%	-13%	-13%	-9%	-7%
Regular wave fit	-6%	-5%	-3%	-3%	-12%	1%	-3%	-10%	-14%	-13%	-5%	-3%

Table 4.8: Accuracy results of regular wave tests using the scale as defined in table 5.1

Mooring line	I-3	I-4	I-5	I-6	I-7	I-8	I-9	I-10	I-11	I-12	I-13	I-14
PSF	Green	Green	Green	Green	Green							
PSA	Green	Green	Green	Red	Orange							
SBF	Green	Orange	Green	Orange	Orange	Orange						
SBA	Green	Orange	Green	Orange	Orange	Orange						

#### 4.4.1. Data outliers

As explained in section 2.2.2, breaking waves and slamming effects occur irregularly in the basin tests, increasing in occurrence towards higher waves. These effects can cause high incidental forces in the mooring lines. Therefore, the occurrence of the maximum forces in the mooring lines have been studied in the video footage. Table 4.8 shows the findings for all irregular wave tests. Green means that no notable physical conditions such as breaking waves were observed. For the orange results, small breaking wave effects are observed. Red means that a large breaking wave incident is observed. This means that for the final 2 tests (I-13 and I-14), with a significant wave height of 5.90 metre and a peak period 11.60 seconds, the maximum mooring line forces are related to breaking wave effects. Simultaneously, the errors in the simulation model are highest for these tests (see figure 4.6).

## 4.5. Conclusion

It can be concluded that the static behaviour of the simulation model is validated and that the simulation model shows similar oscillating behaviour in for regular wave tests and irregular wave tests in serviceability limit state. This means that simulation model is capable of capturing most physical phenomena that determine the behaviour.

However, by applying the conventional damping method 'decay-fit', errors in force and motion amplitudes are introduced for the regular and irregular waves. These errors become more significant towards the natural period of the system, implying that damping was determined inaccurately. A cause for this inaccuracy is classified as parameter uncertainty in the simulation model.

A new damping method has been introduced: the 'regular wave-fit' method. Results show inaccuracies in irregular sea state amplitudes, that can be ascribed to the regular wave tests that was selected for damping determination or to model structure uncertainties.

Comparing the mooring line forces for both methods showed that the simulation accuracy for the SLS states is within an error of 10% from the basin tests. The highest errors are present in the highest sea state in oblique waves, with a maximum error in the 'decay-fit' method of -24% and a maximum error of -19% for the 'regular wave-fit' method. These errors are related to breaking wave incidents in the basin test.

An improvement of average 4% can be observed for the 'regular wave-fit' as compared to the 'decay-fit' method. The inaccuracies in this model that are caused by the fact that damping was not determined at the natural frequency of the system are smaller than the inaccuracies caused by parameter uncertainty in the 'decay-fit' method.

The increase in errors towards higher sea state and differences between the different mooring line forces indicate that model structure uncertainty is present in the simulation model.

The next chapter addresses this model structure uncertainty in the simulation model by means of an uncertainty analysis. For this analysis, the 'regular wave-fit' model results are used, since a higher accuracy in irregular waves was obtained.

# 5

## Uncertainty analysis

Following from the analysis and conclusions of chapter 4, the simulation model with the 'regular wave-fit' damping implementation does not give accurate results for the irregular wave tests. The conclusion was drawn that this is partly caused by parameter uncertainty due to the damping determination and partly due to possible model structure uncertainties in the model.

The goal of this chapter is to identify model structure uncertainties. To do so, an uncertainty analysis was performed: a study on the inaccuracies in the simulation model and identification of possible causes for these inaccuracies. This is related to research question 4, as introduced in chapter 1. First, the method to perform this analysis is explained, whereafter the results are presented and a conclusion is drawn.

### 5.1. Method

The accuracy of the simulation model using the 'regular wave-fit' damping was identified for all regular and irregular wave tests. This accuracy was determined by analysing both spectral density plots (irregular waves) and RAO's (regular waves) as time traces of the signals, where the motions in all 6 DOF were taken into account as well as forces in all mooring lines. Trends were identified that could be observed in the motions and mooring line forces over a range of tests. A different approach is used for the regular and irregular waves.

#### Regular waves:

To get a first idea of the trends that occur, a simplified scale of agreement was applied to the results in terms of accuracy regarding the motion amplitudes. This scale can be observed in table 5.1. A note must be made that this scale was not quantified by the error that is present in the results but is subjective, since it only serves as a quick overview. The results were observed in more detail to further analyse the effects.

#### Irregular waves:

For irregular wave tests a distinction has been made between accuracy of the motion amplitudes and oscillating behaviour. The former is identified using the same scale as for regular waves, where the accuracy is judged for the peak frequency amplitudes (using spectral density plots). The latter is identified using the scale as shown in table 5.2, using the time trace plots.

To perform the uncertainty analysis, the trends have been linked to the physical phenomena present in the experiments (see section 2.2.2) and the test characteristics. To do so, findings from the preliminary sensitivity study (see section 3.5) have been used for more context and support on the expected behaviour.

Table 5.1: The used scale for amplitude accuracy of simulation model

Response at wave frequency	Weight
Strongly underestimated	-10
Underestimated	-5
Slightly underestimated	-2
Accurate	0
Slightly overestimated	2
Overestimated	5
Strongly overestimated	10

Table 5.2: The used scale for oscillation accuracy of the irregular wave tests

Oscillating behaviour	Weight
Accurate	4
Almost accurate	3
Little accuracy	2
Inaccurate	1

Table 5.3: Accuracy results of regular wave tests using the scale as defined in table 5.1

Test	R	T	H	Angle	Surge	Sway	Heave	Roll	Pitch	Yaw
Head waves	50	6.80	1.5	180	0	-10	0	0	0	-10
	51	7.05	1.5	180	0	-10	-5	0	-2	-10
	52	6.55	1.5	180	0	-10	0	0	0	-10
Beam waves	53	6.80	1.5	90	-10	0	-2	0	-5	-10
	54	7.05	1.5	90	-10	0	2	-2	-5	-10
	55	7.30	1.5	90	-10	0	0	0	-5	-10
Oblique waves	56	8.00	1.5	170	5	-5	5	0	5	-2
	57	9.00	1.5	170	10	-2	5	5	2	-5
	58	10.0	1.5	170	10	5	5	2	2	-5

## 5.2. Regular wave test results

All regular waves tests have been analysed for behaviour in all 6 DOF and forces in the four mooring lines. Table 5.3 gives a summarised overview of the general agreement of the floaters and mooring lines amplitudes for regular waves, for which the scale as defined in table 5.1 has been used. Striking trends are discussed below. The regular wave tests were divided in three parts, that are repeated here for convenience:

- *Head waves - Test R-50, R-51, R-52*

These tests serve mainly to analyse the behaviour of the system in surge, with wave periods near the natural frequency of the system in surge direction.

- *Beam waves - Test R-53, R-54, R-55*

These tests serve mainly to analyse the behaviour of the system in sway direction, with wave periods near (but somewhat lower than) the natural frequency of the system in sway direction.

- *Oblique waves - Test R-56, R-57, R-58*

These tests have an incoming wave angle of 170 deg and increasing wave periods. The tests mainly serve to analyse the behaviour of the system in longer waves, where the small wave angle causes some effects in both surge and sway and therefore a higher system rotation.

### 5.2.1. Surge and sway motion in head and beam waves

From the applied method of 'regular wave-fit' damping, the surge and sway motion in head and beam waves respectively are simulated accurately (see figure 4.13). On the other hand, the surge and sway motion perpendicular to the incoming wave direction are strongly underestimated in the simulation model. This underestimation is caused by the difference in orientation of the floaters between the basin tests and the simulation model (see section 4.1.2). Smaller initial yaw angles in the simulation model cause a motion response that is purely in the wave direction, whereas a small motion response perpendicular to the incoming wave angle can be observed in the basin tests. Due to these small amplitudes (<7% of the motion parallel to the incoming wave direction), the absolute error is negligible.

### 5.2.2. Surge and sway motion in oblique waves

Observing the accuracy trends of regular wave tests R-56, R-57 and R-58 in table 5.3, a different trend compared to head and beam waves is observed. The surge motion is overestimated for all three tests, and the sway motion is underestimated for R-56 and overestimated for R-57 and R-58. The trends in surge and sway are related to each other, both showing an increase in motion amplitude for the simulation model compared to the basin test results. The influence of damping is addressed first:

- The amplitude of the motions for R-56 and R-57 is influenced by damping (as shown in the analysis of the 'decay-fit' and 'regular wave-fit' method in section 4.3.2). However, the effect of different damping is negligible for R-58, in which overestimation of the motion is still observed.
- Difference in physical damping effects between the oblique tests and the head and beam wave tests are present, but the expectation is that these damping effects are lower for oblique waves in the basin tests (this is discussed in section 2.2.2). This would result in larger motions in the basin tests and thus an underestimation of the simulation model.

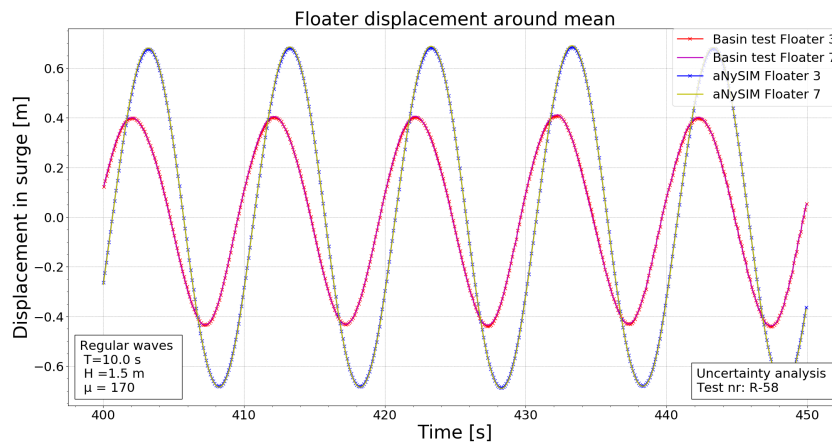


Figure 5.1: Surge motion of floater 3 and 7 around their equilibrium position. For both the simulation model as the basin test results, the relative motion between the two floaters is negligible.

From these observations, it is concluded that viscous damping effects influence the results but are not the root cause for this inaccuracy. The test characteristics and physical phenomena are observed to find the root cause of this inaccuracy. The oblique waves differ from the head and beam waves in three aspects: The incoming wave angle, the wave length and the wave steepness (since the wave height remains the same). Due to the longer wave period, spring forces become more dominant in the motion response (see figure 3.8, in which the tests are classified according to the governing force).

Spring forces in surge and sway are accounted for in the mooring lines and joints. The mooring line behaviour is validated in 4.1.2 and is considered to be accurately implemented for these wave tests. The surge motion of floater 3 and 7 is shown around their equilibrium position in figure 5.1. The figure shows that for both the simulation model as the basin test results, the two floaters show the exact same behaviour. This means that the relative motions between the floaters is negligible and that despite the oblique incoming wave angle, the system still behaves as one and joint forces are not the root cause of the overestimated surge and sway motion.

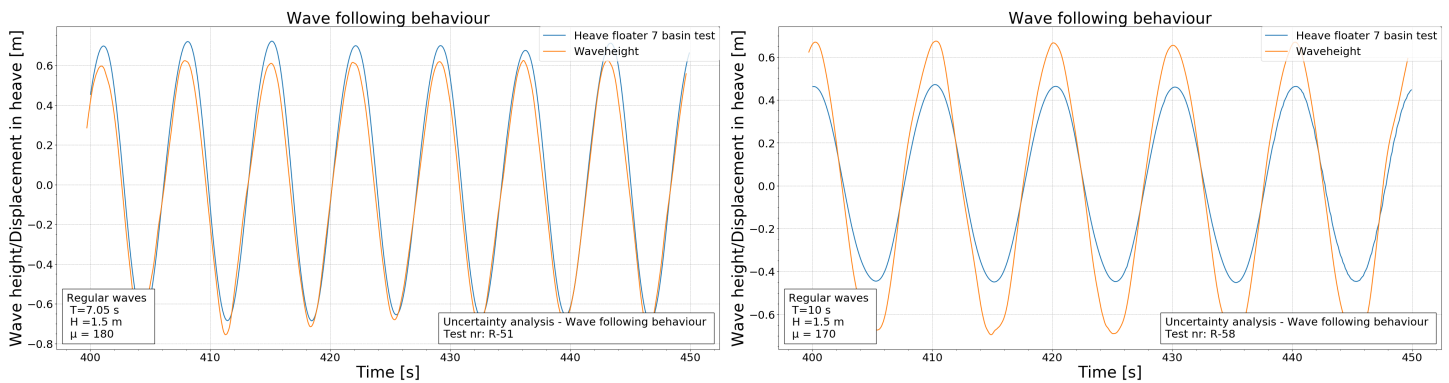
However, as the figure also shows, a negative phase shift between the simulation model and the basin tests is present. More research is required into the cause of this phase difference which is expected to be related to the overestimation of the simulation model.

### 5.2.3. Heave motion

Table 5.3 shows that the heave motion is accurately determined for most head and beam wave tests. This confirms the statement that viscous forces are negligible in heave for this design (see section 3.5), as the motions are simulated accurately without viscous damping implementation. However, the motion is overestimated in the oblique waves. The test characteristics and physical phenomena are observed to find the root cause of this inaccuracy.

The system in regular waves showed clear wave following behaviour in heave motion (see figure 2.5 for illustration). This behaviour is influenced by the wave length [13] and therefore differs for the oblique waves (where the wave length has increased compared to head and beam waves). This effect is shown in figure 5.2, where the heave motion of floater 7 and the wave elevation are shown. For both regular wave test R-51 (figure 5.2a) as R-58 (figure 5.2b), the heave motion follows the wave elevation (the two signals have the same phase and similar oscillating behaviour). However, a difference can be observed regarding the amplitudes. For the heave motion of regular wave test R-58, the amplitudes are smaller than the wave elevation. For the maximum heave amplitude the floater is submerged more than at still water level, and at the minimum heave amplitude the floater is less submerged. This effect cannot be observed for regular wave test R-51. This difference affects the buoyancy force acting on the floater: In aNySIM, this force is calculated based on the floater location compared to the still water level, whereas in the basin tests, the instantaneous water level is taken into account. A non-linearity in buoyancy force due to the wave following behaviour effect of R-58 is present in the basin test but is not taken into account in the simulation model. The buoyancy force is the largest hydrodynamic force in heave (this is visualised in figure G.5b in appendix G) and therefore a small error in calculation affects the heave motion amplitude, causing the overestimation of the heave motion for

oblique regular waves.



(a) Heave motion of floater 7 and wave elevation, showing the 'wave following' behaviour for head wave test R-51.

(b) Heave motion of floater 7 and wave elevation, showing the 'wave following' behaviour for oblique wave test R-58.

Figure 5.2: Basin test results for the heave motion and the wave elevation. A difference in amplitude of the heave motion compared to the wave elevation can be observed for test R-51 and R-58.

#### 5.2.4. Roll and pitch motion

Table 5.3 indicates that the roll motion is simulated accurately for the head and beam wave tests, implying that viscous damping is indeed not a significant factor as shown in section 3.5, and that all other forces are accurately determined in the simulation model. This accurate simulation of the roll motion is striking, since the general experience with simulation models for offshore systems is that the roll motion is very hard to accurately determine, and that viscous effects do play a role in for instance a connected FPSO-LNG system[9]. A cause for this difference can be found in the small dimensions of this system, due to which the viscous effects on roll are less significant as compared to the larger offshore systems.

The pitch motion is simulated accurately for head waves, implying that, similar to roll, the viscous effects are not important and all other forces are accurately determined in the simulation model. However, the pitch motion is underestimated for beam waves, which is likely to be a result of fact that pitch motions in the simulation model are much smaller in beam waves due to the orientation of the system (similar to the surge motion in beam waves).

Both motions (roll and pitch) are overestimated for the oblique wave tests, showing similar trends as for surge, sway and heave. Similar to the heave motion, this inaccuracy can be related to *wave following behaviour* as explained in section 2.2.2. Due to low steepness of the waves, the floater rotation follows the direction coefficient of the wave. This results in different added mass, damping and restoring force for the basin tests.

#### 5.2.5. Yaw motion

The yaw motion is strongly underestimated in head and beam waves. This is a result of the floater orientation difference between the basin tests and the simulation model. Due to the symmetric orientation in the simulation model, motion response is purely in the wave direction, also resulting in negligible yaw motions. The floaters in the basin tests have a larger initial yaw angle, inducing (small) motion responses in yaw. For oblique waves, the underestimation becomes smaller as a result of the oblique incoming wave angle, due to which a yaw motion is introduced in the simulation model as well. Due to the viscous damping implementation in yaw, which has been determined from decay tests, the motion response is still underestimated in the simulation model. However, since the amplitude of the yaw motion is around 0.5 degrees in the basin test results for the oblique waves and even lower for the head and beam waves, the effect on the mooring line forces is insignificant.

### 5.3. Irregular wave test results

Irregular waves I-3 to I-14 results have been analysed for behaviour of 8 floaters in all 6 DOF and the four mooring line forces. Table 5.4 shows a summarised overview of the general amplitude accuracy of the motions and mooring line forces for irregular waves using the scale as defined in table 5.1. Table 5.5 gives an overview

of the oscillating behaviour accuracy for the motions of the system. For this analysis, the classification of irregular waves as defined in chapter 2 has been used:

- *Serviceability limit state (SLS) – Tests I-3, I-4, I-5 and I-6*  
These tests have the same wave height (2m) and wave period (6.8s) with incoming wave angles of 180, 135, 105 and 90 degrees. The effect of an altering wave angle can be analysed with these tests. Furthermore, due to their close similarity to the regular waves, a comparison in behaviour can be made.
- *Bridging states, beam waves – Tests I-8, I-10, I-12, I-14*  
The bridging state tests have an increasing wave height and wavelength and serve to analyse the effect of these increasing sea states. Four increasing sea states are tested for beam waves ( $\mu = 90^\circ$ ). These tests allow for an analysis of the system with a dominating sway motion, where surge motions can be neglected.
- *Bridging states, oblique waves – Tests I-7, I-9, I-11, I-13,*  
The bridging state tests have an increasing wave height and wavelength and serve to analyse the effect of these increasing sea states. Four increasing sea states are in oblique waves ( $\mu = 135^\circ$ ). These tests allow for analysis of the system where both surge and sway motions are present, and the system experiences more yaw rotation.

Using both tables, several inaccuracy trends were identified that are discussed below.

Table 5.4: Summarised overview of the results of irregular wave tests using the scale as defined in table 5.1

Test	I	Tp	Hs	Angle	Surge	Sway	Heave	Roll	Pitch	Yaw
Service-ability limit state	3	6.70	2.0	180	5	-10	0	0	0	-10
	4	6.70	2.0	135	5	0	0	0	0	-2
	5	6.70	2.0	105	-5	5	5	0	5	-2
	6	6.70	2.0	90	-10	2	-2	2	-5	-5
Oblique	7	8.00	2.90	135	5	-5	-5	0	2	-5
Beam	8	8.00	2.90	90	-10	5	2	2	-5	-5
Oblique	9	9.20	3.75	135	5	-5	-5	0	0	-2
Beam	10	9.20	3.75	90	-10	2	-2	0	0	-5
Oblique	11	10.40	4.75	135	0	-5	-5	-2	-2	-5
Beam	12	10.40	4.75	90	-10	-5	-5	-2	-5	-5
Oblique	13	11.60	5.90	135	-5	-5	-5	-2	0	-10
Beam	14	11.60	5.90	90	-10	-2	-2	-2	-10	-5

Table 5.5: Summarised overview of the oscillation accuracy of irregular wave tests using the scale as defined in table 5.2

I	Tp	Hs	Angle	Surge	Sway	Heave	Roll	Pitch	Yaw
3	6.70	2.0	180	4	1	4	4	4	1
4	6.70	2.0	135	4	4	4	4	4	4
5	6.70	2.0	105	4	4	4	4	4	4
6	6.70	2.0	90	1	4	4	4	4	1
7	8.00	2.90	135	4	4	4	4	4	4
8	8.00	2.90	90	1	4	4	3	1	2
9	9.20	3.75	135	4	4	4	3	3	4
10	9.20	3.75	90	1	4	4	2	1	2
11	10.40	4.75	135	3	3	3	3	3	3
12	10.40	4.75	90	1	3	3	2	1	2
13	11.60	5.90	135	2	2	2	2	2	2
14	11.60	5.90	90	1	3	3	2	1	2

### 5.3.1. Motion amplitude accuracy SLS

From table 5.4 it becomes clear that in the SLS, the motion in surge and sway is overestimated for head and beam waves respectively. This is shown in figure 5.3 for the surge motion of test I-3. The SLS tests have a peak period  $T_p = 6.7$ , which is relatively close to the natural period in surge and sway and therefore the damping effects have a large influence on the system behaviour. Additionally, this peak period is close to the period at which the damping was determined for the 'regular wave-fit' ( $T=7.05$  for surge and  $T=7.3$  for sway), but not exactly the same. This means that frequency dependent damping effects differ for the SLS tests compared to the regular waves. Finally, from the physical analysis in section 2.2.2, different damping effects have been identified for the irregular wave tests compared to the regular wave tests, logically resulting in more damping in the irregular waves. Therefore, the cause of this overestimation is related to viscous damping effects.

#### Coupled pitch-surge damping

The first effect as was observed in the video footage, are vortices around the floaters that become more apparent in irregular wave tests. These vortices are, amongst others, a result of the wave steepness. The irregular waves have a steepness  $H/\lambda = 0.28$  (observing the peak period and significant wave height), whereas the highest steepness for regular waves is  $H/\lambda = 0.022$ . The physical analysis showed that steeper waves are related to more vortex generation around the floaters.

A direct consequence of a change in steepness is a different pitch behaviour. Table 5.6 shows the pitch motion amplitude for the regular head and oblique wave tests and the SLS test in head waves. All tests have a different wave steepness. A clear decrease in pitch motion can be observed for the longer oblique waves with

lower steepness. Observing the SLS test I-3, the (significant) pitch amplitude is much higher than the pitch amplitude for the regular head waves. Following from this larger amplitude, the (significant) pitch velocity increases for the SLS test as well. Relating the vortices to the pitch velocity of the floaters, this effect can be accounted for as a *coupled pitch-surge damping effect*. The phenomenon is explained using the surge motion, but similar effects are present for the sway motion.

Table 5.6: The pitch motion and velocity amplitudes for regular waves and the irregular wave I-3 with different wave periods and steepness factors. Note that for the irregular wave test, the significant wave height, peak period and significant pitch amplitude are given.

	Wave period [s]	Wave height [m]	Wave angle [deg]	Mean pitch motion amplitude [deg]	Steepness [-]
R-50	6.80	1.5	180	3	0.021
R-51	7.05	1.5	180	3	0.019
R-52	6.55	1.5	180	3.2	0.022
R-56	8.00	1.5	170	2.5	0.015
R-57	9.00	1.5	170	1.6	0.012
R-58	10.00	1.5	170	1.6	0.010
I-3	6.7	2.0	180	5	0.028

### Shielding in drag

The second damping effect is related to the flow disturbances due to the presence of the floaters, described as a *shielding effect* in section 2.2.2. This shielding effect is present for both excitation forces as damping effects. Due to more flow disturbances in irregular waves (as compared to regular waves), this shielding effect becomes more significant. In figure 5.4, this effect is presented for the first order excitation force, but similar reasoning can be used for the viscous damping effects. As can be observed, the excitation force in sway direction of floater 4 differs significantly from floaters 1, 2 and 3. The difference becomes more visible towards higher frequencies. For the regular waves, the system is only excited at one frequency, at which this shielding effect is incorporated in the viscous damping of all the floaters. Additionally, the regular wave frequencies are between 0.86 and 0.92 for beam waves. The shielding effect for these frequencies is still relatively small. However, for irregular waves, multiple frequencies are excited (this is shown in figure 5.3 for irregular wave I-6, showing spectral density of the wave height over wave frequency). This means multiple shielding effects are present. Additionally, the shielding effect for the peak frequency of I-6 ( $T_p = 6.7, \omega_p = 0.93$ ) is different than for the regular wave test that was used to fit the damping ( $T_p = 7.3, \omega_p = 0.86$ ).

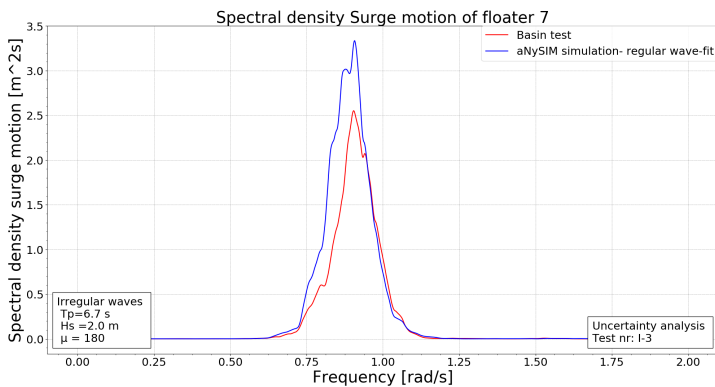


Figure 5.3: Spectral density of the surge motion for irregular wave test I-3, showing an overestimation of the simulation model.

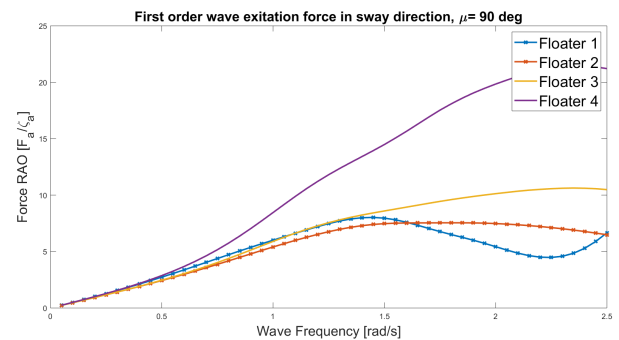


Figure 5.4: Excitation force RAO obtained from DIFFRAC for four floaters in sway motion.

### Mooring line dynamics

The third effect is related to the mooring line dynamics as presented in section 2.2.2. As discussed, mooring line damping is often related to the low frequency motions of the system but since the natural frequency of this system is within the wave exciting frequency range, mooring line damping is expected to have a significant influence in the SLS tests. This is substantiated by the trend that for all incoming wave angles in the SLS tests, inaccuracies are present in surge and sway (see table 5.4). This strongly indicates that damping effects influence the system behaviour that are independent on the system direction. Damping on the mooring lines

Table 5.7: Wave characteristics of the tests in which the simulations underestimate the system behaviour

Test nr	Motion	Tp	Hs	Angle
I-11	Surge oblique waves	10.4	4.75	135
I-12	Sway beam waves	10.4	4.75	90
I-7	Sway oblique waves	8	2.9	135

effects the system in the direction parallel to the wave and will therefore have impact in all wave directions on both surge and sway.

### 5.3.2. Motion amplitude accuracy bridging tests

Observing table 5.4, the motion amplitude starts to get underestimated towards the higher sea states. The test characteristics of the wave tests at which this effect becomes visible are noted in table 5.7. Figure 5.5 illustrates this effect for the surge motion of I-11 and I-13. As can be observed in for both tests, two peaks are present, indicated with the dashed black lines. One at the wave exciting peak frequency ( $\omega_p = 0.60$  for figure 5.5a and  $\omega_p = 0.54$  for figure 5.5a) and one at the natural frequency of the system in surge ( $\omega_n = 0.83$ ). The peak at the natural frequency is overestimated in the simulation model results (this is caused by the difference and increase in viscous damping effects as explained in section 5.3.1), but the peak at the wave peak frequency is underestimated. Several comments can be made regarding the effect and possible causes for inaccuracy:

- The effect is independent of the incoming wave angle, as it occurs for sway in both beam and oblique waves.
- Compared to the SLS tests where motions are overestimated, both the wave height and wave period are altered, causing possible inaccuracies.
- From the analysis of governing forces (see section 3.5, figure 3.8), the peak period of irregular wave test I-11 ( $T_p = 10.4$ ) is located in the transition area between the damping and spring forces for both surge and sway. This means that around the peak frequency spring terms become more important.

The important spring terms originate in the mooring lines and the joint stiffness;

- The mooring system implementation has been validated in section 3.4.3.
- Following from the analysis on system behaviour in section 2.2.2, the relative motions between the floaters in beam waves are negligible, implying that joint forces do not play a significant role in the system behaviour.

Therefore, the mooring line and joint stiffness are not identified as the cause for this inaccuracy.

As was observed in section 2.2.2, the increase in wave height introduces more overflowing water and more flow disturbances that can be related with viscous effects. Although their impact decreases (see section 3.5) these damping effects still influence the behaviour for longer waves, and an inaccuracy can stem from the fact that damping has been defined for a different frequency, where other damping effects are present (following from the 'regular wave-fit' method as described in section 4.3).

Isolating the root cause of this behaviour requires more experimental data. Tests should be performed where only 1 parameter is changed at the time (wave height, wave period and incoming angle).

### 5.3.3. Oscillating behaviour

Table 5.5 has been used to identify trends and notable behaviour regarding the oscillating behaviour of irregular wave test simulations.

#### Oscillating behaviour: surge and sway

As shown in table 5.5, the oscillating behaviour for surge and sway is accurately determined up to a wave height of 4.75 metre (I-11), after which small differences start to occur. Section 4.3.2 has presented the oscillating accuracy for the SLS tests. To visualise the difference occurring in higher sea states, figure 5.6 shows a time trace range of the sway motion for test I-11 ( $T_p 10.40 H_s 4.75 \mu 135^\circ$ ) and I-14 ( $T_p 11.6 H_s 5.90 \mu 90^\circ$ ).

The sway motion in figure 5.6a shows a similar oscillating period but the simulation model has a positive phase shift as compared to the basin test results for the entire time trace. Similar results were observed for the surge motion of I-11. However, this phase shift cannot be observed in figure 5.6b for the sway motion (with a higher sea state). A cause for this phase difference is therefore related to the difference in incoming

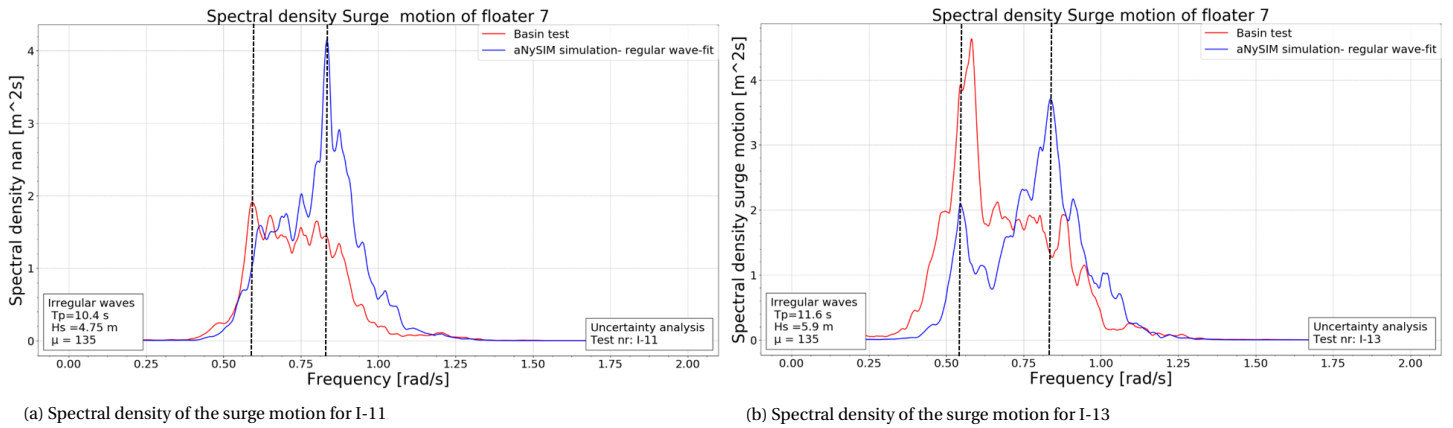


Figure 5.5: Spectral densities of irregular wave test I-11 and I-13, showing the difference in simulation accuracy at the wave exciting ( $\omega_p$ ) and natural  $\omega_n$  frequency, both indicated with a dashed black line.

wave angle between I-11 and I-14. Related to this incoming wave angle is a different direction of overflowing water. Analysing figure 5.8, which shows the level of overflowing water for I-11, an increase in overflowing water (depicted with the green circle) does not result in different behaviour for the sway motion in figure 5.6a. Therefore, it can be concluded that the level of overflowing water is not directly related to the phase shift.

An interesting note can be made regarding this phase difference in comparison to the regular wave tests. Figure 5.1 has shown a phase difference between the basin test results and the simulation model as well, for the longer regular wave tests (R-58, T = 10s). However, this phase shift is negative. Similar to the regular waves, more research is required into the cause of this phase shift.

For test I-14, no phase difference is present, but the sway motion shows an extra oscillating behaviour as compared to the basin tests (designated with a green circle in figure 5.6b). An explanation for these higher order oscillations can be found in the spectral density analysis of irregular wave test I-14, that shows similar characteristics to the surge motion spectral density of test I-13 (see figure 5.5b). The overestimation of the simulation model at the natural frequency peak of the system causes a larger response in motion if this frequency is excited. This causes the extra oscillating behaviour in the green circle.

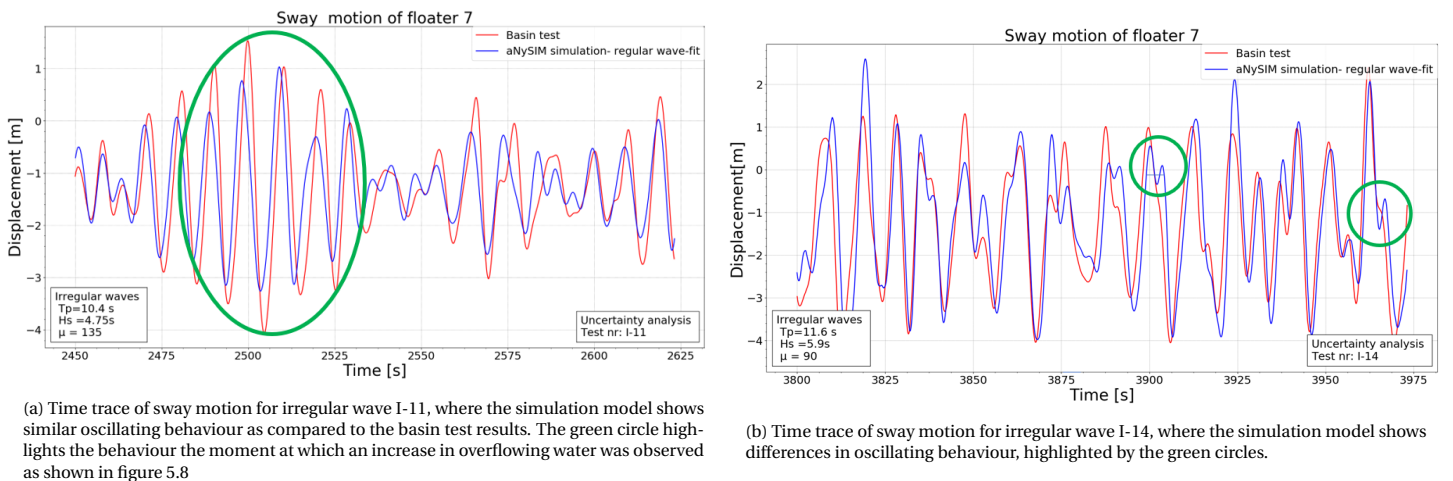


Figure 5.6: Examples of oscillation accuracy for different irregular wave tests. The green circles highlight differences in oscillation behaviour for irregular wave test I-14.

### Oscillating behaviour: roll and pitch

The general oscillation accuracy for roll and pitch is accurate for the irregular wave tests up until a wave height of 3.75 metres. This behaviour substantiates the finding for the roll motion in regular waves (section 5.2.4) that viscous effects are not significant for the roll motion of this design. In higher waves, the oscillation accuracy becomes less as the simulation model starts showing different behaviour at some moments in time.

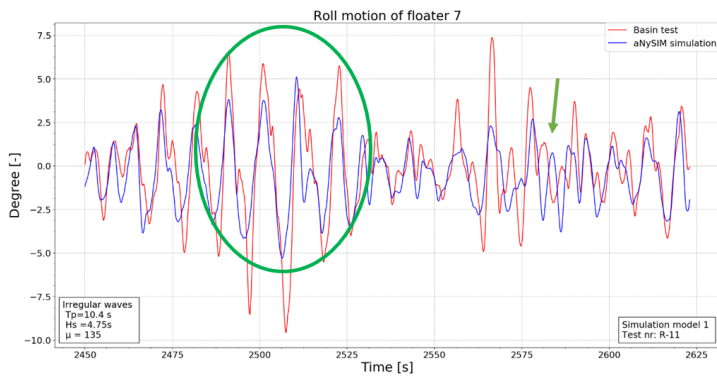


Figure 5.7: Roll motion of floater 7 in irregular wave I-11. Different behaviour can be observed for the simulation model compared to the basin test results. The green circle highlights the behaviour the moment at which an increase in overflowing water was observed as shown in figure 5.8.

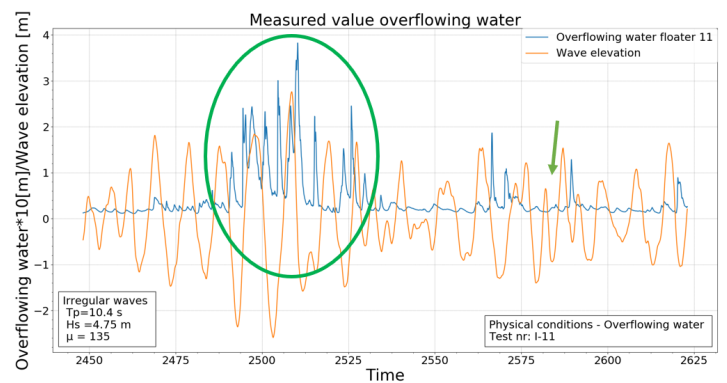


Figure 5.8: The time traces of the measured water height on floater 11 for irregular wave I-11. The green circle highlights an increase in overflowing water. The green arrow highlights a lower level of overflowing water

An example of this behaviour is presented in figure 5.7 for the roll motion in irregular wave test I-11. Specific points are indicated with a green circle and arrow:

*The green circle:* An increase in overflowing water can be observed for a longer moment in time in figure 5.8. In the analysis in section 2.2.2 it was observed that this water flows into multiple directions on the floater (caused by the oblique incoming waves). Figure 5.7 shows that at that moment in time, the oscillating behaviour for the simulation model shows a similar trend to the basin test results, implying that no significant nonlinear behaviour occurs due to the effect of the overflowing water. It can therefore be concluded that the roll motion is not significantly influenced by the overflowing water, contrary to the expectations.

*The green arrow:* The simulation model shows significant difference in oscillating behaviour as compared to the basin test results (a shift in phase and a different oscillating period). Observing the overflowing water measurements at the green arrow, no increase in level is shown. This means that the difference in behaviour cannot be related to the overflowing water effects.

### Behaviour of irregular wave test I-13

As was observed in table 5.5, the oscillation accuracy of the simulation model decreases for all 6 DOF for irregular wave test I-13. Additionally, in the data outlier analysis in section 4.4.1 it was pointed out that the maximum mooring line forces in the basin test results are related to breaking wave incidents. To study if these incidents influence the behaviour significantly, the heave motion is analysed for a given point in time in which a wave breaking incident occurs. Figure 5.9a shows a time trace of the heave behaviour of floater 7 for irregular wave test I-13. As can be seen, the wave height increases around 3840 seconds, at which a breaking wave incident occurs. This increase in wave height causes an increase in overflowing water (also depicted in the figure, showing an increase at 3840 seconds). For that moment in time, the basin test results of the heave motion show large amplitudes, whereas the aNySIM results remain smaller. Additionally, the roll motion is shown for the same breaking wave incident in figure 5.9b. As can be seen, a large roll motion amplitude occurs in the basin test results that is not observed for the simulation model. Both time traces for heave and roll show large inaccuracies in oscillating behaviour that can be partially related to the *nonlinear effects at the breaking wave incident* and the related wave height and overflowing water.

## 5.4. Conclusion

Section 5.2 and 5.3 have pointed out several causes and the corresponding physical origin resulting in model structure uncertainty. These uncertainties were linked to specific design aspects of this system by using the physical analysis of section 2.2.2. An overview is presented in table 5.8. As shown, effects have been identified from three important design characteristics: the multi-body system, the mooring system and the relatively small dimensions. Additionally, the uncertainties influence different degrees of freedom. For instance, the viscous damping effects are identified for the surge and sway motions mostly (shielding effects, coupled pitch-surge motion, mooring line hydrodynamics). Several points of discussion must be made regarding the findings in this chapter.

- Several inaccuracies have been identified for which no direct cause was found. However, analysis has

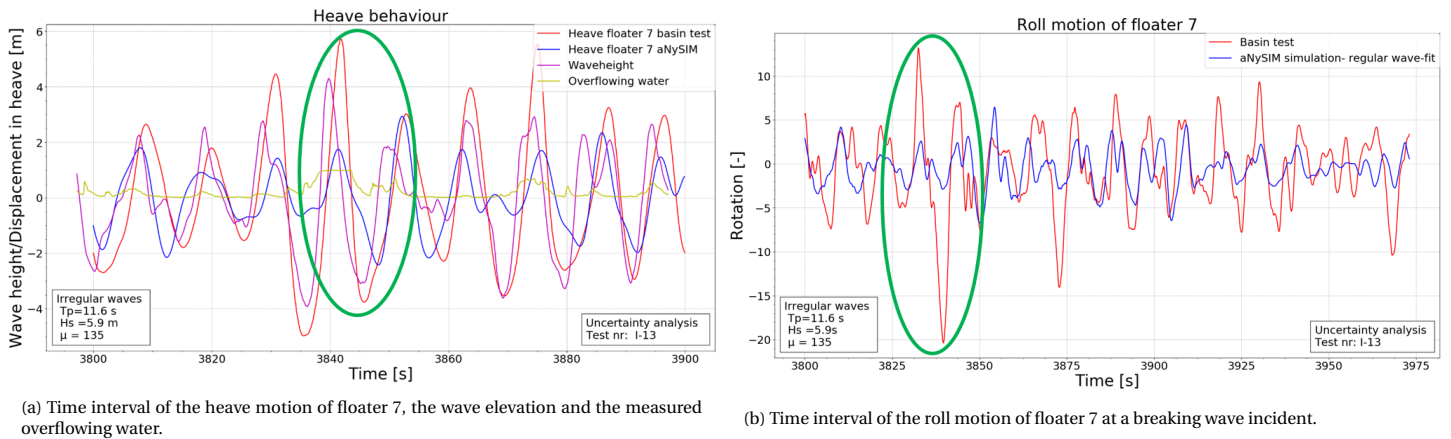


Figure 5.9: Roll and heave results for irregular wave test I-13. The green circle indicates a breaking wave incident.

Table 5.8: Overview of the character of the uncertainties that have been identified by analysing the accuracy of the simulation model and the physical conditions during the test. The design aspect related to the uncertainty is mentioned.

Uncertainty cause	Design aspect	Implementation possibility	Main effect	Governing force
Shielding effects in drag caused by the presence of other floaters	Multi-body system	Yes	Surge/Sway	Damping
Hydrodynamic loads on mooring lines	Moored system	Yes	Surge/Sway/Heave	Damping/Inertia
Coupled pitch-surge viscous damping due to wave steepness effects	Small dimensions	Yes	Surge	Damping
Nonlinear behaviour due to breaking waves	Small dimensions	No	all 6 DOF	Inertia /Damping/Spring
Nonlinear effects in hydrodynamic and static coefficients due to wave following behaviour	Small dimensions	No	Heave/Roll/Pitch	Inertia /Damping/Spring

shown that the causes do not (solely) originate in viscous damping effects. The inaccuracies are:

- The overestimation of surge and sway motion in oblique irregular waves.
- The underestimation of the surge and sway motion for longer irregular waves.
- More research is required to isolate possible uncertainty causes. This requires more data from basin tests results using different test characteristics (systematically altering wave height, period, angle).
- The viscous damping effects that have been identified are not quantified or isolated using measurement data. More research on these effects is required to better determine their significance.
- Contrary to the expectations, the effect of overflowing water has not been identified as a large cause of uncertainty in the surge, sway, roll and pitch motion. This is beneficial for future possibilities of simulations.

The uncertainty causes that influence the viscous damping can be implemented in aNySIM relatively simple and an accurate implementation is expected to have impact on the parameter uncertainty as well. Therefore, for further analysis, it was decided to perform a sensitivity study on the effect of hydrodynamic loads on mooring lines, shielding effects in drag and a coupled viscous damping on the behaviour of the system.

# 6

## Sensitivity studies

Following from the conclusion of the uncertainty analysis, the three parameters have been selected for further investigation in a sensitivity study; the effect of mooring line dynamics, shielding and coupled viscous damping on the system behaviour and mooring line forces.

The goal of this chapter is to get insight in the effect of implementing these parameters on the system behaviour, related to research question 5 as introduced in chapter 1. The first section presents the applied methods used to implement the parameters. Thereafter, results are shown that give a first insight in the sensitivity of all 3 parameters separately and finally a conclusion is drawn on the effect of the parameters.

### 6.1. Method

For each of the three parameters (hydrodynamic mooring lines, the shielding of floaters and coupled viscous pitch-surge damping), the method and assumptions are presented here. All three parameters affect the damping of the system and therefore the floater damping coefficients were re-fitted to obtain agreement with the basin tests. This is necessary to perform a sensitivity study. The 'regular wave-fit' method, explained in section 4.3.1, was used for this re-fit. A clear note must be made on the determination of the parameters; they serve to identify the influence of that parameter on the system; their values are not optimised. Furthermore, only 1 set of parameter values has been tested to see the effect. A more comprehensive sensitivity study was outside the scope of this study.

#### 6.1.1. Hydrodynamic mooring line implementation

The implementation of hydrodynamic effects on the mooring line can be presented by the application of a Morison structure [25] on the line. The Morison structure then applies the Morison equation which is set up as follows:

$$f_m = f_f + f_a + f_d \quad (6.1)$$

where the total Morison force  $f_m$  is a summation of the Froude Krylov force  $f_f$ , added mass force  $f_a$  and the drag force  $f_d$ . For the computation of these forces, an inertia vector ( $c_m$ ) and a drag coefficient vector ( $c_d$ ) need to be defined, both containing normal and tangent coefficients. For this parameter study, it has been decided to select values estimated from literature as a starting point. Research conducted by Yang [46], where the drag coefficient  $c_d$  has been determined based on experiments for a catenary mooring set up, states that for free oscillations the added mass coefficient ( $c_m$ ) does not have a significant influence on the behaviour of a moored structure. Similarly to that research, the value of  $c_m$  has been set on 1 in this mooring line set up. The research further shows drag coefficients for different Reynolds numbers, which converges to a value of 1.5 for high Reynolds numbers. This value has been adopted as well for this mooring line set up. Tangential coefficients are assumed to be an order of magnitude smaller than the normal coefficients and are set on a value of 0.1 for both  $c_m$  and  $c_d$ [46].

The Lumped Mass Line[22] option in aNySIM provides the implementation of a Morison structure on the mooring line. The Lumped Mass Line is split into multiple elements, where the mass and buoyancy of the lines is split into the nodes between the elements. Nodes can be connected by spring stiffness and damping, which serve to implement the stiffness of the mooring line.

The drag load  $f_d$  (tangential and normal) is calculated for each element, taking into account the length and diameter of the element. Similarly, the added mass  $f_a$  is calculated for each element, taking into account the volume of the element and the water density. The Froude Krylov  $f_f$  force is calculated using the wave accelerations at the centre of the element. All three contributions are then split and divided over the connecting nodes.

To solve the entire equation of motion, including the hydrodynamic forces on the mooring line, the integration scheme of the numerical solver must be adjusted. This was done by adjusting the time step of the mooring line within the time step of the entire model, ensuring a stable integration without significantly increasing the total computational time. A study on the required number of elements in the line and the required step size is shown in appendix E.4. An overview of this new mooring line implementation is given in appendix C.5.

### Verification

To verify the new mooring line implementation, benchmark tests from the aNySIM documentation have been used [43]. These benchmark tests serve to verify implementations in the XMF file, where simplified problems have been used. For this specific mooring line implementation, the drag load implementation was verified by applying a regular wave on a simple line connected to a spring object. The offset of the object should match the current drag load, based on the normal and tangential component ( $c_{dn}, c_{dt}$ ). A similar approach was used for the inertia forces (Froude Krylov and added mass), based on the normal and tangential inertia component ( $c_{mn}, c_{mt}$ ). The results are in agreement with the analytical solution of these forces, and therefore this implementation has been used for this study as well.

### 6.1.2. Shielding effect

The shielding effect explained in chapter 5 can be implemented by adjusting the drag coefficients for all floaters dependent on angle of attack of the flow. Previous research done on arrays of cylinders [37] and squares [17, 18] shows that the drag coefficient is influenced by the angle of attack, the distance between the objects, the Reynolds number and the hysteresis (ie. Previous behaviour determines the flow around the objects, implying a time dependent drag). These studies have been conducted for tests with a constant incoming flow and generally larger distances between the objects. Differences with this study are that the current system is not exposed to a constant incoming flow but to incoming (and diffracted and radiated) waves. This means that not only drag but also wave exciting and radiation forces experience shielding effects. The latter is taken into account in the diffraction calculations done in DIFFRAC. Additionally, the current system has very small distances between the floaters, that are much smaller than the length of the floaters. Due to these differences, no exact value can be obtained from the consulted references [17, 18, 37], and literature will only serve as input for the estimations. Literature results show a decrease in drag coefficient from 50% to almost 100% for shielded objects, where the drag decreases when the distance between two objects decreases. For this research, the shielded factor will be set on 25%. This is done since it is expected that due to the small draft, the shielded floaters will still be partly exposed to the incoming waves.

Figure 6.1 shows an overview of the floaters and their applied drag coefficient label for different wave angles of attack. The floaters are divided into rows and columns that are either:

- Exposed to the undisturbed incoming waves completely shielded from the flow from a the wave with 180° difference
- Shielded from both the incoming wave as the wave with 180° difference
- Shielded from the flow from the incoming wave and exposed to the flow from the wave with 180° difference

The colour of the floater indicates the shielding effect for waves with an angle of 180 or 0 degrees. The colour of the number indicates the shielding effect for waves with an angle of 90 or 270 degrees. As can be seen, row 2 and 3 have the same shielding effect for each column. This means that there is no extra shielding applied if a floater is shielded by 2 floaters. Column 1 and 3 have the same shielding effect for exactly the opposite waves, similar to row 1 and 4. As an example, the shielding coefficient is given for floater 1 and floater 10 and 11 in table 6.1, where the latter two have the same shielding effect in both head as beam waves. For floater 1, shielding is assumed for waves from 0 to 90 degrees. Thereafter, the waves are undisturbed. For floater 10 and 11, the flow is undisturbed for waves from 0 to 80 degrees and from 280 degrees onwards. For other flow directions the floaters are shielded from the waves due to the presence of the system. The shielding implementation for all floaters is shown in appendix G.5

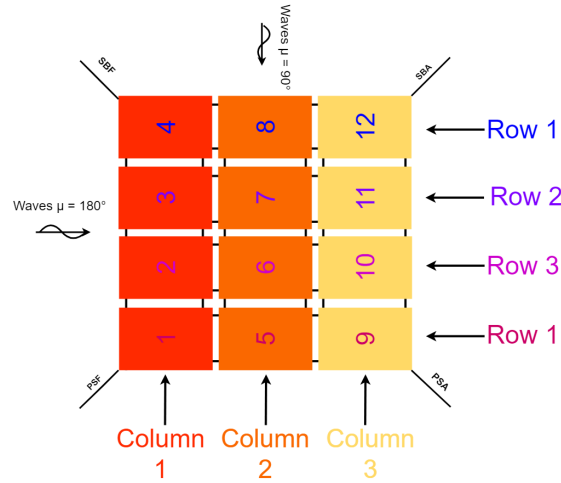


Figure 6.1: Visualisation of the shielding effect per floater, which is dependent on the row and column.

Similar to the drag determination in section 4.3.1, the drag is set equal for surge and sway direction at a value of  $C_d = 1$ . This value is now multiplied by the shielding effect (25% of the drag coefficient) for all flow directions. As a result, 9 different floater files have been created, to accommodate all different drag coefficients.

### Verification

To verify if the shielding effect was implemented correctly, the drag force of this parameter implementation has been compared with the drag force of the 'regular wave-fit' method. The comparison is shown in figure 6.2 for floater 1 and 5, where regular wave R-51 (T7.05H1.5μ180) is used to visualise the effect of shielding on the drag force. Figure 6.2a shows the effect on floater 1. As can be seen, the drag force for the shielding implementation and the 'regular wave-fit' method is equal for a negative relative flow (this means the flow travels in negative x-direction, and floater 1 is the first floater it encounters.), which results in a negative drag force. However, for a positive relative flow (positive drag force), the amplitude of the shielding implementation is around 25% of the drag force amplitude of the 'regular wave-fit' method. This means that floater 1 is indeed shielded by other floaters for a flow in positive x-direction. This is in agreement with the setup as shown in figure 6.1, where floater 1 is shielded from flow travelling in positive x-direction ( $\mu = 0$ ).

Figure 6.2b shows the effect on floater 5. The drag force amplitude of parameter 2 is now 25% of the regular wave-fit method for both positive as negative drag. This means the floater is indeed shielded for both flow directions. This is in agreement with the setup shown in figure 6.1, where floater 5 is shielded from both sides.

### 6.1.3. Coupled pitch-surge damping

Applying a coupled pitch-surge viscous damping connects the pitch motion that increases in steeper waves to the surge motion of the floaters. This coupled damping can be annotated as  $B_{15}$  and can be directly implemented on the floaters in the aNySIM model. However, no experimental data can be used to retrieve this damping value since it cannot be isolated from other damping effects. Furthermore, no literature research has been found on this aspect. Therefore, to do a parameter study on the effect of this damping, the damping value will be estimated and set to a large value. This might result in a strong overestimation of the effect, but it will give insight in possible changes of behaviour of the system.

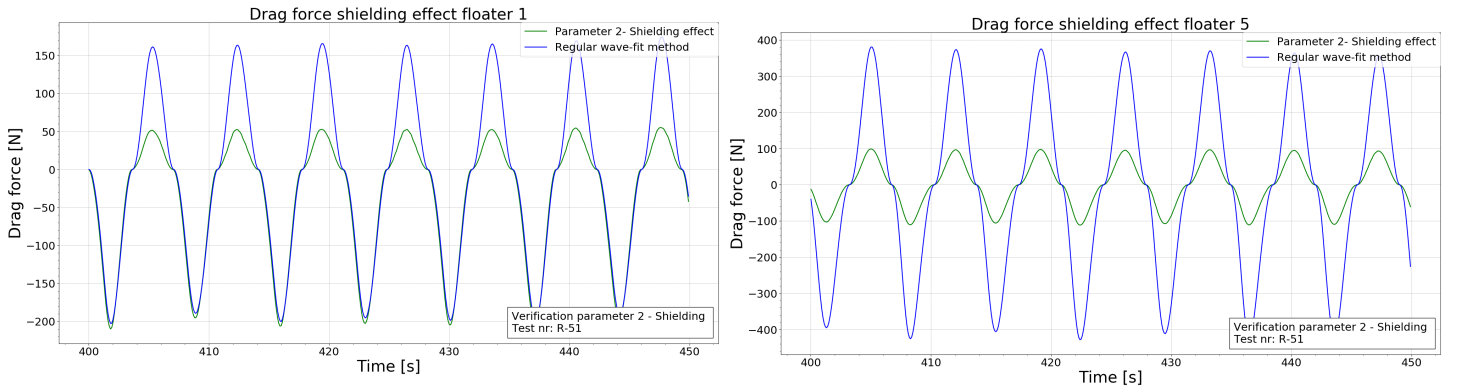
Therefore, to determine the value, the force exerted by this damping value has been set to be 50% of the first order wave exciting force (Froude Krylov) in surge direction. The damping force exerted is calculated by:

$$F_{damp15} = B_{15} \dot{u}_5 \quad (6.2)$$

Where  $\dot{u}_5$  is the maximum pitch velocity of a floater and  $B_{15}$  is the coupled pitch-surge viscous damping. Both values of the Froude Krylov force and pitch velocity are obtained from the results of the 'regular wave-fit' model for regular wave run R-52 (This is the steepest regular wave, having the highest pitch velocity). Results of this calculation are shown in table 6.2.

Table 6.1: Overview of the shielding coefficients for floater 1 and floater 10 and 11. The latter two have the same shielding coefficient for all wave angles.

Angle	Floater 1	Floater 10 & 11	Angle	Floater 1	Floater 10 & 11
0	0.25	1	180	1	0.25
10	0.25	1	190	1	0.25
20	0.25	1	200	1	0.25
30	0.25	1	210	1	0.25
40	0.25	1	220	1	0.25
50	0.25	1	230	1	0.25
60	0.25	1	240	1	0.25
70	0.25	1	250	1	0.25
80	0.25	1	260	1	0.25
90	0.25	0.25	270	1	0.25
100	1	0.25	280	1	1
110	1	0.25	290	1	1
120	1	0.25	300	1	1
130	1	0.25	310	1	1
140	1	0.25	320	1	1
150	1	0.25	330	1	1
160	1	0.25	340	1	1
170	1	0.25	350	1	1



(a) Drag force in surge direction for floater 1. The positive drag force, obtained from a flow in positive x-direction, for parameter 2 is 25% of the drag force for the 'regular wave-fit' model. This is the effect of shielding. For a flow in negative x-direction, the drag forces are equal since floater 1 is not shielded for that case.

(b) Drag force in surge direction for floater 5. The drag force of parameter 2 has an amplitude that is 25% of the drag force for the 'regular wave-fit' method, in both directions. This is due to the fact that floater 5 is shielded from both sides in x-directions.

Figure 6.2: Motion RAO for surge and sway of floater 1. All regular wave test results are shown for parameter 1, 2 and 3, together with the results the 'regular wave-fit' model and the basin tests.

Table 6.2: Overview of values used for the calculation of the damping coefficient for the coupled pitch-surge damping. The assumption is made that the force exerted by this damping is around 25% of the first order wave force exerted on the floater in surge direction.

$\max F_{ex1}$ [N]	$\max F_{damp15}$ [N]	$\max \dot{u}_5$ [rad/s]	$B_{15}$ [Ns]
4041.64	1010.41	0.067	30094.76

Results will be generated with a damping value  $B_{15}$  of 30000 Ns.

### Verification

To verify the implementation of the coupled pitch-surge damping, the linear damping in surge direction is calculated analytically and compared with the results from aNySIM for parameter 3. The linear surge damping consists of the pure surge damping and the coupled damping, which can be written as:

$$F_{vlin} = B_{11}^{(1)} \cdot \dot{x}_1 + B_{15}^{(1)} \cdot \dot{\theta}_1 \quad (6.3)$$

Where  $F_{vlin}$  is the linear viscous force in surge direction,  $B_{11}$  is the linear damping coefficient in surge due to the motion in surge.  $\dot{x}_1$  is the surge velocity of floater 1,  $B_{15}$  is the linear damping coefficient in surge due to the motion in pitch and  $\dot{\theta}_1$  is the pitch velocity of floater 1. The velocities in surge and pitch are obtained from the aNySIM results, calculating the derivative of the motions. Figure 6.3 gives results from the analytically calculated damping force and the linear viscous force obtained from aNySIM. The two methods give the same results, verifying that the implementation of parameter 3 was done correctly.

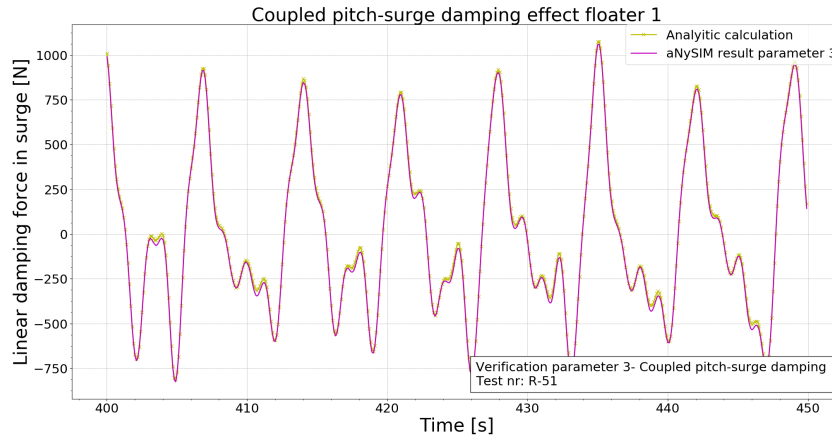


Figure 6.3: The linear damping force in surge, built up by the surge-surge and pitch-surge damping. Analytic and aNySIM results are equal.

## 6.2. Results

To analyse the effect of the 3 implemented parameters, the effect of the implementations compared to results of the 'regular wave-fit' model as presented in chapter 4. First, the behaviour in sway and surge will be discussed for regular and irregular waves. All regular wave results presented are shown in figure 6.4 and all irregular wave results are shown in figure 6.5. Secondly the impact on the mooring line forces will be discussed. Thereafter, decay test results will be presented. To clarify different effects, results have been grouped according to the index as explained in chapter 2. For convenience this index will be repeated here:

- Regular waves

- *Head waves - Test R-50, R-51, R-52*

These tests serve mainly to analyse the behaviour of the system in surge, with wave periods near the natural frequency of the system in surge direction.

- *Beam waves - Test R-53, R54, R-55*

These tests serve mainly to analyse the behaviour of the system in sway direction, with wave periods near (but somewhat lower than) the natural frequency of the system in sway direction.

- *Oblique waves - Test R-56, R-57, R-58*

These tests have an incoming wave angle of 170 deg and increasing wave periods. The tests mainly serve to analyse the behaviour of the system in longer waves, where the small wave angle causes some effects in both surge and sway and therefore a higher system rotation.

- Irregular waves

- *Serviceability limit state (SLS) – Tests I-3, I-4, I-5 and I-6*

These tests have the same wave height (2m) and wave period (6.8s) with incoming wave angles of 180, 135, 105 and 90 degrees. The effect of an altering wave angle can be analysed with these tests. Furthermore, due to their close similarity to the regular waves, the effect of irregular wave behaviour can be observed.

- *Bridging states, beam waves – Tests I-8, I-10, I-12, I-14*

The bridging state tests have an increasing wave height and wavelength and serve to analyse the effect of these increasing sea states. Four increasing sea states are tested for beam waves ( $\mu =$

90°). These tests allow for an analysis of the system with a dominating sway motion, where surge motions can be neglected.

– *Bridging state, oblique waves – Tests I-7, I-9, I-11, I-13,*

The bridging state tests have an increasing wave height and wavelength and serve to analyse the effect of these increasing sea states. Four increasing sea states are in oblique waves ( $\mu = 135^\circ$ ). These tests allow for analysis of the system where both surge and sway motions are present, and the system experiences more yaw rotation.

### 6.2.1. Parameter 1 - Hydrodynamic mooring line implementation

The implementation of parameter 1 results in increased motions as compared to the 'regular wave-fit' model for tests with shorter wave periods (higher frequencies) than the natural frequencies of the system. This effect can be observed in figure 6.4a, where RAO of the surge motion in regular waves is shown: The RAO in head waves (R-50, and R-52) increases for parameter 1 as compared to the results of the 'regular wave-fit' model (note that the RAO for R-51 is equal to the 'regular wave fit' model since this test was used to re-fit the damping coefficients). Similarly, the effect can be observed in SLS test I-3 as shown in 6.5a, where the spectral density of parameter 1 is higher than for the 'regular wave-fit' model. This higher spectral density does not improve the agreement of the simulation model with the system.

Observing tests with longer wave periods, the implementation of parameter 1 gives lower results as compared to the 'regular wave-fit' model. This can be observed in the oblique regular waves (R-56, R-57 and R-58) in figure 6.4a, where the surge RAO for parameter 1 clearly decreases as compared to the RAO of the 'regular wave-fit' model. A similar effect can be observed for the oblique bridging irregular wave tests, see figure 6.5b, where the spectral density of the surge motion of irregular wave I-11 is shown for all three parameters and the 'regular wave-fit' model. Parameter 1 clearly shows a decrease in spectral density; the spectral density of parameter 1 is lower than the 'regular wave-fit' method for the lower frequencies.

For sway, a similar effect can be observed, although to a lesser extent. This is shown in figure 6.5c, where the spectral density of the sway motion for oblique wave test I-13 is shown. Similar to the spectral density of the surge motion for that test (figure 6.5b), the spectral density of parameter 1 is lower than the spectral density of the 'regular wave-fit' model.

The results for the sway RAO in regular beam waves (figure 6.4b, test R-53, R-54 and R-55) show a small increase in RAO for parameter 1 as compared to the 'regular wave-fit' model. These tests have a shorter wave period than the natural period of the system in sway, which is similar to the effect that was observed for the regular wave results in surge.

### 6.2.2. Parameter 2 - Shielding effect implementation

The shielding effect is insignificant for the regular wave test RAO's (see figure 6.4a for the surge RAO and 6.4b for the sway RAO), where no change in RAO's can be observed for parameter 2 as compared to the 'regular wave fit' model. This insignificant effect can be explained by the fact that due to the small differences in the sea states of the regular waves (all waves are relatively long) the (possible) shielding effect is similar for all tests. Similarly, no effect can be observed for the SLS tests in head and beam waves (see figure 6.5a where the results of parameter 2 overlap the results of the 'regular wave-fit' model).

The shielding effect becomes most visible for tests in the bridging state, as can be seen in the spectral density of the sway motion for test I-11 (figure 6.5c). The effect is smaller in surge direction, as shown in 6.5b), where no clear difference can be observed in spectral density for the results of the 'regular wave-fit' model as compared to parameter 2. An explanation for this difference can be found in the setup of the floater system. For the shielding effect in surge direction, three different floater columns can be observed, whereas for the shielding effect in sway direction, 4 rows are observed. This causes more difference in drag on the floaters in sway compared to the original 'regular wave-fit' model, and therefore this effect was expected.

### 6.2.3. Parameter 3 - Coupled pitch-surge damping implementation

As expected, this implementation mostly has influence on the behaviour in surge direction and can be observed for different wave lengths. This effect can also be observed in bridging test I-9 (see figure 6.5d), where two peaks can be identified in the spectral density of the surge motion for all simulation models. The first peak (at  $\omega = 0.68$  rad/s) corresponds to the peak frequency of the incoming wave spectrum. At this peak, the spectral density of parameter 3 has increased as compared to the 'regular wave-fit' model. For the second peak (at  $\omega = 0.86$  rad/s), which corresponds to the natural frequency of the system, the spectral density of

parameter 3 stays equal to the 'regular wave-fit' results.

At the first peak, the corresponding waves are longer (similar to the oblique regular waves) than in the second case. These longer waves can be related to a lower pitch velocity; the resulting coupled damping is lower and therefore the behaviour increases. A similar effect can be observed for I-11 (see figure 6.5b), where a decrease in spectral density is observed for the lower frequencies and around the natural frequency of the system. Parameter 3 shows similar results to the results of the 'regular wave-fit' model.

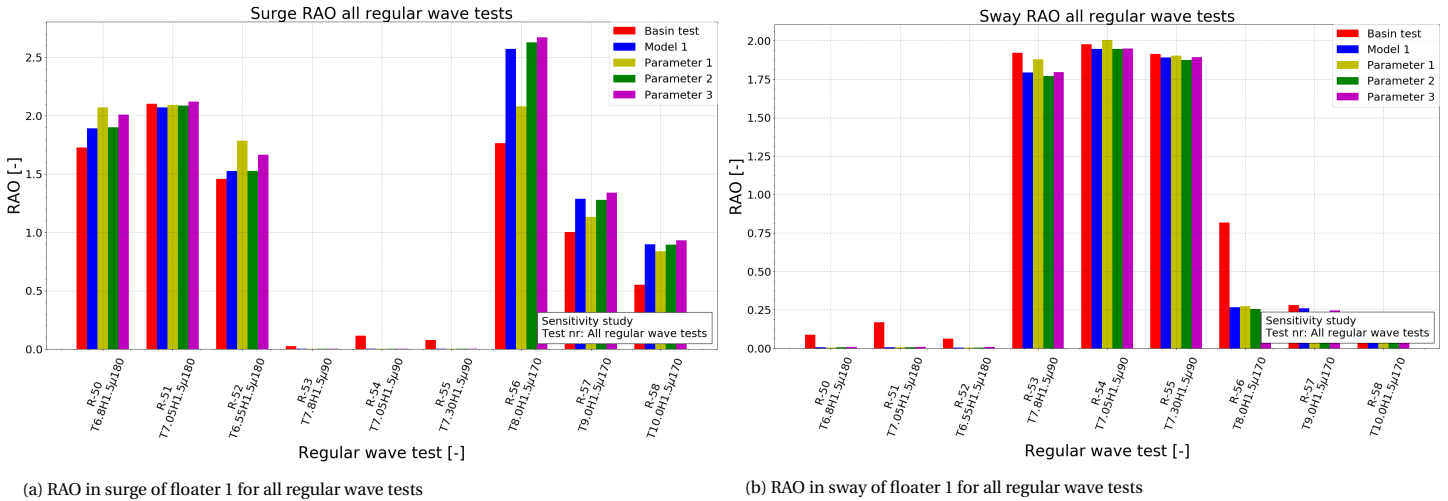


Figure 6.4: Motion RAO for surge and sway of floater 1. All regular wave test results are shown for parameter 1, 2 and 3, together with the results the 'regular wave-fit' model and the basin tests.

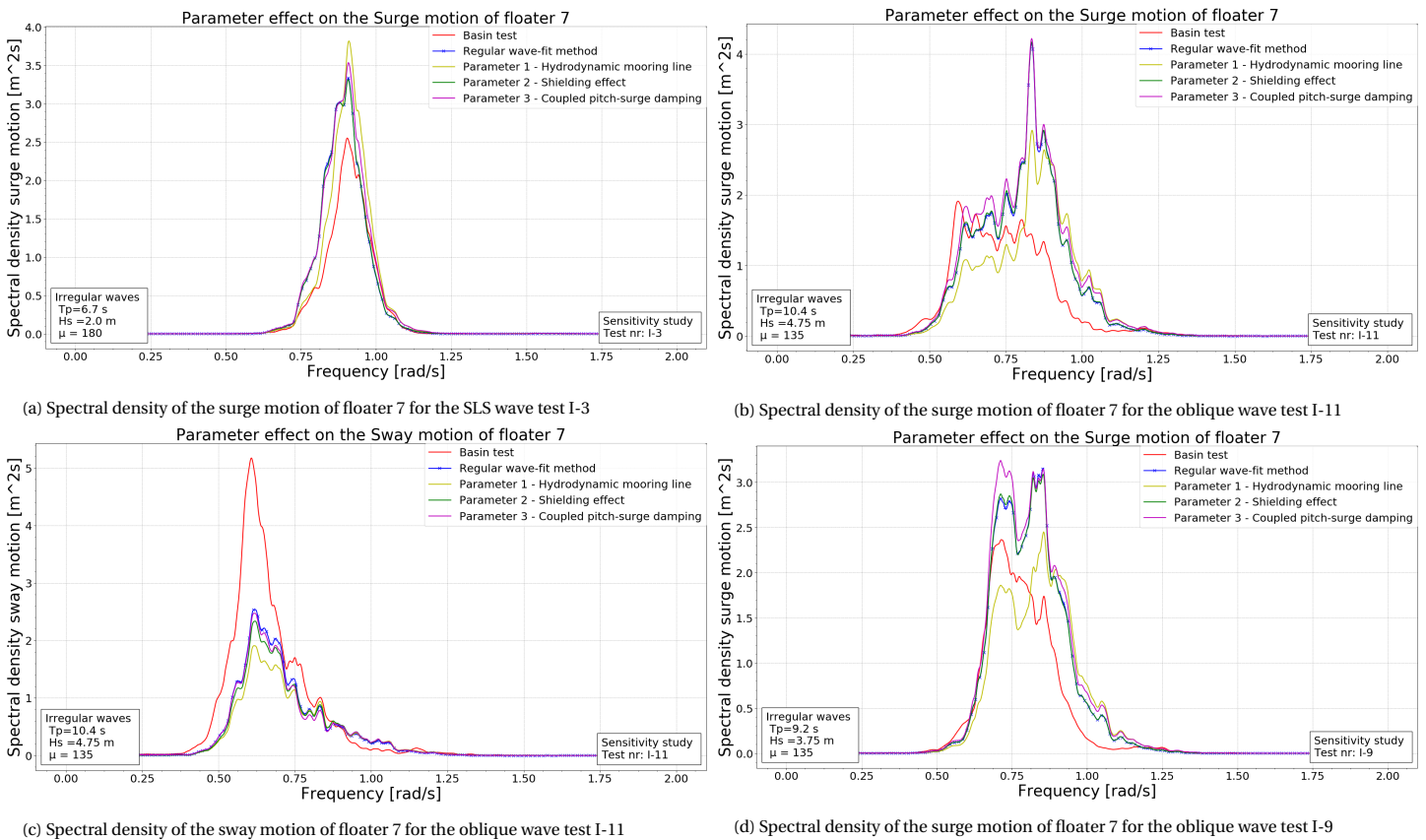


Figure 6.5: Spectral densities of the surge and sway motions of floater 7 for all three parameters, the 'regular wave-fit' model and the basin test results. Different irregular wave tests are shown to perform the sensitivity analysis

### 6.2.4. Mooring line forces in irregular waves

The effects mentioned above are explained and shown for the surge and sway motion of the system. However, the effect on the mooring line forces is determined by the behaviour of the system in all 6DOF. The forces in the mooring lines are therefore elaborated on in this section. Most effects can be observed in the oblique irregular waves, therefore the spectral densities of all four mooring line forces are shown for test I-11 in figure 6.6.

Looking at all four sub figures, the first observation that can be made is that the effect of the parameter implementations can be split into two groups:

The lines perpendicular to the incoming waves, mooring line PSF (figure 6.6a) and SBA (figure 6.6d) show the same trends for all three parameters; all parameters have a decreased spectral density compared to the regular wave-fit' model.

The lines that are in line with the incoming waves, mooring line PSA (figure 6.6b) and SBF (figure 6.6c) show similar trends; The spectral density of parameter 1 decreases, parameter 2 stays equal and parameter 3 increases as compared to the spectral density of the 'regular wave-fit' model.

Combining the two groups, the following observations can be made for the parameters:

- For parameter 1 (Hydrodynamic forces on the mooring lines), all mooring line forces have decreased. This is in line with the behaviour that was observed for the irregular waves as shown in section 6.2.1. The behaviour remains similar to the 'regular wave-fit' model, with lower amplitudes.
- For parameter 2 (Shielding effect) no effect was observed for the lines perpendicular to the incoming waves. For the mooring line forces parallel to the incoming waves, a decrease in force was observed. The implementation of shielding has resulted in different oscillating behaviour as compared to the regular wave-fit model.
- Parameter 3 (Coupled pitch-surge damping) shows different behaviour for the four mooring lines as compared to the 'regular wave-fit' model as well, where the forces in line with the waves become higher and the forces in the lines perpendicular to the waves become lower.

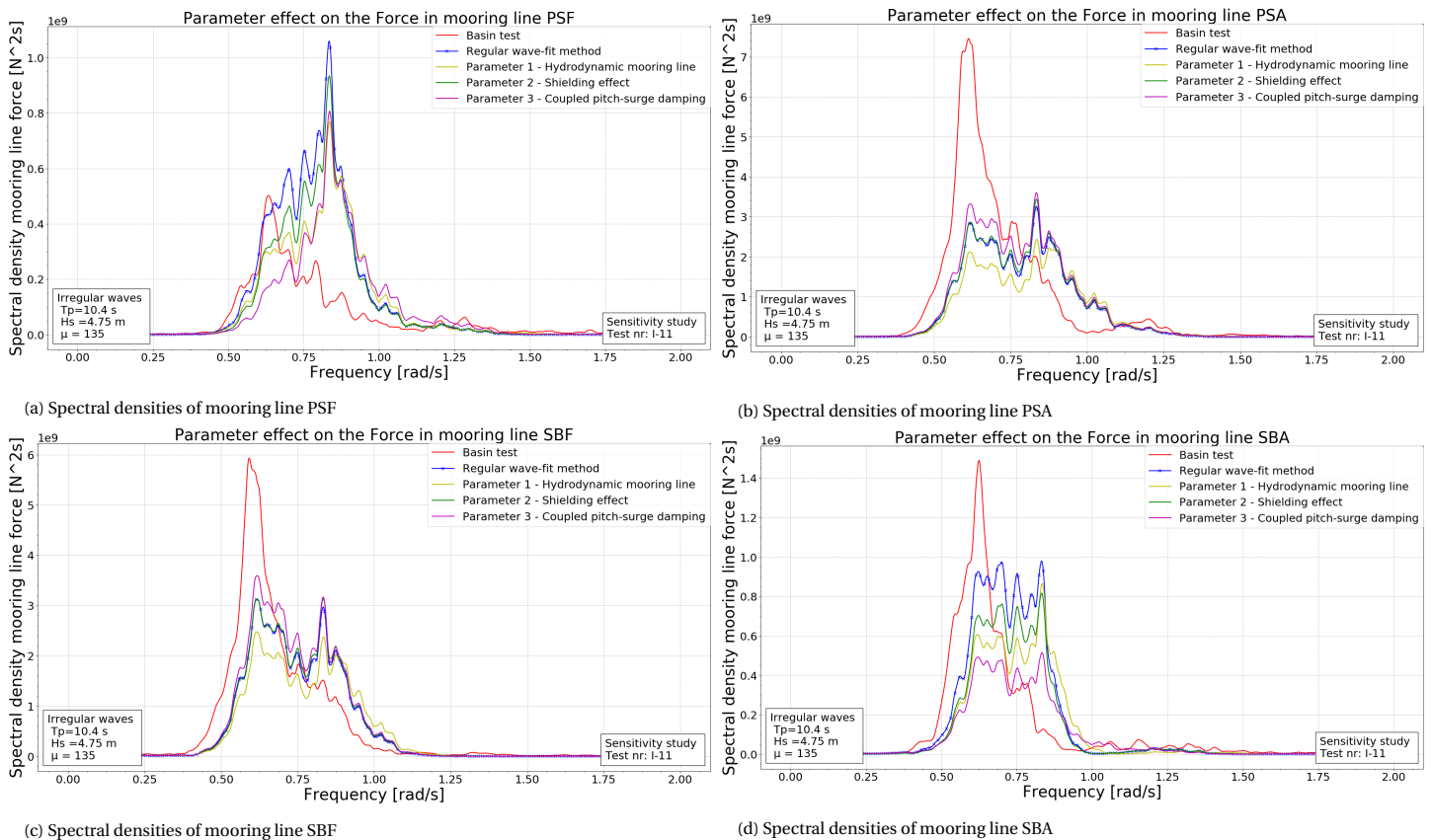


Figure 6.6: Spectral densities of all four mooring lines for all three parameters, the 'regular wave-fit' model and the basin test results.

### 6.2.5. Decay test results

In figure 6.7 the results for the surge and sway decay are presented for all three parameters in combination with the results of the 'regular wave-fit' model and the basin tests.

As can be observed in figure 6.7a, the decay result for parameter 1 shows the most divergent behaviour as compared to the 'regular wave-fit' model, as both the amplitude as the period is different for all oscillations. The difference in period can be a result of the additional added mass in the mooring line. Following from the equation of the natural frequency of the system, a higher added mass would decrease the natural frequency (and therefore the natural period increases):

$$\omega_n = \sqrt{\frac{k}{m+a}} \quad (6.4)$$

Where  $\omega_n$  is the natural frequency,  $k$  is the stiffness of the system,  $m$  is the mass of the system and  $a$  is the added mass of the system. Furthermore, it can be observed that parameter 2 only shows larger motions than the 'regular wave-fit' model for the first oscillation, whereafter the effect is lost. This can be a result of a decreased influence of the drag on the behaviour for smaller oscillations (since drag scales with the velocity squared, the effect is larger for larger velocities). Finally, parameter 3 shows a similar decay period as the 'regular wave-fit' model with lower amplitude, since more damping is present. This is striking, as the pitch velocity is much smaller for the decay tests than in the regular wave tests, thus the coupled damping was expected to have little effect. This would have led to an increase in decaying motion since the damping on the floaters in surge direction is lower.

For the decay motion in sway (see figure 6.7b), a similar effect of parameter 1 can be observed as for the surge decay test. Parameter 2 shows more difference with the 'regular wave-fit' results than for surge; this is in line with the results of regular and irregular waves, where parameter 2 has more effect on the sway motion. Parameter 3 shows no effect on the sway decay motion, which is expected due to the fact that the damping implementation only affects the surge motion.

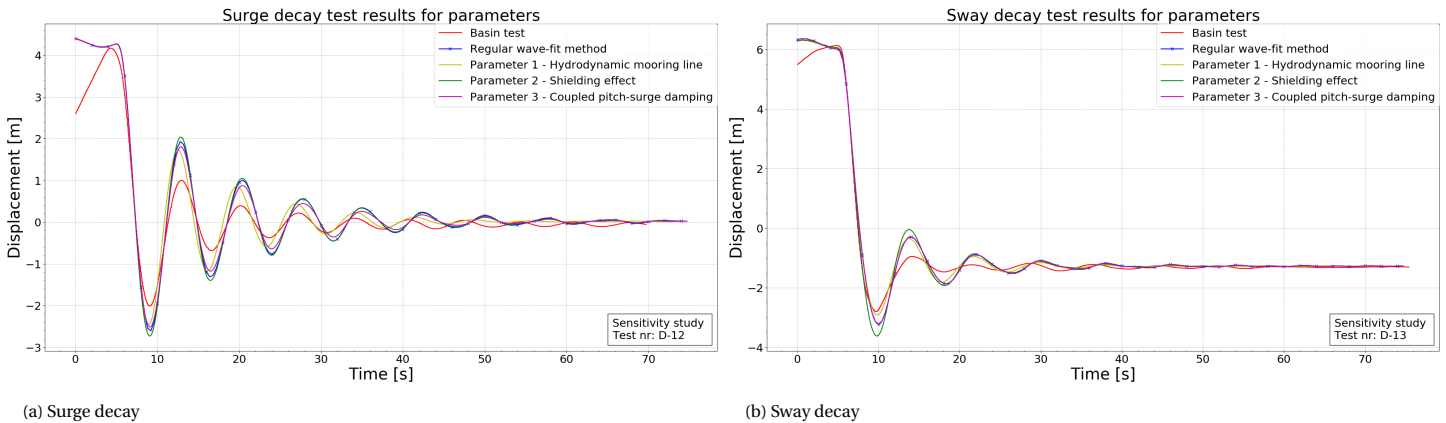


Figure 6.7: Decay tests in surge and sway for all three parameters, the 'regular wave-fit' model and the basin test results.

## 6.3. Conclusion

Several statements can be made on the effect of the three different parameters tested (the effect mooring line dynamics, shielding and coupled viscous damping).

### Hydrodynamic mooring line dynamics

From the analysis in chapter 5, implementing a hydrodynamic loads on the mooring line could improve the behaviour of the system due to better determination of the damping effects. The results from this sensitivity study show that the effect of the implementation is different for SLS tests, where an increase in surge and sway motion is observed as compared to the 'regular wave-fit' model. For the bridging tests, the behaviour decreases as compared to the 'regular wave-fit' model. This trend is similar over the different wave angles. The mooring line dynamics require some more investigation in order to correctly implement them, since results show that their effect is significant.

### **Shielding effect implementation**

As expected from the analysis in chapter 5, the shielding implementation has not influenced the behaviour of the system in regular waves. It was expected that the implementation would become more visible in irregular waves but results show that the effect is negligible; only very small differences could be observed for oblique waves. These small differences resulted in different spectral densities for the mooring line forces that are parallel with the incoming wave.

### **Coupled pitch-surge damping**

The coupled pitch-surge damping was implemented to mainly analyse the effect of different wave steepness on the surge motion. For the regular waves with the highest wave steepness (R-52) the RAO has increased as compared to the regular wave fit. This result is the opposite of what is expected.

The effect is also visible in irregular waves, where the motion increases as compared to the 'regular wave-fit' model around the lower frequencies in the spectrum. This is according to the expectations; at the lower frequencies, the pitch motion becomes smaller, resulting in lower damping. The implementation causes a different effect on the force in the four different mooring lines as compared to the results of the 'regular wave-fit' model. Furthermore, the effect was implemented for the surge damping, but effects were observed in sway as well as for oblique waves, implying a motion coupling.

### **Model improvement**

The current implementation of the three parameters has not led to clear model improvements towards a higher accuracy. The effects are different for different wave tests and different motions and mooring lines. Additionally, due to the presence of different viscous effects in all tests, the combination of all parameters should be tested. For improvement, more research must be conducted, for which the hydrodynamic mooring line has most priority, as is expected that most improvement can be obtained there. Thereafter, the implementation of the coupled pitch-surge damping could give improvements. Finally, it is not expected that the shielding effect for this current implementation will result in significant improvements.

# 7

## Discussion

In this chapter, the research presented in this report is discussed. First, the limitations of this study are discussed in section 7.1. A more general assessment of the findings of this study is discussed in section 7.2. Thereafter, the specific tool used for this study, aNySIM, is discussed as simulation model in section 7.3.

### 7.1. Limitations of this study

#### Mooring line implementation

The simulation model used for this research was not able to correctly simulate the mooring line forces for system offsets larger than 10 metre in the horizontal plane, corresponding to mooring line forces of 480.7kN. This force was not exceeded in the simulated tests, but for simulations of higher sea states, the mooring line implementation must be improved.

#### Ultimate limit state simulations

Following from the mooring line implementation and the physical effects present in the ultimate limit state (ULS) tests, it was decided to leave the ULS tests out of the scope of this research. As a result, no conclusions can be drawn on the accuracy of the model in ULS. The knowledge gap on uncertainty causes and accuracy in ULS remains.

#### Uncertainty analysis

A simplified method was used to identify the accuracy of the system in all 6DOF and all four mooring lines in the uncertainty analysis. This means that small nuances might not have been picked up, or possibly some effects were enlarged. However, by analysing the causes for inaccuracy in more detail, it is expected that the trends that were observed (e.g. overestimation of the simulation model around the natural frequency, underestimation at lower frequencies, discrepancies in oscillating behaviour for higher wave heights) were accurately identified, although some trends might not have been discovered and discussed.

#### Joint forces

The joint forces were outside the scope of this study. Since no extensive research was performed on this subject, it is difficult to discuss the potential effect of an error in the joint stiffness on the system behaviour and mooring line forces. Two following actions must be done to further address this phenomenon:

- It would be necessary to identify the sensitivity of the system regarding the joint stiffness, by altering the stiffness matrix
- It must be studied whether the stiffness matrix from the springs used in the basin tests can be defined more precisely in order to decrease the informational uncertainty.

#### Model accuracy

The accuracy of the simulation model has only been determined in serviceability state and bridging state. Accuracy for ultimate limit state was not analysed and is recommended in further research. It is expected that the accuracy of the system in ULS is lower as external effects increase in higher sea states. Additionally, due to the limited availability of validation, trends that were observed regarding the model accuracy cannot be fully

isolated. More experiments must be conducted to fully conclude to what extent the simulation model is able to accurately simulate the system behaviour.

### Quantification of uncertainties

The uncertainties that have been identified in this study (e.g. viscous effects on the mooring lines, coupled viscous effects or non linearities due to breaking waves) have not been quantified. Therefore, no conclusion can be drawn on the absolute significance of these effects and more research is required. Quantification can be done by more extensive sensitivity studies in aNySIM or by using different numerical tools (e.g. CFD tools to identify specific damping effects).

## 7.2. Interconnected, multi-body offshore floating solar systems

For future designs of OOE or other companies exploring the possibilities of multi-body, low freeboard offshore systems, it is important to address the relevance of this study in a more generic way.

### Damping determination method

As pointed out in the previous section, an additional method for damping determination has been analysed to study the parameter uncertainty using the 'decay-fit' method. A small improvement in accuracy was obtained using the 'regular wave-fit' method compared to the 'decay-fit' method. However, performing experiments in regular waves is more expensive and time consuming. Therefore, the benefits of a small increase in accuracy does not outweigh the extra trouble of required regular wave tests for future designs. A recommendation must be made to further study the effects of a multi-body system in decaying motion. Additionally, the simulation procedure to perform a decay test in yaw must be developed for a multi-body offshore system as no method was found and the results of this decay test simulation were not suitable for the fitting process.

### Upscaling effects

As part of a larger picture, this design forms the basis of development of floating solar fields consisting of 500, 1000 or maybe even 10.000 floaters. Which results would change and which would be expected to remain the same?

#### *Computational time*

A benefit of using the frequency-time domain solvers compared to CFD (which most likely results in higher accuracy) is that the computational time is limited. For the current system, computational time is 2 hours for 1000 seconds of real time simulation in irregular waves. In comparison, a typical CFD calculation for a vessel takes around 50 hours for 1000 seconds[12]. However, increasing the number of floaters would significantly increase the computational time as well, which would cause the same problems as present in CFD (Results take a long time to generate and fast design becomes challenging). This problem could be addressed by re-considering the need for time domain solvers and analyse the possibilities of a combination of frequency and time domain solvers. However, the question must then also be asked if there even is a possibility to simulate a system with a high amount of bodies within a reasonable time range.

#### *Parameter determination capabilities*

For larger structures, the determination of viscous damping might become even more inaccurate since isolating effects becomes increasingly difficult. Furthermore, a simulation software that is dependent on experimental results for damping determination might encounter scaling problems for very large structures if they were to be tested in a physical tank on model scale. A solution could be to look into trends regarding the viscous damping and extrapolate to larger structures.

#### *Effect of model structure uncertainties*

The model structure uncertainties, mentioned in the section above, all have different effects for larger structures. Firstly, it is expected that mooring line dynamics become less relevant for larger structures if the mooring line setup remains similar to this current situation. In that case, the relative force contribution of the mooring lines would decrease as the amount of floaters increase.

Secondly, the shielding effect as explained earlier, is likely to change for larger structures. In larger structures, the floaters at the centre will experience more shielding effects than the floaters in the centre of the system of 12 floaters. In addition, damping of the waves due to the presence of the floaters would become more significant on a larger scale. The flow in the centre of a large scale setup might have changed significantly compared to the incoming flow and thus different damping effects are likely to be present on the floaters.

Thirdly, the coupled pitch-surge damping effect is expected to remain similar for the individual floaters, although the relative contribution to the behaviour might change as the proportion of forces might change.

Finally, the effect of overflowing water is expected to be present for a larger scale, although the possible damping effect that the floaters exert on the waves might influence the amount of overflowing water depending on the location in the field. This would mean that the effect would not only change for different sea states, but also for different floaters within the field.

### **Design alterations**

The system as presented is dependent not only on the amount of floaters, but also on the mooring system and the dimensions.

#### *Mooring system*

Altering the mooring system is likely if the number of floaters increases or for different locations. This could increase or decrease the hydrodynamic effect of the mooring system. However, since incorporating the mooring line hydrodynamic effects increases the computational time, a constant consideration must be made on the significance of the mooring line forces.

#### *Freeboard, draft and weight*

Changing the dimensions of the floater would influence the amount of overflowing water. Furthermore, the effect of the added weight and inertia could change and become more or less relevant for a different structure. Altering the draft might influence the flow disturbance and could change the shielding effect.

#### *Gap distance*

Altering the gap distance between the floaters could introduce gap resonance effects that are not present for this specific design but would significantly influence the behaviour of the structure. Gap resonance effects are both from numerical as physical origin. The numerical gap resonance can be limited using a so called 'surface lid' [3], however, the physical gap resonance can have significant influence as has been studied for larger offshore structures [38].

## **7.3. aNySIM**

Regarding the simulation tool that was used, several comments can be made.

### **DIFFRAC-aNySIM combination**

The simulation tool is build on a combination of the diffraction software DIFFRAC and the time domain solver aNySIM. This combination requires two licences if everything were to be done in-house. This might result in increasing costs compared to other simulation software. Furthermore, the separation between the diffraction software and time domain simulation software increases the possibility of inconsistencies in design parameters if different designs were to be studied.

### **Usability**

The use of aNySIM requires a lot of research, as not all content and possibilities are well documented. On the other hand, the experience that is present at MARIN regarding the use and possibilities of the software is very useful, especially for novel designs.

### **Optimisation possibilities**

The simulation tool aNySIM holds a lot of possibilities that have not been used in this study. Therefore, it cannot be said that the optimal solution has been found. For instance, the Morison equation [26] that has been used for the hydrodynamic loads on the mooring lines, can also be used to add hydrodynamic effects on the floater due to the overflowing water. However, this approach neglects diffraction effects and it is therefore unknown whether results would improve. Additionally, there are undoubtedly more possibilities that have not been discovered in this study.



# Conclusion and recommendations

The main goal of this study was to investigate to what extent the frequency-time domain simulation tool is able to simulate an interconnected, multi-body offshore floating solar system. The main conclusions and recommendations are presented in this chapter.

## 8.1. Conclusion

The frequency-time domain simulation tool is able to simulate regular wave tests and irregular wave tests with low sea states within the reliability limits for engineering purposes. For higher sea states the simulation tool cannot be considered as reliable due to nonlinear effects that cause discrepancies in oscillating behaviour and motion amplitudes.

For the serviceability limit state ( $H_s = 2.0\text{m}$ ,  $T_p = 6.8\text{s}$ ) the simulation model captures the most significant physical phenomena that determine the system behaviour: the simulation model shows accurate oscillating behaviour and errors for the maximum mooring line forces are smaller than 10%.

For higher sea states, errors in the mooring line forces increase towards 15%. The oscillating behaviour accuracy decreases from sea states of  $H_s = 4.75\text{m}$  and  $T_p = 10.4\text{s}$  and higher. Analyses have shown that this difference in oscillating behaviour is not a direct cause of overflowing water effects.

A strong increase in nonlinear effects as breaking waves incidents and large amounts of overflowing water are related to large discrepancies in oscillating behaviour for a sea state of  $H_s = 5.90\text{m}$  and  $T_p = 11.6\text{s}$ . Errors in the mooring line forces are related to these breaking wave incidents, resulting in errors of around 20%.

Inaccuracies causing the mooring line force errors for sea states around the natural frequency of the system are ascribed to viscous damping effects, caused by both parameter uncertainty and model structure uncertainties. The conventional damping determination method 'decay-fit' introduces parameter uncertainty that is caused by the highly damped behaviour in the decay tests. A newly introduced damping determination method using regular waves ('regular wave-fit') has shown an improvement in the mooring line force errors for all irregular wave tests of around 4% as compared to the 'decay-fit' method.

Model structure uncertainties regarding viscous damping have been identified for the (novel) design characteristics of the system (the multi-body system, small dimensions and the mooring system). Additionally, model structure uncertainties have been identified in the linear assumptions of hydrodynamic coefficients calculated in the frequency domain software.

As a result of the test characteristics and the complex combination of physical phenomena that define the behaviour of the system, it is not possible to isolate all causes of inaccuracies in the simulation model. More validation data is necessary to further isolate different effects, specifically in the longer regular and irregular waves.

## 8.2. Recommendations

### Experiments

More experiments are required to isolate effects on the model accuracy. Several tests are recommended specifically:

- Decay tests to get better insight in the physical behaviour that causes the highly damped system.
- Regular sea states at the exact natural frequency of the system to allow for a better comparison between the 'regular wave-fit' method and the 'decay-fit' method.
- Regular sea states in head waves with the same period and wave height as regular wave test R-56, R-57, R-58 (H=2m and T=8s, 9s or 10s) to exclude to incoming wave angle effect from the overestimation in surge direction.
- Irregular wave tests where only the significant wave height or peak period is adjusted, to study the effect of longer waves separately from the effect of higher waves.

### Comparison data

To develop and optimise a simulation model for a novel design, gaining more experience is crucial in addition to the model improvements as suggested in the previous sections. This experience consists of more simulations, more validation material and more comparisons. To do so, it is recommended to actively use all data that is obtained from the real life prototype behaviour. Additionally, ULS tests should be simulated as well. This would allow a better informed judgement regarding the model reliability. Finally, it is recommended to compare the results in this study with the results from van Poppelen [34] (which has used a slightly different design and different validation data) to analyse whether similar trends in accuracy can be observed and whether similarities in viscous damping implementation can be found.

### Viscous damping determination

The decay simulation method in yaw should be researched more extensively provide a suitable method for a multi-body system. Using better data from decay experiments and regular wave tests at the natural frequency of the system, the two damping determination methods must be further studied.

### aNySIM model improvement

The joint implementation in aNySIM must be improved to minimise the uncertainties due to differences in joint stiffness. It is recommended to further optimise and research the implementation of hydrodynamic mooring line effects and coupled pitch-surge damping. Both implementations affect the viscous damping of the system and expectations are that the parameter uncertainty present in decay tests decrease.

### Nonlinear hydrodynamic coefficients

It is recommended to study the effect of non-linearities in the hydrodynamic coefficients due to the small dimensions as compared to the wave height and wave length, to quantify the significance of the wave following behaviour and to see whether these effects are crucial in model reliability. These studies must be done in a different simulation tool.

### Upscaling

Regarding the possibility of upscaling of numbers of floaters, the most limiting factor is expected to be the computational time. It is therefore recommended to study two possibilities: The first possibility is to see whether symmetry in the system can play a role in computation of hydrodynamic forces. For instance, the added mass and damping coefficients now differ for all 12 floaters due to their different location within the system. However, for larger fields of floaters, it might be possible to apply symmetry rules. This would decrease the number of floaters for which diffraction software should be run. This only affects the computational time of the frequency solver.

The second possibility is to study different frequency-time domain solver combinations. This means that more of components of the equation of motion could be calculated in frequency domain in a simplified version. For instance, research could be done on implementing a frequency dependent solution of the mooring line set up instead of a time dependent solution.

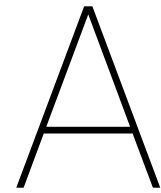
Finally, it is recommended to continuously assess the reliability of the frequency-time domain solver in comparison with the increase of computational time or required research for improvements.

# Bibliography

- [1] E Bellini. Dutch consortium plans world's first "off-shore" floating PV plant for the North Sea. URL <https://www.pv-magazine.com/2018/02/07/dutch-consortium-plans-worlds-first-off-shore-floating-pv-plant-for-the-north-sea/>.
- [2] J Bokhorst and R Zoontjes. Float-Over Analysis for World'S Largest Float-Over Barge. In *International Conference on Ocean, Offshore and Arctic Engineering*, pages 1–8, 2011. ISBN 9780791844359. doi: 10.1115/OMAE2011-49462.
- [3] B Buchner, A van Dijk, and J de Wilde. Numerical Multiple-Body Simulations of Side-by-Side Mooring to an FPSO. *Proceedings of the 11th International Offshore and Polar Engineering Conference*, I:343–353, 2001.
- [4] X Chen, W C Cui, and Q Shen. New method for predicting the motion responses of a flexible joint multi-body floating system to irregular waves. *China Ocean Engineering*, 15(4):491–498, 2001. ISSN 08905487. doi: 10.3321/j.issn:0890-5487.2001.04.004. URL <http://www.cnki.com.cn/Article/CJFDTOTAL-CHIU200104003.htm>.
- [5] L Cheng and P Lin. The numerical modeling of coupled motions of a moored floating body in waves. *Water (Switzerland)*, 10(12), 2018. ISSN 20734441. doi: 10.3390/w10121748.
- [6] C Chrysosostomidis. Mooring dynamics. In *Design of Ocean Systems*. MIT opencourseware, Cambridge, MA, 2011.
- [7] W. Cummins. Impulse response function and ship motions. *Schiffstechnik*, 1962.
- [8] X. Feng and W. Bai. Hydrodynamic analysis of marine multibody systems by a nonlinear coupled model. *Journal of Fluids and Structures*, 70:72–101, 2017. ISSN 10958622. doi: 10.1016/j.jfluidstructs.2017.01.016.
- [9] Y Inoue and MR Islam. Effect of viscous roll damping on drift forces of multi-body floating system in waves. In *International offshore and polar engineering conference*, volume I, pages 279–285, 2001. ISBN 1-880653-51-6. URL <http://e-book.lib.sjtu.edu.cn/isope2001/pdf/files/papers/044.pdf>.
- [10] W-H. Tsai J. C. S. Yang , C. H. Marks , J. Jiang , D. Chen , A. Elahi. Determination of Fluid Damping Using Random Excitation. *Journal of Energy resources technology*, 107(2):220–225, 1985. doi: <https://doi.org/10.1115/1.3231180>.
- [11] Sandrine Jamet. NEMOH-Presentation - LHEEA. URL <https://lheea.ec-nantes.fr/logiciels-et-brevets/nemoh-presentation-192863.kjsp>.
- [12] H Jasak, V Vukčević, I Gatin, and I Lalović. CFD validation and grid sensitivity studies of full scale ship self propulsion. *International Journal of Naval Architecture and Ocean Engineering*, 2017. ISSN 20926790. doi: 10.1016/j.ijnaoe.2017.12.004.
- [13] J M J Journée and W W Massie. *Offshore Hydromechanics, second edition*. Delft University of Technology, Delft, 2008.
- [14] F J Koppes. Numerical Modelling of Interconnected Floating Solar Energy Platforms. Technical report, 2019.
- [15] B Le Méhauté. *An introduction to hydrodynamics and water waves.*, volume 22. 1977. ISBN 0387072322. doi: 10.4319/lo.1977.22.5.0974.
- [16] J Leprou. Analysis and design of the interconnector system for a multibody interconnected floating offshore solar farm. Technical report, ENSTA Bretagne, 2019.

- [17] C Liu and J Chen. Observations of hysteresis in flow around two square cylinders in a tandem arrangement. *Journal of Wind Engineering and Industrial Aerodynamics*, 90:1019–1050, 2002.
- [18] M Liu, L Xiao, and L Yang. Experimental investigation of flow characteristics around four square-cylinder arrays at subcritical Reynolds numbers. *International Journal of Naval Architecture and Ocean Engineering*, 7(5):906–919, 2015. ISSN 2092-6782. doi: 10.1515/ijnaoe-2015-0063. URL <http://dx.doi.org/10.1515/ijnaoe-2015-0063>.
- [19] D P. Loucks, E van Beek, J R. Stedinger, J P.M. Dijkman, and MT. Villars. *Model Sensitivity and Uncertainty Analysis for Water Resources*. 2005. ISBN 9231039989. doi: ISBN:92-3-103998-9. URL [https://www.utwente.nl/ctw/wem/education/afstuderen/Loucks{}\\_VanBeek/09{}\\_chapter09.pdf](https://www.utwente.nl/ctw/wem/education/afstuderen/Loucks{}_VanBeek/09{}_chapter09.pdf).
- [20] E Malta, F Matsumoto, R Goncalves, F Pereira, A Fajarra, and K Nishimoto. Damping Coefficient Analyses for Floating Offshore Structures. *OMAE*, (June), 2010. doi: 10.1115/OMAE2010-20093.
- [21] Marin. aNySIM\_General\_Information. pages 1–8.
- [22] MARIN. aNySIM Theory Documentation. Technical report, 2000.
- [23] MARIN. DIFFRAC User Guide, 2018.
- [24] P. A. Martin and A. G. Dixon. The scattering of regular surface waves by a fixed, half-immersed, circular cylinder. *Applied Ocean Research*, 5(1):13–23, 1983. ISSN 01411187. doi: 10.1016/0141-1187(83)90053-6.
- [25] J.R. Morison. The Force Distribution Exerted by Surface Waves on Piles. Technical report, Institute of Engineering Research - Waves Research Laboratory, Berkely, 1953.
- [26] J.R. Morison, J.W. Johnson, and S.A. Schaaf. The Force Exerted by Surface Waves on Piles. *Journal of Petroleum Technology*, 2(05):149–154, 1950. ISSN 0149-2136. doi: 10.2118/950149-G. URL <http://www.onepetro.org/doi/10.2118/950149-G>.
- [27] M Naciri, O Waals, and J De Wilde. TIME DOMAIN SIMULATIONS OF SIDE-BY-SIDE MOORED VESSELS LESSONS LEARNT FROM A BENCHMARK TEST. In *International Conference on Offshore Mechanics and Arctic Engineering Proceedings of OMAE2007*, pages 1–11, 2007.
- [28] H Nowacki, J Moss, E Snyder, and B Young. *Experiments on the resistance of a family of boxlike hull forms for amphibious vehicles*. University of Michigan, college of engineering, 1968.
- [29] Oceans of energy. Home | Oceans of Energy | Clean and Renewable Energy. URL <https://oceansofenergy.blue/>.
- [30] Offsetsolar. The World's First Floating Solar Farm. URL <https://www.offsetsolar.com/blogs/offset-solar-blog/first-floating-solar-farm>.
- [31] WJ Otto, A Nap, and R Heijmen. ZON OP WATER Offshore, 2019.
- [32] M Peñalba Retes, G Giorgi, and J V. Ringwood. A Review of non-linear approaches for wave energy converter modelling. In *11th European Wave and Tidal Energy Conference*, number 1, pages 1–10, 2015. ISBN 2309-1983.
- [33] J A Pinkster. *Low frequency second order wave exciting forces on floating structures*. PhD thesis, Delft University of Technology, 1980.
- [34] M H J Van Poppelen. Comparison of time domain simulations with model tests for a single- and multi-body offshore floating solar system. Technical report, University of Twente, 2019.
- [35] D. M. Skene, L. G. Bennetts, M. H. Meylan, and A. Toffoli. Modelling water wave overwash of a thin floating plate. *Journal of Fluid Mechanics*, 777(July), 2015. ISSN 14697645. doi: 10.1017/jfm.2015.378.
- [36] D. M. Skene, L. G. Bennetts, M. Wright, M. H. Meylan, and K. J. Maki. Water wave overwash of a step. *Journal of Fluid Mechanics*, 839(March):293–312, 2018. ISSN 14697645. doi: 10.1017/jfm.2017.857.
- [37] F Sonnenwald, V Stovin, and I Guymer. Estimating drag coefficient for arrays of rigid cylinders representing emergent vegetation. *Journal of Hydraulic Research*, 2018. doi: 10.1080/00221686.2018.1494050.

- [38] L Sun, R Taylor, and P Taylor. First- and second-order analysis of resonant waves between adjacent bargesite. *Journal of Fluids and Structures*, 26:954–978, 2010.
- [39] L. Sun, R. Eatock Taylor, and Y. S. Choo. Responses of interconnected floating bodies. *IES Journal Part A: Civil and Structural Engineering*, 4(3):143–156, 2011. ISSN 19373260. doi: 10.1080/19373260.2011.577933.
- [40] Z Tajali and M Shafieefar. Hydrodynamic analysis of multi-body floating piers under wave action. *Ocean Engineering*, 38(17-18):1925–1933, 2011. ISSN 00298018. doi: 10.1016/j.oceaneng.2011.09.025. URL <http://dx.doi.org/10.1016/j.oceaneng.2011.09.025>.
- [41] A Toffoli, L G Bennetts, M H Meylan, C Cavaliere, A Alberello, J Elsnab, and J P Monty. Geophysical Research Letters Sea ice floes dissipate the energy of steep ocean waves. 2015. ISSN 19448007. doi: 10.1002/2015GL065937.
- [42] B Uwihanganye, C A Adenya, and H M Ndiritu. REVIEW OF NUMERICAL APPROACH USED IN THE OPTIMIZATION OF MOORING SYSTEMS FOR FLOATING STRUCTURES . *International Journal of Engineering Technology and Scientific Innovation*, (05), 2018.
- [43] J van den Berg and W.H Pauw. Introduction to aNySIM XMF, 2018.
- [44] S Weller and S Gueydon. Analysis of the DeepCwind model tests and a first attempt to simulate a semi-submersible floating wind platform with aNySIM Final report. Technical Report September 2017, MARIN, 2012. URL [www.marin.nl](http://www.marin.nl).
- [45] G Weymouth. Marine Hydrodynamics: viscous flow. Technical report, Southampton, 2018.
- [46] W S Yang. *Hydrodynamic Analysis of Mooring Lines Based on Optical Tracking Experiments*. PhD thesis, Texas A&M University, 2007.
- [47] X Zhang, S Draper, H Wolgamot, W Zhao, and L Cheng. Eliciting features of 2D greenwater overtopping of a fixed box using modified dam break models. *Applied Ocean Research*, 84(January):74–91, 2019. ISSN 01411187. doi: 10.1016/j.apor.2019.01.006.



# Basin model details

## A.1. Test details

Test type	Test name	Notation	Wave height [m]	Wave period [m]	Water depth [m]	Wave angle BT [°]	Wave angle AS [°]	Ang frequen cy	Wave length [m]	Steep ness [-]
<b>Zero procedures</b>										
	Pretension	Z-15	-	-	25	-	-	-	-	-
<b>Static offset</b>										
	Sweep Y basin fixed	S-17	-	-	25	-	-	-	-	-
	Sweep X basin fixed	S-18	-	-	25	-	-	-	-	-
<b>Decay</b>										
	Surge Decay	D-12	-	-	25	-	-	-	-	-
	Sway Decay	D-13	-	-	25	-	-	-	-	-
	Yaw Decay	D-14	-	-	25	-	-	-	-	-
<b>Regular wave</b>										
	Eigen frequency surge	R-50	1.5	6.80	25	270	180	0.92	72.19	0.021
	Eigen frequency surge	R-51	1.5	7.05	25	270	180	0.89	77.60	0.019
	Eigen frequency surge	R-52	1.5	6.55	25	270	180	0.96	66.98	0.022
	Eigen frequency sway	R-53	1.5	6.80	25	180	90	0.92	72.19	0.021
	Eigen frequency sway	R-54	1.5	7.05	25	180	90	0.89	77.60	0.019
	Eigen frequency sway	R-55	1.5	7.30	25	180	90	0.86	83.20	0.018
	Interconnector test	R-56	1.5	8.00	25	260	170	0.79	99.92	0.015
	Interconnector test	R-57	1.5	9.00	25	260	170	0.70	126.47	0.012
	Interconnector test	R-58	1.5	10.00	25	260	170	0.63	156.13	0.010
<b>Irregular wave</b>										
	Service limit state 180	I-3	2.0	6.70	25	270	180	0.94	70.09	0.029
	Service limit state 135	I-4	2.0	6.70	25	225	135	0.94	70.09	0.029
	Service limit state 105	I-5	2.0	6.70	25	195	105	0.94	70.09	0.029
	Service limit state 90	I-6	2.0	6.70	25	180	90	0.94	70.09	0.029
	Bridging to ULS 1 135	I-7	2.90	8.00	25	225	135	0.79	99.92	0.029
	Bridging to ULS 1 90	I-8	2.90	8.00	25	180	90	0.79	99.92	0.029
	Bridging to ULS 2 135	I-9	3.75	9.20	25	225	135	0.68	132.15	0.028
	Bridging to ULS 2 90	I-10	3.75	9.20	25	180	90	0.68	132.15	0.028
	Bridging to ULS 3 135	I-11	4.75	10.40	25	225	135	0.60	168.87	0.028
	Bridging to ULS 3 90	I-12	4.75	10.40	25	180	90	0.60	168.87	0.028
	Bridging to ULS 4 135	I-13	5.90	11.60	25	225	135	0.54	210.09	0.028
	Bridging to ULS 4 90	I-14	5.90	11.60	25	180	90	0.54	210.09	0.028
	Ultimate limit state 180	I-15	7.00	12.70	25	270	180	0.49	251.82	0.028
	Ultimate limit state 135	I-16	7.00	12.70	25	225	135	0.49	251.82	0.028
	Ultimate limit state 135	I-16	7.00	12.70	25	225	135	0.49	251.82	0.028
	Ultimate limit state 105	I-17	7.00	12.70	25	195	105	0.49	251.82	0.028
	Ultimate limit state 90	I-18	7.00	12.70	25	180	90	0.49	251.82	0.028

Figure A.1: Details of all tests executed in offshore basin

## A.2. Video footage findings

	System behaviour	Vortices/Waves at end of floater	Water flowing through gaps	Overflowing water	Mooring line dynamics	Breaking waves	Acting as a wave follower	Slaming behaviour
<b>R</b>								
50	The twelve floaters behave as one	Similar waves can be observed as with nr. 56	Very little water flowing through gaps	Water overflowing every cycle similar to 50	Very small wrinkles can be observed around the mooringline	No breaking waves	Yes	No
51	The twelve floaters behave as one	Similar waves can be observed as with nr. 56	Very little water flowing through gaps	Water overflowing every cycle similar to 50	Very small wrinkles can be observed around the mooringline	No breaking waves	Yes	No
52	The twelve floaters behave as one	Similar waves can be observed as with nr. 56	Very little water flowing through gaps	Water overflowing every cycle similar to 50	Very small wrinkles can be observed around the mooringline	No breaking waves	Yes	No
53	The twelve floaters behave as one	Clear waves can be observed due to motion of floater system	Some water is flowing through gaps	Overflowing water mainly caused by water through gaps	Very small wrinkles can be observed around the mooringline	No breaking waves	Yes	No
54	The twelve floaters behave as one	Clear waves can be observed due to motion of floater system	Some water is flowing through gaps	Overflowing water mainly caused by water through gaps	Very small wrinkles can be observed around the mooringline	No breaking waves	Yes	No
55	The twelve floaters behave as one	Clear waves can be observed due to motion of floater system	Some water is flowing through gaps	Overflowing water mainly caused by water through gaps	Very small wrinkles can be observed around the mooringline	No breaking waves	Yes	No
56	The twelve floaters behave as one	Clear waves can be observed due to motion of floater system	Some water is flowing through gaps	Less overflowing water every cycle than with 50	Very small wrinkles can be observed around the steel line	No breaking waves	Yes	No
57	The twelve floaters behave as one	Very little waves can be observed	Less water is flowing through gaps than 56	Less overflowing water every cycle than with 50 and 56	Very small wrinkles can be observed around the mooringline	No breaking waves	Yes	No
58	The twelve floaters behave as one	None can be observed	Less water is flowing through gaps than 56,57	Less overflowing water every cycle than with 50 and 56,57	Very small wrinkles can be observed around the mooringline	No breaking waves	Yes	No
<b>I</b>								
3	The twelve floaters behave as one	Yes, almost constantly (depending on period)	Water can be clearly seen flowing through the gaps, mostly horizontal gaps	Water overflowing every cycle, more than in regular waves	Very small wrinkles can be observed around the mooringline	No breaking waves	Only in some moments in time	Yes, in some cases
4	The twelve floaters behave as one, bending effects in joints become more visible	Yes, More strongly dependent on period	Less water is flowing through horizontal gaps	Water overflowing but less regularly than with 3 (asymmetric)	Very small wrinkles can be observed around the mooringline	No breaking waves	Only in some moments in time	Not observed
5	The twelve floaters behave as one, bending effects in joints become more visible	Yes, More strongly dependent on period	Less water is flowing through horizontal gaps, more trough vertical	Water overflowing but less regularly than with 3 (asymmetric) and in some cases clearly in 2 directions: due to roll motion of the floaters	Very small wrinkles can be observed around the mooringline	No breaking waves	Cannot be observed	Not observed
6	The twelve floaters behave as one	Yes, almost constantly (depending on period)	More water through vertical gaps	More water is overflowing than in 4	Very small wrinkles can be observed around the mooringline	No breaking waves	Cannot be observed	Very little slaming can be observed
7	The twelve floaters behave as one, bending effects in joints become more visible	More waves visible than in 4	A bit more water than in 4	More water is overflowing than in 4	Very small wrinkles can be observed around the mooringline	No breaking waves	Cannot be observed	Not observed
8	The twelve floaters behave as one	Yes constantly	More water through vertical gaps	Water overflowing in two directions similar to 6	Very small wrinkles can be observed around the mooringline	No breaking waves	Cannot be observed	No slaming, more diving of first columns of floaters
9	The twelve floaters behave as one, bending effects in joints become more visible	Comparable to 7	Comparable to 7	Water is overflowing heavier than for 7	Very small wrinkles can be observed around the mooringline	No breaking waves	Cannot be observed	No slaming, more diving of first columns of floaters
10	The twelve floaters behave as one	Comparable to 8	Comparable to 8	No clear difference with 8	Very small wrinkles can be observed around the mooringline	No breaking waves	Cannot be observed	No slaming, more diving of first columns of floaters
11	The twelve floaters behave as one, bending effects in joints become more visible	Comparable to 7	Comparable to 7	Water is overflowing heavier than for 7	Very small wrinkles can be observed around the mooringline	No breaking waves	Cannot be observed	Slaming of the corners of the floaters
12	The twelve floaters behave as one	More than 8	More water flowing through than for 8 and 10	Water is overflowing heavier than for 8	Very small wrinkles can be observed around the mooringline	No breaking waves	Cannot be observed	floaters in some cases
13	The twelve floaters behave as one, bending effects in joints become more visible	Comparable to 11	Mainly water overflowing so water trough gaps is difficult to observe	In some cases very heavy overflowing water	Very small wrinkles can be observed around the mooringline	No breaking waves	Cannot be observed	floaters (floaters come out of the water)
14	The twelve floaters behave as one	Comparable to 12	Mainly water overflowing so water trough gaps is difficult to observe	In some cases very heavy overflowing water	Very small wrinkles can be observed around the mooringline	Incidental breaking wave	Cannot be observed	Slaming of floaters in some cases

Figure A.2: Overview of the findings from the video footage of regular and irregular wave tests performed in the offshore basin. Several aspects have been identified and analysed to study the trends

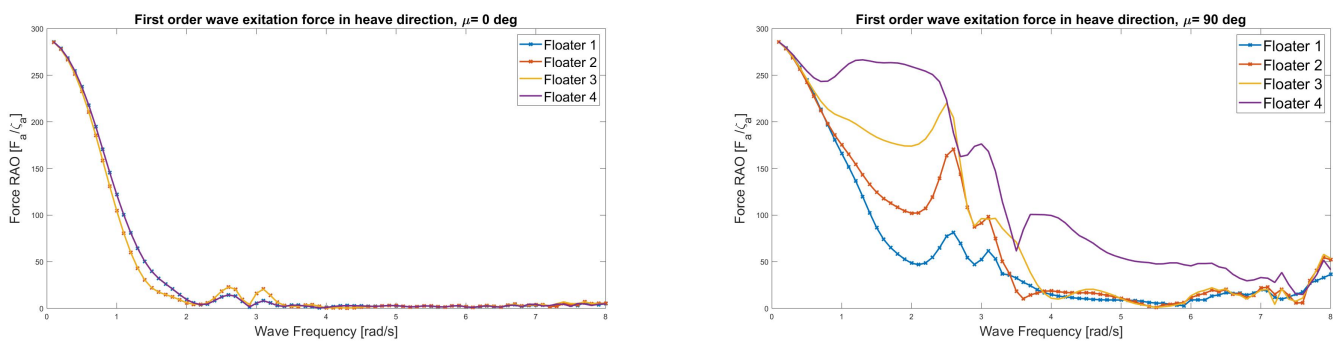
# B

## DIFFRAC method and verification

In this appendix, the data obtained in DIFFRAC and used in aNySIM is explained in more detail.

### B.1. First order excitation force

First order excitation forces and moments are determined for each frequency in all wave directions for all six degrees of freedom. The hyd file contains the force amplitude as the  $RAO = \frac{F_a}{\zeta_a}$  and the force phase as  $\epsilon_{F\zeta}$ . To explain how the 12 independent bodies are taken into account, figure B.1 shows the first order excitation force in heave direction in head and beam waves. The excitation force for floater nr. 1 to 4 over the range of frequencies is shown. For a wave with a wave direction of  $\mu = 0^\circ$  (figure B.1a), the entire system is symmetric with the symmetry line between floater 2 and 3. Therefore, floater 2 and 3 have the same result, as well as floater 1 and 4. The difference between the floaters can be explained by the presence of the other floaters when the forces are calculated. The force on floater 1 is calculated by an incoming potential that is composed of the undisturbed incoming potential in combination with the reflection of the other bodies present. The same method holds for floater 2, 3 and 4. The presence of other bodies becomes more clear when the wave exciting force in heave direction is observed for waves with direction  $\mu = 90^\circ$ , see figure B.1b. Floater 4 is the first floater that is encountered by the wave and therefore the force RAO is largest on this floater. From floater 4 to 1 the impact of the incoming wave decreases due to the presence of the other floaters, resulting in a much lower RAO for floater 1. A note must be made that for low frequencies (long waves), the force RAO is the same for all 4 floaters. This is due to the fact that in long waves the floaters act as a wave follower and the wave 'does not feel' the presence of the previous floaters.



(a) Incoming waves at  $\mu = 0$

(b) Incoming waves at  $\mu = 90$

Figure B.1: First order wave excitation force RAO in z direction for floater 1 to 4 in 2 different wave directions. These values are directly obtained from the hyd file as calculated in DIFFRAC.

### Verification

To analyse the excitation force, analytical calculations will be compared with the input from the hydfile, in which the force RAO is given:  $\frac{F_{ex}}{\zeta_a}$ . To calculate the excitation force, the Froude Krylov and diffraction force

need to be computed. However, solving for the diffraction problem cannot be done analytically. This diffraction force is expected to be very small, as the wave length of the incoming wave is 6 times larger than the floater length [24]. Therefore, the diffraction is neglected and only the Froude Krylov component is calculated: The Froude Krylov force is calculated assuming the linear Bernoulli equation, resulting in:

$$F_{FK} = -\rho \int_S \frac{\delta\Phi_I}{\delta t} \mathbf{n} dS \quad (\text{B.1})$$

With

$$\frac{\delta\Phi_I}{\delta t} = -\zeta_a g e^{kz} \cos(kx \cos(\mu) + ky \sin(\mu) - \omega t) \quad (\text{B.2})$$

Since the structure can be seen as a simple barge, the Froude Krylov force RAO in x, y and z direction can be calculated separately, resulting in the following equations:

$$\frac{F_{FK_x}}{\zeta_a} = B \rho g [1/k e^{-kz}]_{-D}^0 \cdot (\cos(kL/2 - \omega t) - \cos(-kL/2 - \omega t)) \quad (\text{B.3})$$

$$\frac{F_{FK_y}}{\zeta_a} = L \rho g [1/k e^{-kz}]_{-D}^0 \cdot (\cos(kB/2 - \omega t) - \cos(-kB/2 - \omega t)) \quad (\text{B.4})$$

$$\frac{F_{FK_z}}{\zeta_a} = B \rho g e^{-kD} [1/k \sin(kx - \omega t)]_0^L \quad (\text{B.5})$$

Where:

- B = width of structure
- L = length of structure
- D = Draft of structure

The RAO for the analytically calculated Froude Krylov force in heave direction is compared to the excitation force RAO obtained from DIFFRAC. As can be seen in figure B.2 there is a difference in amplitude between the two force RAO's. This difference is caused by neglecting the diffraction force.

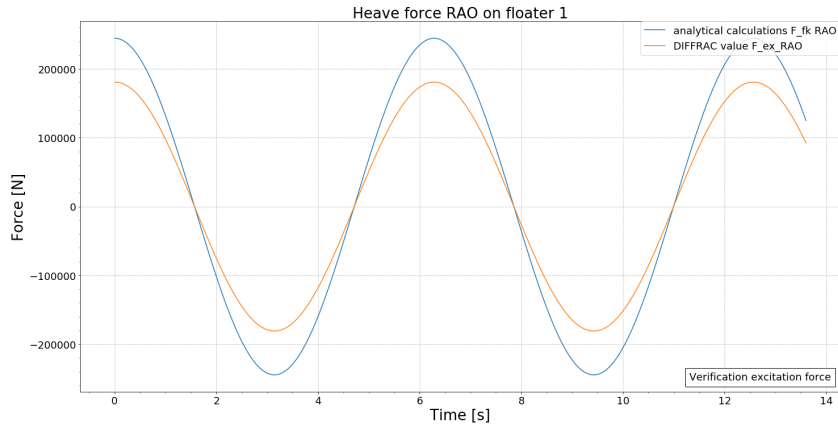


Figure B.2: analytic Froude Krylov force calculations compared to the first order excitation force RAO obtained from DIFFRAC

## B.2. Second order excitation force

The results of computation of these second order forces in DIFFRAC is stored in the hyd file as the quadratic transfer functions (QTF) of the mean and low frequency force and moment components. The QTF can be split in a real part, P, which is in-phase with the low frequency part of the square of the incident wave, and in a imaginary part, Q, which is out-of-phase. Both P and Q are given as 4D matrices with the form of  $(80 \times 20 \times 25 \times 6)$ , which consists of:

- An array of 80 frequencies ( $f_i$ ) from 0 to 8 rad/s.
- An array of 20 frequencies ( $f_j$ ), from frequency ( $f_i$ ) to the twentieth consecutive frequency with a maximum of 8 rad/s. For  $f_{i=80} = 8$ , this means that there is only 1 frequency ( $f_{j=80} = 8$ ).
- An array of 25 wave directions, from 0 to 360
- An array of all 6 DOF

For the square of two incident waves with the same frequency, the difference part becomes zero, therefore only the mean part remains of the in-phase part. This is the mean wave drift force. The out-of-phase part becomes entirely 0. All other (off-diagonal) QTF's contain both the mean and low frequency part. The P and Q matrices are calculated for waves in all 25 directions  $\mu$  and for all degrees of freedom. To illustrate the different shares of P and Q for different situations, figure B.3 shows two situations with different incoming wave frequency. Figure B.3a shows the results for  $\omega_i = \omega_j$  for all frequencies. Here the out-of-phase part is 0 and the in-phase part P only shows the mean value. Figure B.3b shows results for the total QTF and the subparts Q and P for the combination of two consecutive waves.

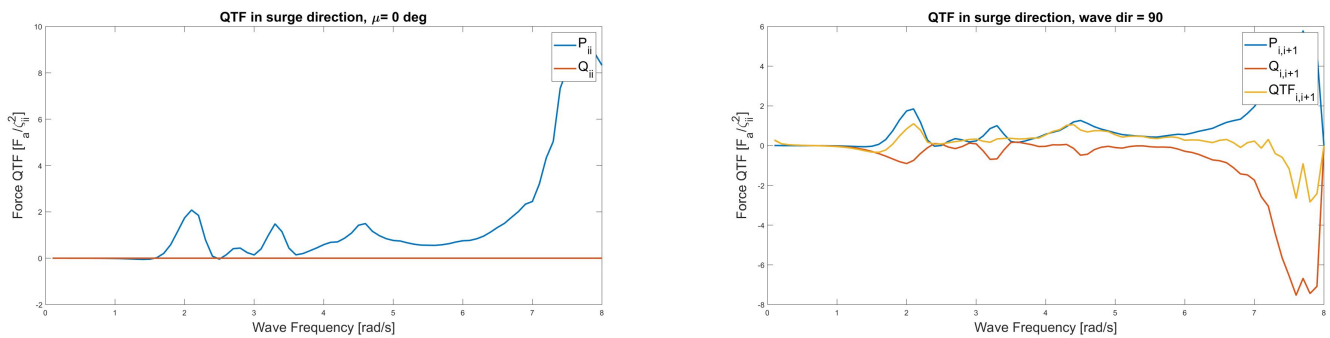
(a) P and Q parts of QTF for  $\omega_i = \omega_j$ (b) P and Q parts of QTF for  $\omega_i = \omega_{j+1}$ 

Figure B.3: Second order wave excitation force QTF values for 2 different combinations of wave frequencies. These values are directly obtained from the hyd file as calculated in DIFFRAC.

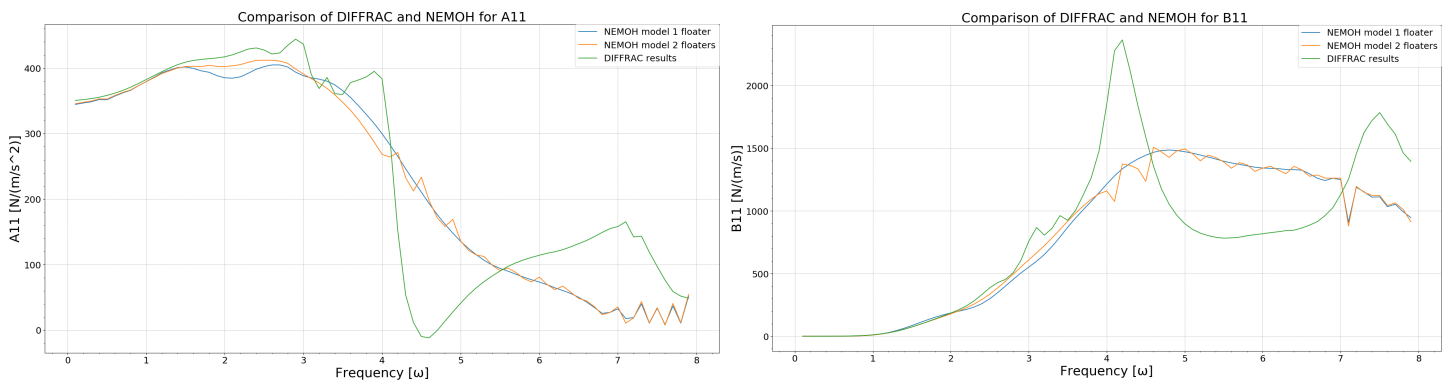
### B.3. Hydrodynamic coefficients

The radiation problem is solved in DIFFRAC to obtain the hydrodynamic coefficients, damping and added mass. This problem is solved linearly, ie the time dependent instantaneous wetted surface is neglected. Both coefficients are calculated for 80 frequencies between 0 and 8rad/s. The added mass matrix consists of the added mass in each degree of freedom due to a motion in the same or another degree of freedom (6x6 matrix for 1 floater), and the coupling between all floaters ie. the influence of all six motions of floater 2 to 12 on all six motions of floater 1. This results in a matrix of 72x72 for each frequency. Similar results are obtained for the hydrodynamic damping of the bodies.

#### Verification

The hydrodynamic coefficients calculated in DIFFRAC will be verified using different numerical diffraction software; NEMOH [11]. The NEMOH model has been developed by Koppes in [14] for 1 floater and 2 floaters side by side. This allows for a comparison of the hydrodynamic coefficients of a single floater and the coupled coefficients.

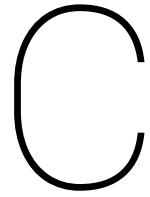
Results are shown for  $a_{11}$ ,  $b_{11}$ , the surge-surge added mass and damping of floater 1. The range of frequencies present in the incoming wave frequencies is from 0.6 to 1.2 rad/s. As shown in the figures, both the added mass as the damping values are equal. The differences that occur in the higher frequencies are a result of gap resonance. This effect will therefore most likely also become equal if the NEMOH model would be extended with 12 floaters. However, for this research, the frequency range that is simulated gives equal results. More verification on DIFFRAC demonstrated that the two diffraction software's give similar results for other DOF's as well [14].



(a) Results of the added mass in surge direction of 1 floater, comparing the DIFFRAC software with calculations in NEMOH.

(b) Results of the damping in surge direction of 1 floater, comparing the DIFFRAC software with calculations in NEMOH.

Figure B.4: Comparing the DIFFRAC software with calculations in NEMOH. Results are equal for the range of wave exciting frequencies (0.6-1.2 rad/s). The irregularities in higher frequencies, caused by gap resonance effects, can therefore be neglected in this research.



# aNySIM implementation

In this appendix, the content of the XMF files used in aNySIM is presented. For more detail on the specifics, the aNySIM documentation can be consulted [22, 43].

## C.1. Main XMF file

xship::Time

- **Timestep[s]**: Used for integration
- **Starttime[s]**: Time at which simulation start
- **Endtime[s]**: Time at which simulation stops

xship::Waves

- **waterDensity[ $kg/m^3$ ]**: seawater
- **waterDepth[m]**: Depending on simulation 22 or 25 metres
- xship::Timetracespectrum

**direction**: Depending on simulation

**txt file**: Txt file fo wave elevation retrieved from basin tests corresponding simulation

**refpos**: Position where wave elevation is implemented

xship::Current

- **Depths**: Vector of depths for current layer
- **Directions**: Vector of directions at current layer
- **Speeds**: Vector of speeds at current layer

xsf::LineconnectionPoint "Anchor"

- **Position**: Vector of location of anchor point

xship::Hyddb "hyddb0"

- **Filename**: Location and filename of hyd file
- **Hydcenter**: Vector of hyd file coordinate system origin in GCS

xmf::Integrator "Integrator"

- `xship::Body "Floater"`: Defines the location for the submodel of a floater. See C.2
  - position**: The position of the LCS origin of a floater in the GCS
  - hydDbIndex floater**: Defines which floater from the hydrodynamic data base needs to be connected to the specific floater in a submodel.
- `xship::Hydinteratcion "Floater"`: Defines the bodies and interaction between the bodies that is loaded from the hydrodynamic database.
  - hydDbName**: The name of the hydrodynamic database that is used, from which the location is loaded from `xship::HydDb`.
  - body**: Defines the bodies that need to be taken into account for the hydrodynamic interaction. These are all the floaters.
- `xship::Joint "Joint"`: Defines the location for the submodel of a joint. See C.4
  - body1**: The first body that is used as a connection point for the joint. This is a floater.
  - body2**: The second body that is used as a connection point for the joint. This is a floater.
- `xship::Mooringline "Mooring line"`: Defines the location for the submodel of a mooring line. See C.3
  - con0**: The first connection point of the mooring line, this is a floater.
  - con1**: The second connection point of the mooring line, this is an anchor.
  - buoyPos**: The initial location of the buoy in the GCS
  - buoyyaw**: The initial yaw angle of the buoy in the GCS
- **algorithm**: Defines which integration algorithm is used. In this case Runge Kutta 4.
- **tolerance**: The tolerance of the system.

## C.2. Sub XMF file - Floater

**Property references**: Loads in the references from the main file for a specific floater, ie. the hydrodynamic index and the reference position of the floater in GCS.

```
xmf::Body "Floater"
```

- `anysim::ForceSeries "serie1"`: An external force series to be applied on a floater. e.g. for initial displacement for decay test.
  - Position**: Location on floater to apply force to.
  - file**: The location of the txt file with external force.
- `xsf::Visualisation "coordinatesystem"`: Information on the visualisation of the local coordinate systems on a floater.
  - Geometry file**: Location of the file with coordinate system drawing
  - scale**: At what scale the LCS should be visualised.
- `xsf::Visualisation "vizpanelfloat"`: Information on the visualisation of the floater.
  - Geometry file**: Location of the file with floater drawing
  - scale**: At what scale the floater should be visualised.
- `xship::LinearHydrostatics "hydrostat"`: Loads in the linear hydrostatics from the hyd file
  - Lpp**: Length between perpendiculars
  - ta**: Draft aft
  - tf**: Draft fore
  - beam**: Width of the floater
  - hydDbName**: Loads the hydrodynamic database name from the main file
  - hydDbIndex**: Loads the hydrodynamic database index for this specific floater from the main file
- `xship::Excitation "ex"`: Loads in the linear excitation force
  - hydDbName**: Loads the hydrodynamic database name from the main file
  - hydDbIndex**: Loads the hydrodynamic database index for this specific floater from the main file

- `xship::SecondOrderExcitation "ex2"`: Loads in the second order (mean and low frequency) excitation force
  - hyddbName**: Loads the hydrodynamic database name from the main file
  - hyddbIndex**: Loads the hydrodynamic database index for this specific floater from the main file
  - factors**: Multiplication factors for forces in all 6DOF. IF this is 0, the second order forces are not taken into account in that specific direction.
  - Update interval**: The interval can be set for updating the low frequency wave force. In intermediate time steps the loads will be taken constant.
- `xsf::LineConnectionPoint "line"`: Defines a mooring line connection point.
  - position**: The location given in the LCS.
- `xship::LinearDamping "ldampadd"`: Defines the linear damping in all 6DOF
  - $b_{jj}$ : The direction for which the damping is defined.
- `xship::QuadraticDamping "qdampadd"`: Defines the quadratic damping in all 6DOF
  - $b_{jj}$ : The direction for which the damping is defined.
- **Roll**: the initial roll angle of the floater.
- **Pitch**: the initial pitch angle of the floater.
- **Yaw**: the initial yaw angle of the floater.
- **relcom**: The location of the centre of gravity in the LCS
- **refpos**: The location of the origin of the LCS in the GCS. This is loaded from the main file.
- **Mass**: Mass of the floater
- **kxx/kyy/kzz**: radius of gyration in respectively roll, pitch and yaw direction.

### C.3. Sub XMF file - Mooring system catenary line

**Property references** : Loads in the references from the main file for a specific mooring line, ie. the reference positions of the floaters for connection.

`xlines::CompositeCatenaryLine "Mooringline"`: Defines the connections of the mooring line and the properties of the different segments.

- **connection 0 and 1**: loads the two connection points of the mooring line (the floater and the anchor)
- **unbreakable**: True - the line cannot break
- `xlines::CatenarySegment`: loads all properties for segment
  - length**: Length of line segment
  - massPerMeter**: Mass in air of line segment
  - submWeightPerMEter**: Submerged weight of line segment
  - AxialStiffness**: Stiffness of segment in axial direction

### C.4. Sub XMF file - Joints

**Property references** : Loads in the references from the main file for a specific mooring line, ie. the reference positions of the floaters for connection, and the locations and orientations of the buoy.

`anysim::Joint`: Defines the properties of the joints and the locations at which they are attached to the relevant floaters

- $c_{jj}$ : The stiffness in the joints in axial, transverse, bending and torsion direction.
- **blinear $_{jj}$** : the mechanical damping of the joints in all 6 directions
- **ignoreInitialOffset**: The force is calculated the relative distance between the floaters, in which the initial distance is ignored.
- **object1/2**: The 2 floaters to which the joint is connected
- **point1/2**: The connection points on the relevant floaters.

## C.5. Sub XMF file - Mooring system Lumped mass line

**Property references** : Loads in the references from the main file for a specific mooring line, ie. the reference positions of the floaters for connection.

`xlines::LumpedmassLine "Mooringline"`: Defines the connections of the mooring line and the properties of the different segments. Segments can be divided in elements. The amount of elements influences the computational time and accuracy of the calculation.

- **connection 0 and 1**: loads the two connection points of the mooring line (the anchor and the floater)
- **unbreakable**: True - the line cannot break
- **nStep**: Number of timesteps within the overall integration time step to ensure a stable solution.
- `xlines::Lumpedmassegment`: loads all properties for segment
  - length**: Length of line segment
  - massPerMeter**: Mass in air of line segment
  - submWeightPerMEter**:Submerged weight of line segment
  - AxialStiffness**: Stiffness of segment in axial direction
  - Diameter**: Diameter of the line; important for calculations of hydrodynamic forces
  - NormalDragCoeff**: Drag coefficient in normal direction of the segment of the line. Used for Morison equation.
  - TangentDragCoeff**: Drag coefficient in tangent direction of the segment of the line. Used for Morison equation.
  - NormalInertiaCoeff**: Inertia (Added mass) coefficient in normal direction of the segment of the line. Used for Morison equation.
  - TangentInertiaCoeff**: Inertia (Added mass) coefficient in tangent direction of the segment of the line. Used for Morison equation.
  - axialDampingPercentage**: Mechanical damping of line, used to stabilise the integration
  - TangentDampingPercentage**: Mechanical damping of line, used to stabilise the integration
  - NumberofElements**: Number of elements within a segment



## aNySIM simulations

Different simulations that were performed in aNySIM are briefly explained in this appendix.

### D.1. Zero procedure

Zero procedures were performed in aNySIM by adding no external forces and run the simulation for a period of 200seconds, in which the system has the time to reach static equilibrium. From this zero procedure the pretension in the mooring lines and joints can be derived.

### D.2. Static offset test

Static offset simulations were performed using an external force in 1 degree of freedom (surge,sway) that is increased over time to simulate a displacement. The following steps were executed:

1. Determine simulation time to reach static state
2. Generate txt file with force ladder in one degree of freedom, applied from static state time onwards, see figure D.1
3. "Freeze" all other motions
4. Run static offset simulation with external force applied to all floaters
5. Plot mooring line forces against displacement in degree of freedom.

```
0.0      0.0 0.0 0.0 0.0 0.0 0.0
20.0     0.0 0.0 0.0 0.0 0.0 0.0
30.0     0.0 0.0 0.0 0.0 0.0 0.0
40.0    -75.0 0.0 0.0 0.0 0.0 0.0
50.0    -60.0 0.0 0.0 0.0 0.0 0.0
60.0    -45.0 0.0 0.0 0.0 0.0 0.0
70.0    -30.0 0.0 0.0 0.0 0.0 0.0
80.0    -15.0 0.0 0.0 0.0 0.0 0.0
90.0     0.0 0.0 0.0 0.0 0.0 0.0
100.0    15.0 0.0 0.0 0.0 0.0 0.0
110.0    30.0 0.0 0.0 0.0 0.0 0.0
120.0    45.0 0.0 0.0 0.0 0.0 0.0
130.0    60.0 0.0 0.0 0.0 0.0 0.0
140.0    75.0 0.0 0.0 0.0 0.0 0.0
150.0    90.0 0.0 0.0 0.0 0.0 0.0
```

Figure D.1: txt file used for static offset in surge direction

### D.3. Decay tests

Decay tests were performed using an external force in 1 degree of freedom (surge, sway or yaw) to generate an initial displacement after which the external force is set to 0. The following steps were executed for surge and yaw:

1. Determine simulation time to reach static state
2. Determine required force to obtain initial displacement that is in agreement with basin tests initial displacement
3. Generate txt file with initial force in one degree of freedom, applied for 15 seconds to obtain steady and set to 0 in 1 second on all floaters, see figure D.2a
4. Run decay simulation with external force applied to all floaters
5. Plot displacement of floater 7 against time to compare with basin decay test

The method used to give the floaters an initial yaw angle is different from the method used for surge and sway, since the entire system must be given a yaw moment instead of all floaters separately. Two couple moments are applied on the outer floaters to give the entire system a yaw angle. The applied forces are kept constant for a time span long enough to allow the system to obtain a new equilibrium. In this new equilibrium, all individual floaters have reached their yaw angle.

For the decay test in yaw direction floater 1 and 12 are given external loads in y direction and floater 4 and 9 external loads in x direction. The floaters are not given an external yaw moment, this is obtained by the applied couple moment. To reach the steady state, the forces are applied for 30 seconds instead of 15.

```
0.0      0.0 0.0 0.0 0.0 0.0 0.0
15.0     22.0 0.0 0.0 0.0 0.0 0.0
30.0     22.0 0.0 0.0 0.0 0.0 0.0
31.0     0.0 0.0 0.0 0.0 0.0 0.0
```

(a) txt file used for decay test in surge direction

```
0.0      0.0 0.0 0.0 0.0 0.0 0.0
15.0     0 -145.0 0.0 0.0 0.0 0.0
30.0     0 -145.0 0.0 0.0 0.0 0.0
45.0     0 -145.0 0.0 0.0 0.0 0.0
47       0.0 -155.0 0.0 0.0 0.0 0.0
47.5     0.0 0.0 0.0 0.0 0.0 0.0
```

(b) txt file used for decay test in yaw direction for floater 1

Figure D.2: External force files used for the decay simulations

### D.4. User defined wave elevation time trace

#### *User defined time trace*

The User defined time trace was used for all regular and irregular wave tests that were performed to compare with the basin tests. For simulation of regular and irregular waves, time traces from the basin tests are used for a wave probe that is in line with the GCS origin, depending on the wave direction. The wave elevations are retrieved from the h5file for a specific test. A txt file is generated containing:

- sample time step  $dt = 0.02236$ , which corresponds to a sample frequency of 200Hz on model scale.
- Wave height measured at specific wave probe for each sample time step

The incoming waves of the basin test and the simulations have been compared to ensure that the same external environment is used in both situations. Firstly, figure D.3 shows a plot of the wave elevation at the origin of the GCS. As can be seen, these signals are fully in agreement. Furthermore, to check the actual wave angle that is applied in the basin tests (due to test environment, this might be different than set up), two wave probe signals are used for the beam and head waves. Table D.1 shows the average angle that the waves have

relative to their desired wave angle. This angle is calculated by the phase differences between elevation measurements of the wave probes. As can be seen, the differences between the desired and actual incoming wave angle are negligible.

Combining these two aspects, it can be concluded that the incoming waves are in agreement for the simulation model and the basin tests.

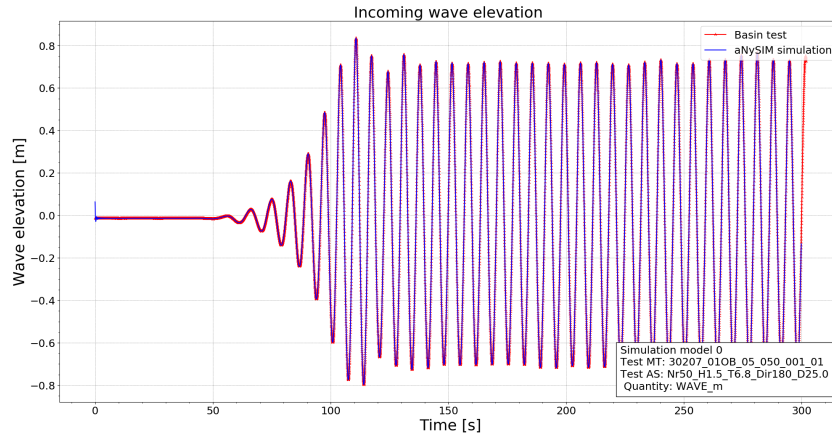


Figure D.3: Wave elevation timetraces at origin of GCS for the basin tests and the aNySIM model

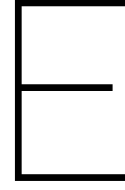
Basin test nr	Desired wave angle[°]	Actual wave angle[°]
50	180	179.94
51	180	179.99
52	180	180.07
53	90	89.20
54	90	90.77
55	90	90.79

Table D.1: Desired and actual wave angle that is obtained in the basin tests for regular head and beam waves

## D.5. aNySIM defined wave elevation

aNySIM can compute wave elevation time traces from given input parameters. Regular waves are computed by definition of a wave height  $H$  and period  $T$ . Irregular waves are computed following a JONSWAP spectrum where the following parameters must be defined:

- $T_p$  = Peak period of spectrum
- $H_s$  = Significant wave height
- $\gamma$  = Spectrum peakedness factor, set on 0.3 for the JONSWAP spectrum



## Studies in aNySIM

Different studies that were performed in aNySIM are briefly explained in this appendix.

### E.1. Numerical integration

To explain the numerical integration method, the problem is simplified to one body and 1 DOF. Equation (3.37) is split in a set of two first order ODE's:

$$\frac{d}{dt} \begin{Bmatrix} x(t) \\ \dot{x}(t) \end{Bmatrix} = \begin{Bmatrix} \dot{x}(t) \\ \frac{\int_{-\infty}^t R(t-\tau)\dot{x}(\tau)d\tau}{m+a} + \frac{c \cdot x(t)}{m+a} \end{Bmatrix} + \begin{Bmatrix} 0 \\ F \end{Bmatrix} \quad (\text{E.1})$$

To solve for this set of equations, the following initial value problem is defined:

$$\frac{d}{dt} \mathbf{y}(t) = \mathbf{f}(t, \mathbf{y}(t)) \quad \text{with } \mathbf{y}(t_0) = \mathbf{y}_0 \quad (\text{E.2})$$

With:

$$\mathbf{y}(t) = \begin{Bmatrix} x(t) \\ \dot{x}(t) \end{Bmatrix}, \mathbf{f}(t, \mathbf{y}(t)) = \begin{Bmatrix} \dot{x}(t) \\ \frac{\int_{-\infty}^t R(t-\tau)\dot{x}(\tau)d\tau}{m+a} + \frac{c \cdot x(t)}{m+a} \end{Bmatrix} + \begin{Bmatrix} 0 \\ F \end{Bmatrix} \quad (\text{E.3})$$

Solving for the next time step  $\mathbf{y}(t_{n+1})$ , this gives:

$$\mathbf{y}(t_{n+1}) = \mathbf{y}(t_n) + \int_{t_n}^{t_{n+1}} \mathbf{f}(t, \mathbf{y}(t)) dt \quad (\text{E.4})$$

As it is generally not possible to solve (E.4) analytically, this is solved numerically. The explicit 'RK4' scheme is used, with for  $t_{n+1} = t_n + \Delta t$ :

$$k_1 = \mathbf{f}(t_n, \mathbf{y}(t_n)) \quad (\text{E.5})$$

$$k_2 = \mathbf{f}(t_{\frac{1}{2}}, \mathbf{y}(t_n) + \frac{\Delta t}{2} k_1) \quad (\text{E.6})$$

$$k_3 = \mathbf{f}(t_{\frac{1}{2}}, \mathbf{y}(t_n) + \frac{\Delta t}{2} k_2) \quad (\text{E.7})$$

$$k_4 = \mathbf{f}(t_1, \mathbf{y}(t_n) + \Delta t k_3) \quad (\text{E.8})$$

$$\mathbf{y}(t_{n+1}) = \mathbf{y}(t_n) + \frac{\Delta t}{6} (k_1 + 2k_2 + 2k_3 + k_4) \quad (\text{E.9})$$

To determine the function  $\mathbf{f}$  for each time step in aNySIM, the integrator part has childs that contain information on the hydrodynamic and hydrostatic forces, the wave exciting and current forces and the mechanic interaction forces.

A study on the time step in aNySIM has been conducted to select a fitting time step for the simulations. A time step of 0.01 seconds has been selected, as results are equal to smaller time steps but computational time significantly decreases. Figure /// shows results of floater 1 for 4 different time steps, showing no difference. Therefore, the largest time step (0.01) is adopted.

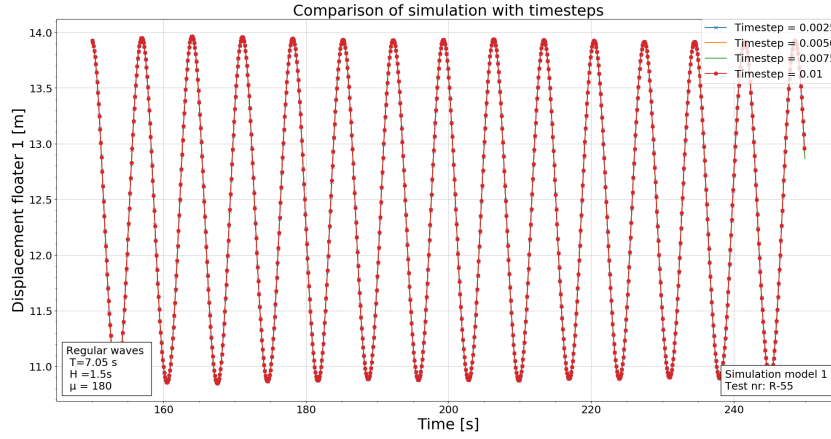


Figure E.1: Motion of floater1 for 4 different time steps, no differences in results can be observed.

Table E.1: Implemented values for joint damping

Direction	critical damp	damp 1	damp 2	damp 3	damp 4	damp 5	damp 6	Final % of critical damping
$b_1$ [Ns/m]	14832.4	9410	941	4705	4450	4449.719	941	6%
$b_2$ [Ns/m]	15165.75	9700	970	4850	4550	4549.725	970	6%
$b_3$ [Ns/m]	15165.75	29100	2910	14550	4550	2274.863	14550	96%
$b_4$ [Nms/rad]	1816.59	7.79	0.779	3.895	55	55	55	3%
$b_5$ [Nms/rad]	1702.939	6.697	0.6697	3.3485	51	51	51	3%
$b_6$ [Nms/rad]	1702.939	6.937	0.6937	3.4685	51	51	51	3%

## E.2. Mechanical joint damping

The implementation of joints has not been thoroughly researched in this thesis. However, a sensitivity study on the damping applied to the joints has been performed. Damping is necessary to obtain numerical stability but must not influence the physical results since the mechanical damping of the springs implemented in the offshore basin model is negligible. Six different damping values have been analysed to see the influence on the forces in the joints and address stability. These different damping values can be observed in table E.1. The final damping (damping 6) has been used in further simulations. This damping value is shown as a percentage of the critical damping:

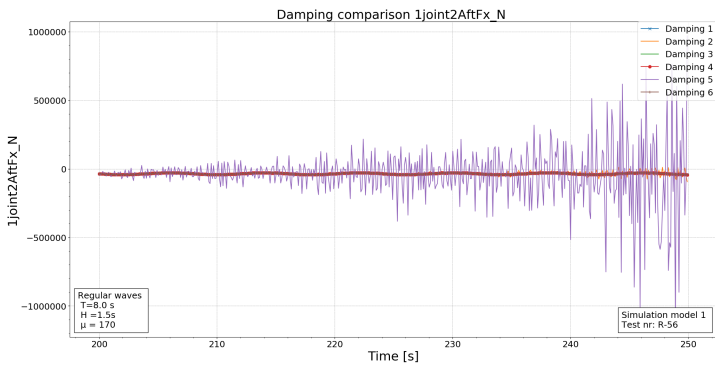
$$b_{crit} = 2\sqrt{mS_e} \quad (E.10)$$

where  $m$  is the mass of the joints (estimated at 25 kg, this is found in computations of Oceans of Energy), and  $S_e$  is the stiffness matrix of the joint, which is different in all 6 DOF.

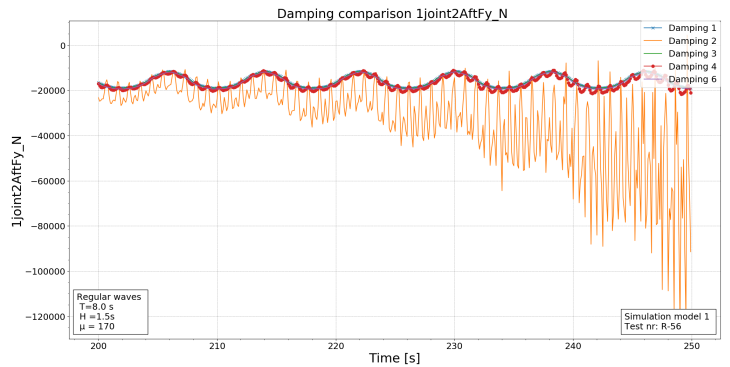
Figures E.2a to E.2c clearly show that damping implementations 5, 2 and 4 result in unstable behaviour in the simulation. This is a result of the (relatively) low damping applied in heave direction. Figure E.2d shows the results for damping 1, 3 and 6 only. Here, all 3 implementations give a stable result with comparable amplitudes and behaviour. Since damping 6 contains the lowest damping values, this is selected.

## E.3. Drag coefficient

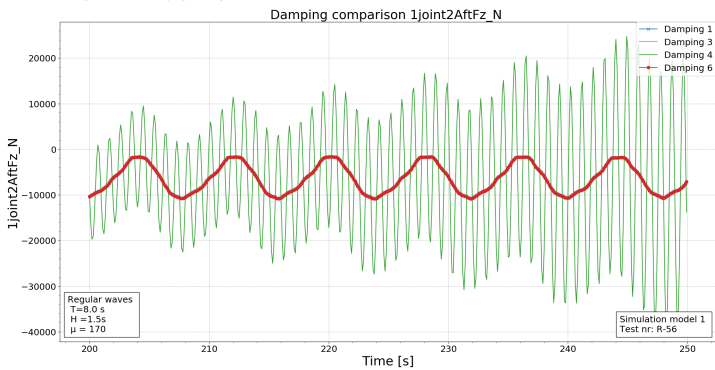
The drag coefficient influences the drag force on the floaters and therefore the motion amplitude. However, since the drag force scales quadratically with the velocity of the floaters, the drag force is not a pure sine (for regular waves). For the fitting method of the 'regular wave-fit' model it is desired to fix the drag coefficient and purely adjust the linear damping. However, if the drag force significantly influences the motion behaviour of the floaters, this coefficient must be fitted as well to obtain the optimal results. Figure E.3 shows results with 2 different drag coefficients (used for the 'decay-fit' and 'regular wave-fit' model). As can be observed, only the amplitude is influenced, and the motion shows a sine line behaviour that is predominantly influenced by the wave exciting forces. From this comparison, it can be concluded that the drag coefficient can be set to a fixed value, obtained from literature and the fitting process can be done with linear coefficients only.



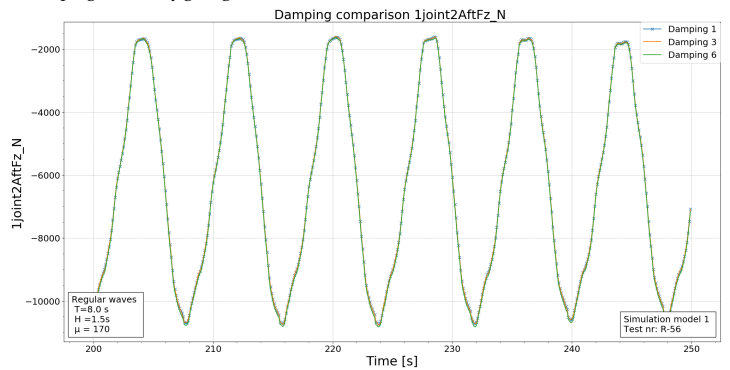
(a) Force in x direction for the aft joint between floater 1 and 2. The simulation with damping 5 is clearly giving an unstable result



(b) Force in y direction for the aft joint between floater 1 and 2. The simulation with damping 2 is clearly giving an unstable result



(c) Force in z direction for the aft joint between floater 1 and 2. The simulation with damping 4 is clearly giving an unstable result



(d) Results of damping 1, 3 and 6 are all stable for the force in z direction of the aft joint between floater 1 and 2.

Figure E.2: Results for irregular wave tests

### E.4. Lumped mass line time step and number of elements

The lumped mass line object in aNySIM separately solves the equation of motion for the mooring line, where hydrodynamic forces as damping and added mass are taken into account. To assure that the solution is stable and converged, a study on the required step size and number of elements is done.

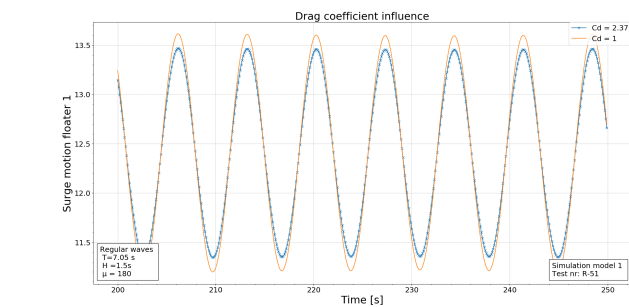


Figure E.3: Grouping of floaters in rows to combine the forces per row

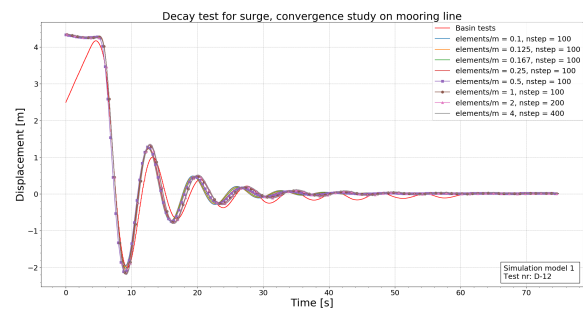
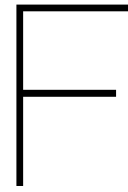


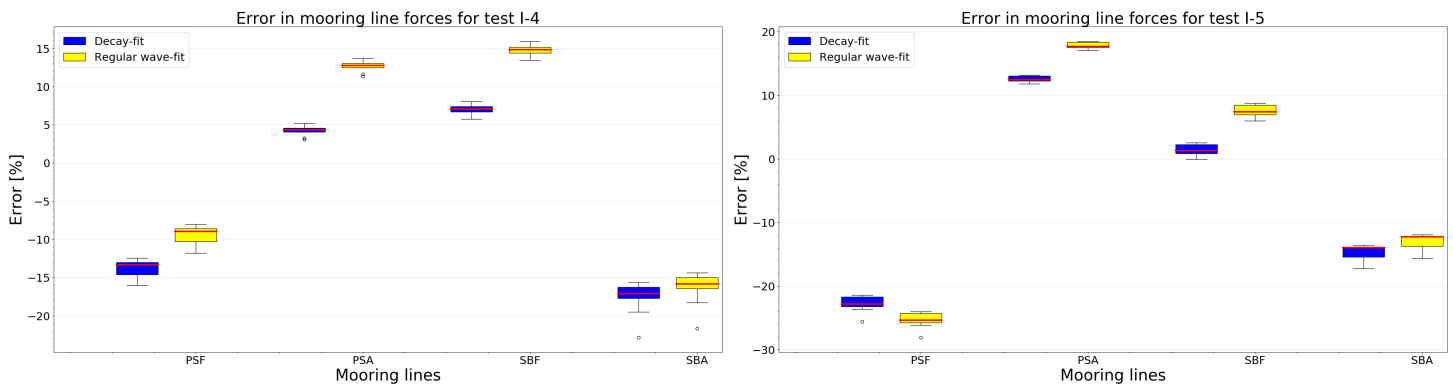
Figure E.4: Convergence study on the elements and step size for the Lumped mass mooring line



# aNySIM results

## F.1. Mooring line errors all irregular wave tests

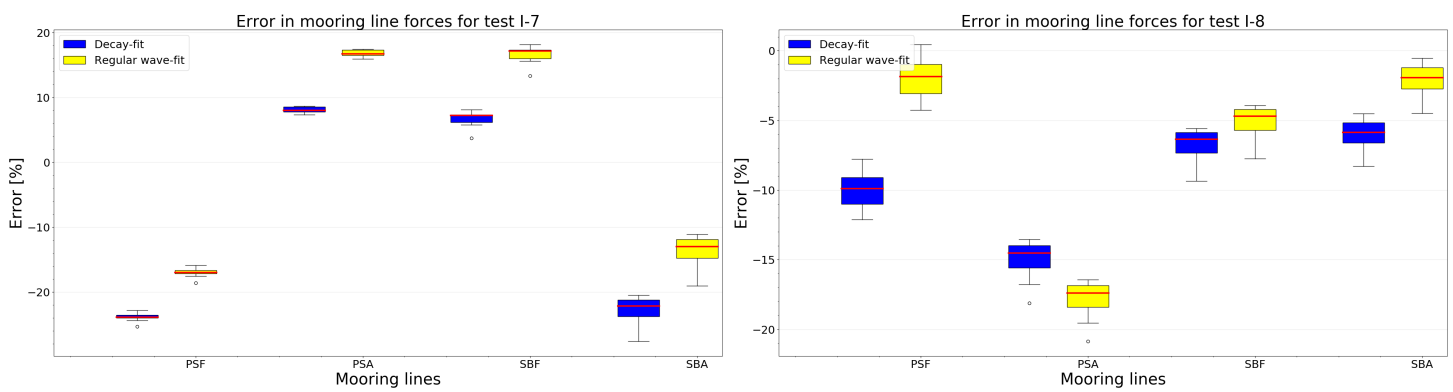
The error in the mooring line forces as calculated in aNySIM are shown for all irregular wave tests.



(a) Error in mooring line forces for I-4 ( $T_s 6.7H_s 2.0\mu 180^\circ$ )

(b) Error in mooring line forces for I-4 ( $T_s 6.7H_s 2.0\mu 90^\circ$ )

Figure F1: Error in mooring line forces for the 10 highest forces obtained from the basin tests. Errors are shown for the 'decay-fit' method and the 'regular wave-fit' method for all 4 mooring lines.



(a) Error in mooring line forces for I-7 ( $T_s 6.7H_s 2.0\mu 180^\circ$ )

(b) Error in mooring line forces for I-8 ( $T_s 6.7H_s 2.0\mu 90^\circ$ )

Figure F2: Error in mooring line forces for the 10 highest forces obtained from the basin tests. Errors are shown for the 'decay-fit' method and the 'regular wave-fit' method for all 4 mooring lines.

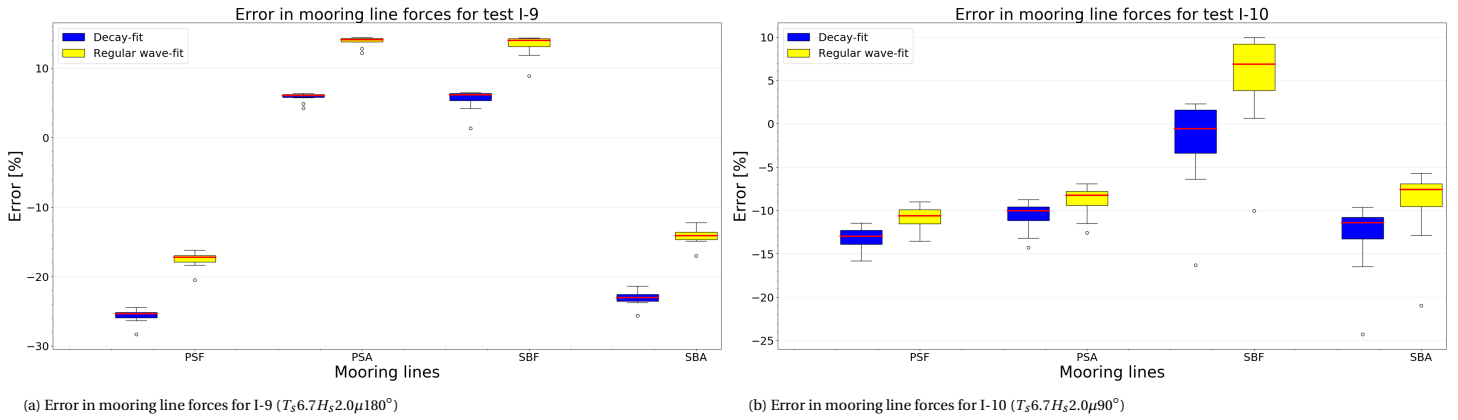


Figure E3: Error in mooring line forces for the 10 highest forces obtained from the basin tests. Errors are shown for the 'decay-fit' method and the 'regular wave-fit' method for all 4 mooring lines.

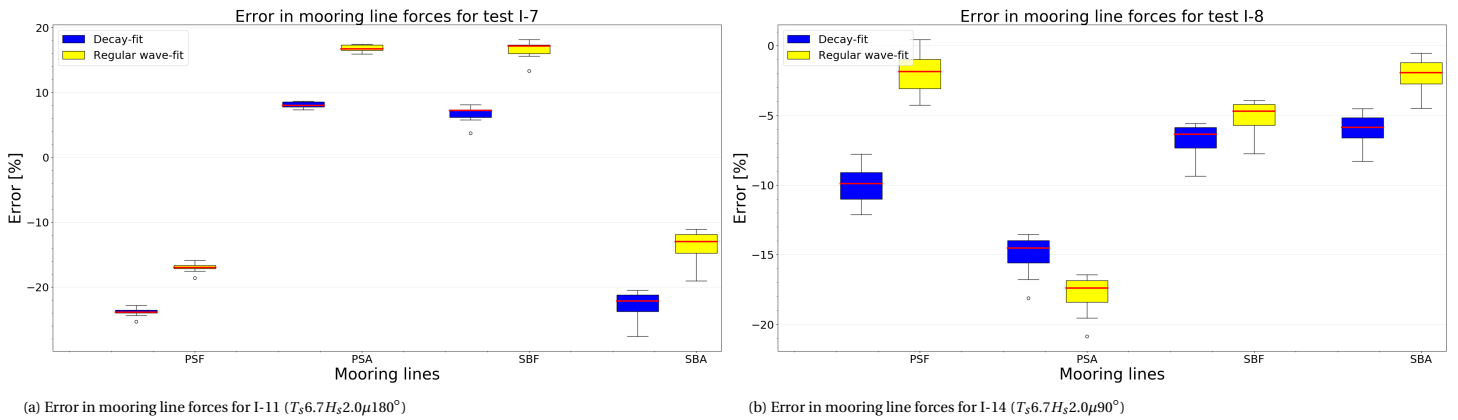
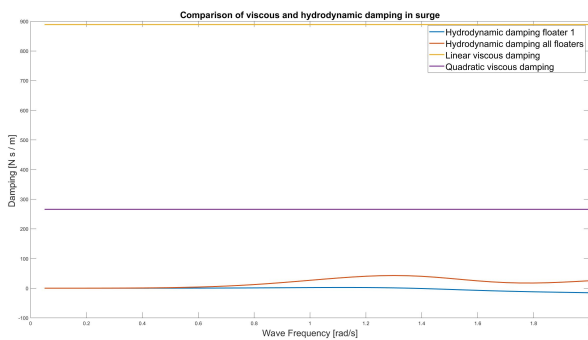


Figure E4: Error in mooring line forces for the 10 highest forces obtained from the basin tests. Errors are shown for the 'decay-fit' method and the 'regular wave-fit' method for all 4 mooring lines.

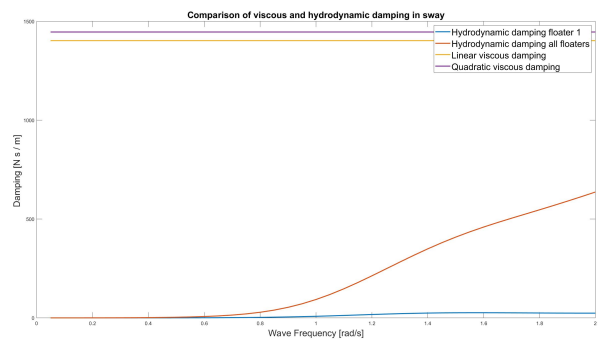
# G

## Supporting figures and tables

### G.1. Comparison hydrodynamic/viscous damping

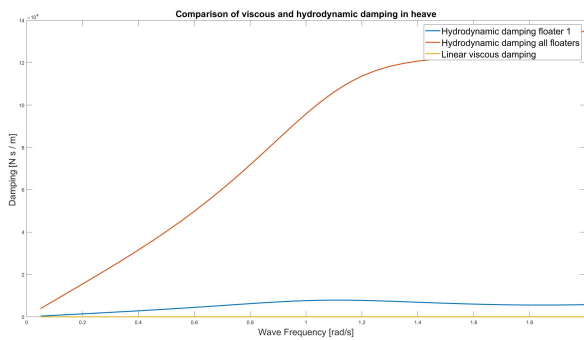


(a) Viscous and Hydrodynamic damping in surge direction for a range of  $\omega = 0$  to 2 rad/s. The viscous contribution is much larger than the hydrodynamic damping contribution.

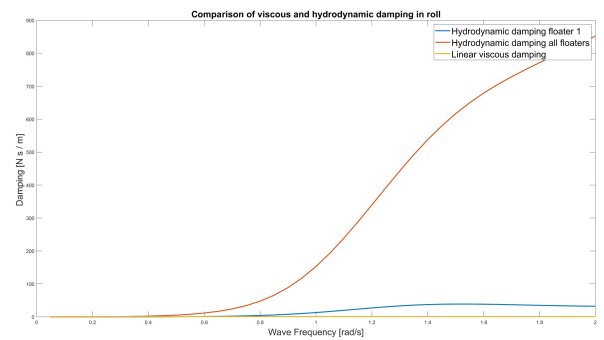


(b) Viscous and Hydrodynamic damping in sway direction for a range of  $\omega = 0$  to 2 rad/s. The viscous contribution is much larger than the hydrodynamic damping contribution.

Figure G.1: Comparison of contribution hydrodynamic and viscous damping

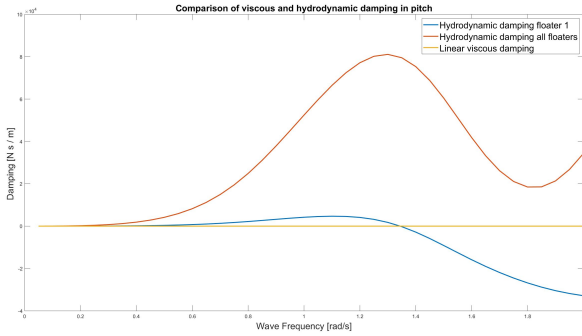


(a) Viscous and Hydrodynamic damping in heave direction for a range of  $\omega = 0$  to 2 rad/s. The hydrodynamic damping contribution of the surrounding floaters is the most important damping term.

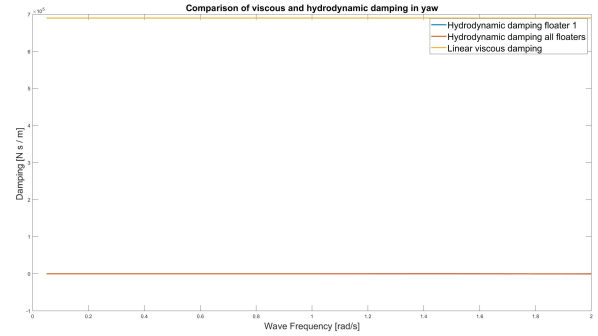


(b) Viscous and Hydrodynamic damping in roll direction for a range of  $\omega = 0$  to 2 rad/s. The hydrodynamic damping contribution of the surrounding floaters is the most important damping term.

Figure G.2: Comparison of contribution hydrodynamic and viscous damping



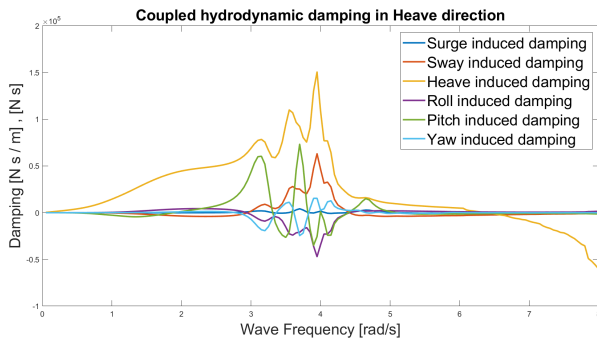
(a) Viscous and Hydrodynamic damping in pitch direction for a range of  $\omega = 0$  to 2 rad/s. The hydrodynamic damping contribution of the surrounding floaters is the most important damping term.



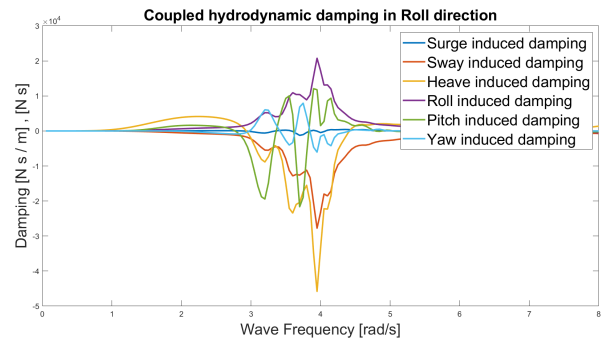
(b) Viscous and Hydrodynamic damping in yaw direction for a range of  $\omega = 0$  to 2 rad/s. The viscous contribution is much larger than the hydrodynamic damping contribution.

Figure G.3: Comparison of contribution hydrodynamic and viscous damping

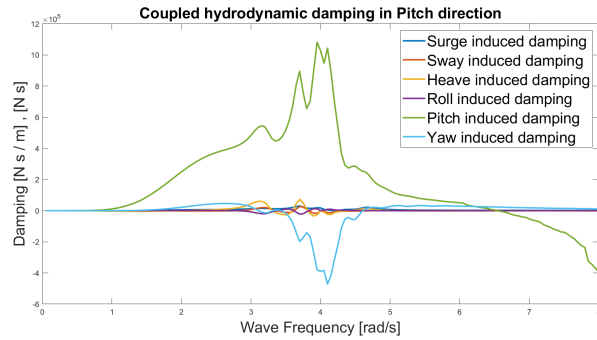
## G.2. Hydrodynamic coupling between degrees of freedom



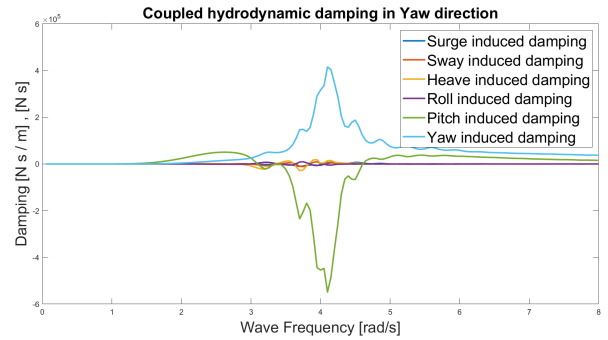
(a) Hydrodynamic damping in heave direction due to motions in other DOF



(b) Hydrodynamic damping in roll direction due to motions in other DOF



(c) Hydrodynamic damping in pitch direction due to motions in other DOF



(d) Hydrodynamic damping in yaw direction due to motions in other DOF

Figure G.4: The coupled hydrodynamic damping in heave, roll, pitch and yaw direction obtained from the hyd file.

## G.3. Force contributions

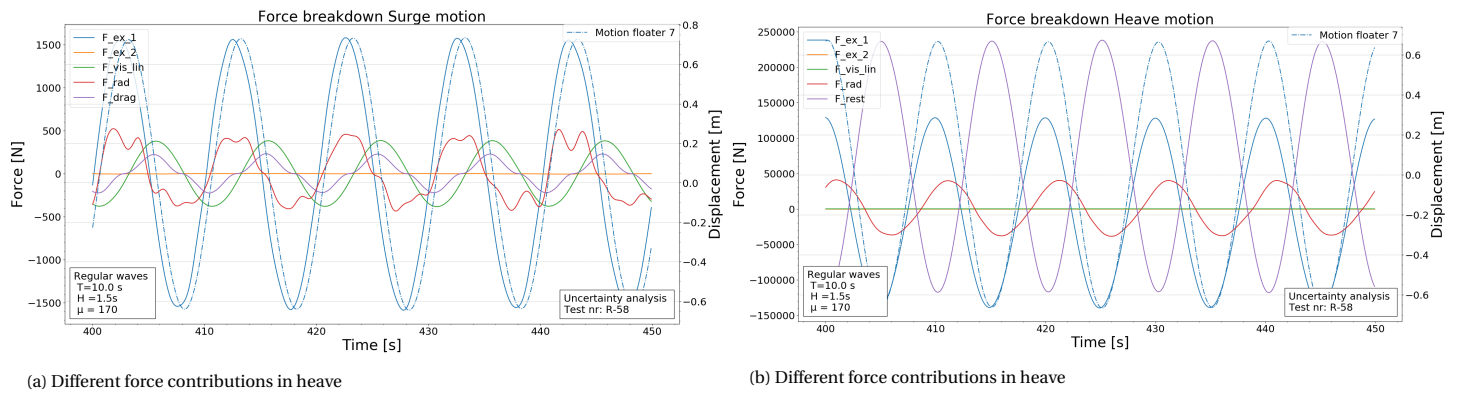


Figure G.5: Force split for surge and heave in regular wave test R-58

## G.4. Maximum mooring line forces Basin test results

### G.5. Shielding implementation

The shielding percentages implemented for the drag coefficient differ for all floaters and the incoming wave angle. Table G.1 shows the shielding effect as implemented in aNySIM for the different floaters.

Table G.1: The shielding percentages for all different floaters depending on the incoming wave angle.

Wave angle	Floater									
	1	2,3	4	5	6,7	8	9	10,11	12	
0	0.25	0.25	0.25	0.25	0.25	0.25	1	1	1	
10	0.25	0.25	1	0.25	0.25	1	1	1	1	
20	0.25	0.25	1	0.25	0.25	1	1	1	1	
30	0.25	0.25	1	0.25	0.25	1	1	1	1	
40	0.25	0.25	1	0.25	0.25	1	1	1	1	
50	0.25	0.25	1	0.25	0.25	1	1	1	1	
60	0.25	0.25	1	0.25	0.25	1	1	1	1	
70	0.25	0.25	1	0.25	0.25	1	1	1	1	
80	0.25	0.25	1	0.25	0.25	1	1	1	1	
90	0.25	0.25	1	0.25	0.25	1	0.25	0.25	1	
100	1	1	1	0.25	0.25	1	0.25	0.25	1	
110	1	1	1	0.25	0.25	1	0.25	0.25	1	
120	1	1	1	0.25	0.25	1	0.25	0.25	1	
130	1	1	1	0.25	0.25	1	0.25	0.25	1	
140	1	1	1	0.25	0.25	1	0.25	0.25	1	
150	1	1	1	0.25	0.25	1	0.25	0.25	1	
160	1	1	1	0.25	0.25	1	0.25	0.25	1	
170	1	1	1	0.25	0.25	1	0.25	0.25	1	
180	1	1	1	0.25	0.25	0.25	0.25	0.25	0.25	
190	1	1	1	1	0.25	0.25	1	0.25	0.25	
200	1	1	1	1	0.25	0.25	1	0.25	0.25	
210	1	1	1	1	0.25	0.25	1	0.25	0.25	
220	1	1	1	1	0.25	0.25	1	0.25	0.25	
230	1	1	1	1	0.25	0.25	1	0.25	0.25	
240	1	1	1	1	0.25	0.25	1	0.25	0.25	
250	1	1	1	1	0.25	0.25	1	0.25	0.25	
260	1	1	1	1	0.25	0.25	1	0.25	0.25	
270	1	0.25	0.25	1	0.25	0.25	1	0.25	0.25	
280	1	0.25	0.25	1	0.25	0.25	1	1	1	
290	1	0.25	0.25	1	0.25	0.25	1	1	1	
300	1	0.25	0.25	1	0.25	0.25	1	1	1	
310	1	0.25	0.25	1	0.25	0.25	1	1	1	
320	1	0.25	0.25	1	0.25	0.25	1	1	1	
330	1	0.25	0.25	1	0.25	0.25	1	1	1	
340	1	0.25	0.25	1	0.25	0.25	1	1	1	
350	1	0.25	0.25	1	0.25	0.25	1	1	1	

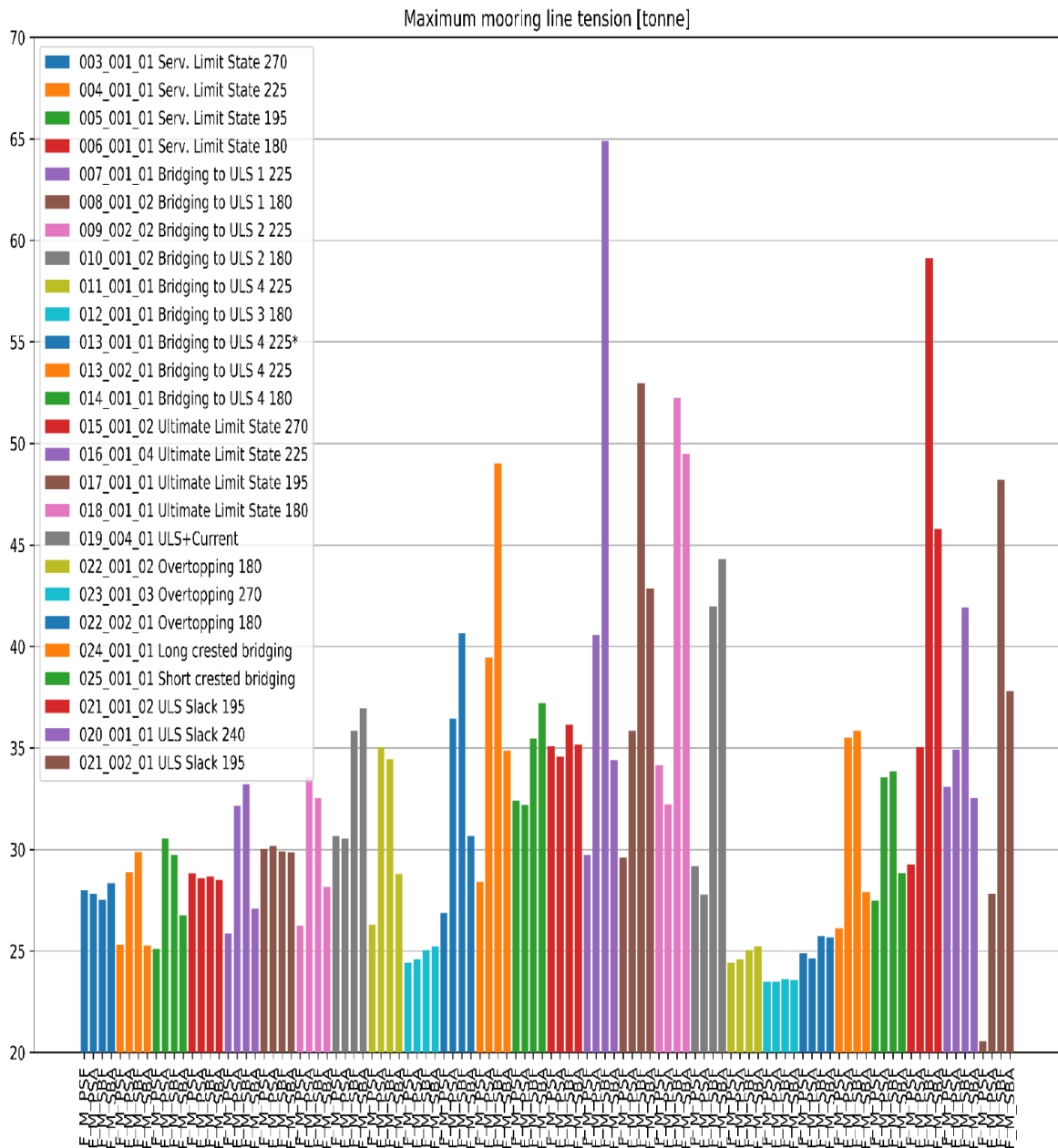


Figure G.6: The maximum measured force in the mooring lines for all irregular wave tests, obtained from the MARIN report [31]